Redox Kinetics of Nonstoichiometric Oxides

Thesis by
Ho-Il Ji

In Partial Fulfillment of the Requirements for the
degree of
Doctor of Philosophy

CALIFORNIA INSTITUTE OF TECHNOLOGY
Pasadena, California

2017
Defended May 12, 2017

Ho-Il Ji
ORCID: 0000-0002-6194-991X

ACKNOWLEDGEMENTS

First and foremost, I would like to thank my advisor, Prof. Sossina Haile, who taught me a sincere attitude towards science.
I owe much of the completion of this thesis to my brilliant lab mates, Tim, Mike, and Philipp.
I am also thankful to Chris, Anu, Haemin, and Sihyuk for enduring the extreme weather change with me.

Good memories with friends and church members at Pasadena and Evanston will be long lasting in my mind. I believe that many valuable experiences, even though some of those were unbearable, definitely nurtured me.

I would like to express my deepest gratitude to my family for their endless love.

Lastly, God always gives me more than I deserve.
I promise that I will walk in your footsteps to the end.

The LORD is my shepherd,
I shall not be in want.
(Psalms 23:1)

ABSTRACT

Cerium oxide ($CeO_{2-\delta}$) and its derivatives are the most attractive materials under consideration for solar-driven thermochemical production of chemical fuels. Understanding the rate-limiting factors in fuel production is essential for maximizing the efficacy of the thermochemical process.

The rate of response of the porous ceria structured with architectural features typical of those employed in solar reactors was measured via electrical conductance relaxation methods. A transition from behavior controlled by material surface reaction kinetics to that controlled by sweep-gas supply rates is observed on increasing temperature, increasing volume specific surface area, and decreasing normalized gas flow rate. The transition behavior is relevant not only for optimal reactor operation and architectural design of material, but also for accurate measurement of material properties.

The redox kinetics of undoped ceria, $CeO_{2-\delta}$ at extreme high temperature (1400 °C) was investigated using the electrical conductivity relaxation method, and those of 10% Pr doped ceria at low temperature (700 °C) were done using the mass relaxation method. It was demonstrated under sufficiently high gas flow rates relative to the mass of the oxide, which is required in order to overcome gas phase limitations and access the material kinetic properties. Furthermore, the surface reaction rate constant of undoped ceria, k_{Chem}, was investigated at high temperature (1400 °C) in humidified gas atmosphere, in consideration of the operating conditions in thermochemical fuel production system. It was demonstrated that H_2O potentially plays a role of oxidants as increasing temperature and/or decreasing oxygen partial pressure; thus in such thermodynamic conditions, pH_2O, besides temperature and pO_2, needs to be carefully considered in surface reaction study.

In addition to relaxation experiments under small driving force for redox reaction, the kinetics of surface related oxidation reaction under large chemical driving force (large ΔpO_2) was investigated by mass relaxation method. Based on the generalized reaction rates of several possible rate determining steps, the relaxation behavior in oxygen concentration for all possible rate determining steps were computed. On the comparison with the experimental results, the most probable rate determining step was suggested (reduction of diatomic oxygen from neutral oxygen molecule to superoxide), and the oxidation kinetics under large driving force was explained.

PUBLISHED CONTENT AND CONTRIBUTIONS

Chapter 2

H.I. Ji, T.C. Davenport, M.J. Ignatowich, S.M. Haile, Gas-phase vs Material-kinetic Limits on the Redox Response of Nonstoichiometric Oxides, *Physical Chemistry Chemical Physics*, **2017** 19(10) 7420-7430. doi: 10.1039/C7CP00449D

H.I. Ji participated in the development of the concept, performed the experiments and analyses, and wrote the paper.

Chapter 3

H.I. Ji, T.C. Davenport, C.B. Gopal, S.M. Haile, Extreme high temperature redox kinetics in ceria: exploration of the transition from gas-phase to material-kinetic limitations, *Physical Chemistry Chemical Physics*, **2016** 18(31) 21554-21561. doi: 10.1039/C6CP01935H

H.I. Ji participated in the development of the concept, performed the experiments and analyses, and wrote the paper.

Chapter 4

P. Simons, **H.I. Ji**, T.C. Davenport, S.M. Haile, A Piezomicrobalance System for High-temperature Mass Relaxation Characterization of Metal Oxides: A Case Study of Pr-doped Ceria, *Journal of the American Ceramic Society*, **2017** 100(3) 1161-1171. doi: 10.1111/jace.14652

H.I. Ji participated in the development of test station, performed the following experiments and analyses: mass relaxation experiments for piezo-crystal without Ti layer, micro-structure and surface-structure characterization.

TABLE OF CONTENTS

LIST OF ILLUSTRATIONS

Number *Page*

LIST OF TABLES

Chapter 1

INTRODUCTION

1.1 Overview

Fossil fuels, such as coal and natural gases, and petroleum for nuclear power generation are still the dominant sources of energy in the modern world, and the energy demand is continuously increasing at a rate of about 2% per year. [1]. However, as is already well known, two main problems are crucial for the future energy crisis: the reserves of fossil fuels are being depleted faster, and their use has been drastically generating a large amount of greenhouse gases, resulting in global warming. [2] This has led to the need for renewable energy solutions, as shown in Figure 1.1, and such as renewable energy is the fastest growing source of energy consumption. Fuel cells, which are devices that convert chemical energy forms such as hydrogen and/or hydrocarbon fuels to electricity with harmless byproduct, namely water, have long been considered a promising technology. In conjunction with this, the generation of the fore-mentioned chemical energy sources by using solar energy is considered another main part for completing a sustainable energy cycle.

Of various fuel cell types, solid-oxide fuel cells (SOFCs) have the benefit of high power generation with fuel flexibility at the intermediate temperature (400 ~ 700

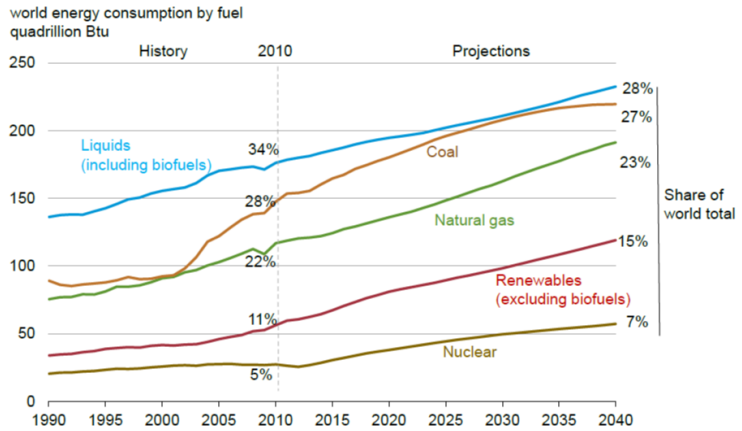

Figure 1.1: Previous and projected future world energy consumption for various energy sources [1]

°C), and many efforts have been devoted to the enhancement of the activity of electrochemical reactions at the electrodes and/or electrode/electrolyte interfaces, which are considered the main obstacle of high performance as the operating temperature decreases. Regarding fuel generation, especially hydrogen, various approaches to solar-driven water splitting have been widely studied, such as photoelectrochemical cells [3, 4] and solar-driven thermochemical fuel production [5, 6]. The latter has been receiving significant attention due to its simple pathway to convert solar energy to fuel by utilizing the large oxygen nonstoichiometry change of the oxide materials, and its potential for large scale fuel production. For higher solar-to-fuel energy conversion efficiency, it is required that the amount of fuel production per unit time (which is considered to be a convoluted result of large $\Delta\delta$ and favorable thermodynamic driving force of oxides for dissociating H_2O/CO_2, as well as faster oxidation/reduction kinetics of the oxides) is enhanced.[7, 8]

In this aspect of the better performance, material kinetic properties of the oxides employed as the electrodes or electrolyte in SOFCs have been vastly investigated for the fundamental understanding as well as the actual application such as material selection and device design.[9–13] In contrast, the study on the redox kinetics of materials in thermochemical fuel production is very sparse and the fundamental understanding of kinetics is not well established, whereas the thermodynamic property of materials, *i.e.* equilibrium oxygen nonstoichiometry vs. thermodynamic conditions (here, oxygen partial pressure & temperature) is broadly and steadily investigated.[14–17] This is probably due to the complicated operating conditions compared to the relatively simple general approaches for addressing kinetic properties. The conditions are large ΔT and/or large ΔpO_2 swings, and high pH_2O or pCO_2 conditions along the oxidation reaction. In this work, we aim to fundamentally understand the redox kinetic behavior under the thermochemical cycle conditions.

1.2 Transport kinetics in oxide materials

Three experimental techniques, the electrical, tracer, and chemical experiments (as depicted in Figure 1.2), for assessing oxygen ion transport kinetics in the oxide materials are widely used.[18] For the first technique in Figure 1.2(a), the redox reaction is driven by an outer electrical potential gradient, thereby in the case of

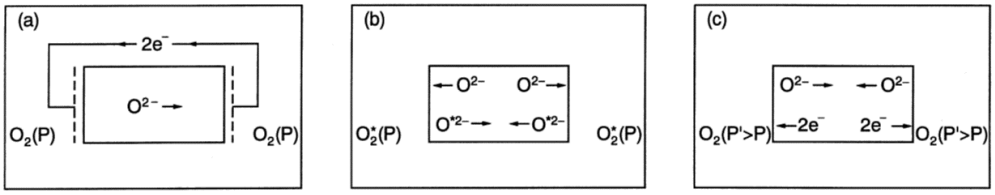

Figure 1.2: Three fundamental experimental techniques applied to elucidate transport properties of mixed ionic-electronic conducting oxides. Reprinted from a reference [18]

oxygen ionic conducting oxides induce the internal ionic current to compensate the outer electronic current. Here, ionic conductivity of the oxide can be converted to the diffusion coefficient according to Nernst-Einstein equation when the electrodes are ideally reversible and surface reaction is much fast enough. If the surface reaction limits the overall reaction, the surface reaction rate constant can be derived from the ionic resistance normalized by area instead of the ionic conductivity used in the diffusion limited case. This operation is quite similar to that of solid oxide fuel cells. The case of Figure 1.2(b) is the tracer experiments. The driving force is the concentration gradient of the tracer without any electrical or oxygen chemical potential gradient, and the transport occurs just by random exchange, for example, between oxygen in the oxide and the isotope in the oxide. The transport parameters are extracted by analyzing the profile of tracer concentration from the surface to the interior of the oxide. In the last case of chemical experiments depicted in Figure 1.2(c), the redox reactions are driven by chemical potential gradient, generally an abrupt change in oxygen partial pressure (pO_2) in atmosphere, and therefore the oxygen nonstoichiometry of the oxide changes to the new equilibrium with the changed pO_2. Here, in the case of mixed-ionic and electronic binary conductor for example, the ionic and electronic fluxes couterbalance each other, and thus both diffusivities of ions and electrons are involved in one governing effective diffusivity, namely the chemical diffusion coefficient (D_{Chem}). These three techniques give different types of surface reaction rate constants and diffusion coefficients. The correlation between each parameter, such as between surface reaction rate constants or diffusion coefficients measured from different techniques, are quite complicated. The correlation is influenced by point defect structure of materials such as a thermodynamic factor of oxygen, w_{O} ($\frac{d\ln a_{\mathrm{O}}}{d\ln c_{\mathrm{O}}}$, where a_{O} is activity and c_{O} is concentration of oxygen), and a conducting type of the oxide (ionic, electronic, or mixed ionic-electronic conductor).[19] Thus, the material evaluation for the kinetic properties considering

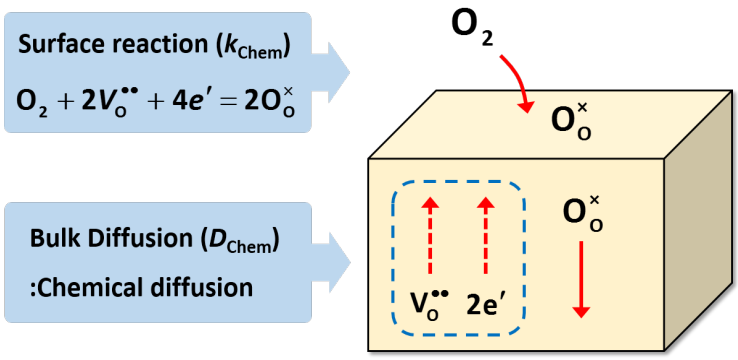

Figure 1.3: Schematics of surface reaction and chemical diffusion processes for oxidation of oxides

the operating condition in actual apllication is the easier, more accurate, and more precise approach.

Especially in the case of chemical experiments, the overall redox kinetics of the oxygen nonstoichiometry re-equilibration consists of two consecutive steps: the chemical surface reaction occuring at the gas/oxide interface, and the chemical bulk diffusion inside the oxide, as depicted in Figure 1.3. In most of cases, the chemical diffusion coefficient (D_{Chem}) and surface reaction rate constant (k_{Chem}) are strongly dependent on the sample geometry as well as $p\mathrm{O}_2$ in the oxide systems; thus most of the research has addressed those kinetic properties for well-defined geometry sample at specifically fixed $p\mathrm{O}_2$ values. In other words, they assume the kinetic parameters to be constant values by applying sufficiently small $p\mathrm{O}_2$ changes on the oxide, and analyze the kinetic relaxation behavior from directly/indirectly detecting mass, electrical conductivity, volume change, and so on.[20–27] This assumption makes the analysis much easier from the analytical solutions for every case, such as in surface reaction limited, bulk diffusion limited, and co-limited of both reactions.[22]

Since a time constant for the diffusion reaction is proportional to the square of a diffusion length (usually half of thickness of sample) and that of surface reaction is simply proportional to the diffusion length, dominant reaction limiting the overall reaction can be controlled by the diffusion length: longer diffusion length tends to be in the diffusion limited and the shorter tends to be in the surface reaction limited.

1.3 Principle of thermochemical fuel production

The process in thermochemical fuel production is described in the reactions given below for the nonstoichiometric oxide, MO_y, involving the thermal reduction in Eq. (1.1) and the oxidation by steam and/or carbon dioxide in Eq. (1.2): [8]

$$\frac{1}{\delta_{red}-\delta_{ox}}MO_{y-\delta_{ox}} \rightarrow \frac{1}{\delta_{red}-\delta_{ox}}MO_{y-\delta_{red}} + \frac{1}{2}O_2 \tag{1.1}$$

$$\frac{1}{\delta_{red}-\delta_{ox}}MO_{y-\delta_{red}} + H_2O\,(\text{or } CO_2) \rightarrow \frac{1}{\delta_{red}-\delta_{ox}}MO_{y-\delta_{ox}} + H_2\,(\text{or CO}) \tag{1.2}$$

where δ_{ox} and δ_{red} respectively indicate the oxygen nonstoichiometry values at equilibrium under thermal reduction and thermochemical oxidation of the metal oxide. For the reduction, the material is exposed to the oxygen-poor gas such as Ar or N_2 inert gases at high temperature ($\sim$ 1500 °C) to induce the oxygen release from the oxide. For the oxidation, two approaches have been suggested: (i) maximizing the utility of oxygen nonstoichiometry change by decreasing the temperature to $\sim$ 800 °C (temperature swing mode depicted in Figure 1.4(a)), [6, 28] or (ii) eliminating the thermomechanical challenges associated with the rapid thermal swings by keeping the temperature constant ($\sim$ 1500 °C) (pressure swing mode as depicted in Figure 1.4(b)). [29, 30] Here, the driving force of the oxidation reaction is the change in oxygen chemical potential driven by the new state of thermodynamic conditions (T and/or pO_2), and thus the oxide is oxidized to the new equilibrium state. For example of the best candidate material system, $CeO_{2-\delta}$, δ_{red} at 1500 °C under 10ppm O_2 in Ar atmosphere ($pO_2 = 10^{-5}$ atm) is 0.067, *i.e.* 2-δ of 1.93 is obtained. For the oxidation reaction, considering the 20% steam supply as an oxidant in Ar balance, the equilibrium pO_2 values are 1.62×10^{-7} atm (log (pO_2/atm) = -6.8) at 800 °C in temperature swing mode, and 2.55×10^{-4} atm (log (pO_2/atm) = -3.6) at 1500 °C in pressure swing mode. These equilibrium pO_2s are calculated from the thermodynamic data of water dissociation by thermolysis.[31] Thus, $\Delta\delta$s, which are utilized for dissociating H_2O/CO_2 per cycle, are 0.067 and 0.033 for temperature and pressure swing modes, respectively, as shown in Figure 1.4.

The better thermodynamic property of the oxide (here, large $\Delta\delta$, which is δ_{ox}-δ_{red}) doesn't guarantee the high efficiency of the whole system. For the temperature swing mode, high levels of solid state heat recovery should be achieved for high efficiency. Furthermore, reduction and oxidation kinetics are essential: faster kinetics

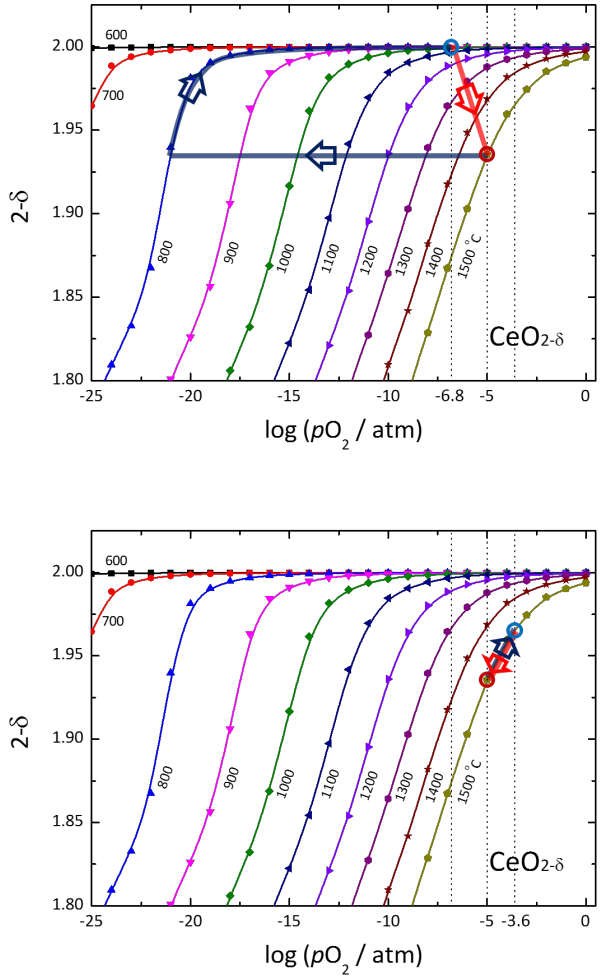

Figure 1.4: Thermochemical cycle: (a) temperature swing (1500 °C under Ar ↔ 800 °C under 20% H_2O in Ar) and (b) pressure swing (Ar ↔ 20% H_2O in Ar at 1500 °C). Red line and arrow represents the direction and reaction path for the reduction, and blue one does for the oxidation reaction. The equilibrium oxygen nonstoichiometry is from a reference [32]

reduces the overall reaction time per cycle, and thus fuel production rate per unit time will be higher. Therefore, material thermodynamics having large $\Delta\delta$ as well as fast kinetics should be satisfied simultaneously for high efficiency.

1.4 Unresolved issues and objectives of this study

The thermodynamic property of nonstoichiometric oxides has been widely investigated, usually using thermogravimetric analysis. In contrast, the understanding of kinetics in the thermochemical process is limited. The redox kinetics in thermochemical fuel production is driven by the changes in gas-phase oxygen chemical potential, corresponding to the chemical experiments described in Figure 1.2(c). Most studies addressing material kinetics using chemical experiments are limited to the specific experimental conditions, such as relatively low temperature (< 1200 °C), very small driving force (very small ΔpO_2), only for characterizing pO_2 and temperature dependence without considering the effects of H_2O/CO_2. Therefore, the kinetic properties reported to date are not directly correlated with the thermochemical process. Furthermore, in actual thermochemical applications, the oxides are structured as porous form having short diffusion length, high specific surface area, and high porosity for faster reactions as well as facile transport of reactant/product gases. An understading of the structural variation effects on the reaction kinetics is still necessary.

To sum, the unresolved issues are:

1. Rate limiting steps among bulk diffusion, surface reaction, and insufficient gas supply in thermochemical process conditions
2. The correlation between material morphology and kinetics/rate limiting steps
3. Material-kinetic property of oxides at high (> 1200 °C) and moderate (~ 700 °C) temperatures
4. The effects of H_2O/CO_2 as oxidants on oxidation kinetics
5. The kinetic behavior under large driving force (large ΔpO_2)

In chapter 2, the interplay between material morphology, gas flow rate, and inherent material properties (equilibrium nonstoichiometry and kinetic properties) affecting kinetics as well as on the overall rate-limiting factor is investigated with respect to temperature.
In chapter 3, we discuss the validity of one of the chemical experiments, total electrical conductivity relaxation (ECR) technique, and characterize the kinetic properties

of ceria ($CeO_{2-\delta}$) having well-defined geometry at extremely high temperature (1400 °C) under sufficiently high gas flow rates to overcome gas-phase limitations. In addition, the effect of pH_2O is investigated at the same temperature (1400 °C). More specifically, how pH_2O is correlated with the surface reaction along oxidation is addressed via ECR tehcnique.

In chapter 4, we discuss another relaxation technique: the mass relaxation via piezocrystal mass sensor. It does directly measure the oxygen concentration in the material, and thus this approach is more appropriate for investigating the kinetic behavior under large driving force without assumptions.

In chapter 5, we discuss the redox kinetic behavior under large driving force investigated by mass relaxation technique at 700 °C. Mechanistic consideration and numerical calculation for the understanding of the experimentally obtained kinetic behavior are shown.

Chapter 2

THE EFFECTS OF TEMPERATURE, FLOW-RATE, AND MORPHOLOGY ON REDOX KINETICS

2.1 Introduction

The redox behavior of non-stoichiometric oxides is central to a vast range of energy and environmental technologies, from fuel cells, [33–36] permeation membranes and batteries, [37–40] to photoelectrochemical cells and catalytic converters. [41, 42] Nonstoichiometric oxides have received particular attention in the context of solar-driven thermochemical production of fuels. [6, 28, 43] This technology relies on the capacity of such oxides to accommodate large swings in oxygen content in response to changes in temperature and/or changes in gas-phase oxygen chemical potential. In many of these applications, rapid response is essential to achieving high efficiency. Consequently, the oxides are often structured as mesoporous or microporous forms having relatively short bulk diffusion lengths, high specific surface area on which reactions can occur, and accessible porosity for facile transport of reactant and product gases. [44–46] For thermochemical fuel production, large porosity is further desirable for promoting radiative heat transfer. [47–50]

Clear identification of the rate-limiting step in a process involving reaction on or with a porous oxide of random morphology presents serious challenges. Two key material properties in this context are the bulk diffusion coefficient and the surface reaction constant, [51, 52] knowledge of which informs the design of optimal architecture. Electrical conductivity relaxation (ECR) methods have been widely employed to measure these properties, [21–23, 27] but the analytical solutions required for treating the relaxation profiles are generally available only for samples with simple geometries. In an ECR experiment, the material is subjected to a step change in gas-phase oxygen partial pressure (pO_2) and the rate at which the oxygen nonstoichiometry (δ) in the oxide changes is tracked by a measurement of the conductivity. It has recently been recognized that even where the sample geometry has been appropriately controlled, gas-flow dynamics can play a critical role in the observed relaxation behavior. Specifically, instead of being limited by bulk diffusion or surface reaction, the response can be limited by the rate at which

the reactant gas is supplied to the material, a phenomena which becomes dominant when the gas flow rate is low relative to the quantity of reactive oxide. [53] Significantly, such gas-limited response has also been observed during thermochemical fuel production, with high-temperature hydrogen production rates from porous ceria (resulting from the reaction of reduced ceria with steam) being proportional to the flow rate of the reactant gas. At lower temperatures, surface reaction kinetics were found to overtake gas-flow limitations as the overall rate-limiting factor. [30] These observations suggest a significant interplay between morphology, gas flow rate, and inherent material properties in establishing the rate at which porous oxides interact with a flow of reactant gases.

Here, with the aim of deconvoluting the various factors specified above, we extensively investigate the effects of morphology, temperature, and gas flow rate on the global redox kinetics of porous ceria, a model system using the electrical conductance relaxation method. A theoretical framework for predicting the temperature, morphology and flow-rate dependence of the relaxation behavior is presented, which is then compared to the experimental results. The experimental work is performed using several types of structures, including reticulated porous ceria, which has attracted attention for its potential to support high solar-to-fuel conversion efficiencies in solar-driven thermochemical fuel production. [47, 50, 54]

2.2 Theory: Electrical Conductance Relaxation of Porous Oxides

We treat the case in which a porous, non-stoichiometric oxide is subjected to a small step change in pO_2 at a fixed temperature. The perturbation serves as a chemical driving force to change the oxygen content in the material, and thereby its electrical conductivity. In the ideal scenario, the oxygen concentration in the gas, including the regions within the pores of the sample, is spatially uniform. In the limit of a low flow rate of reactant gas supplied to the oxide, the solid changes oxidation state as quickly as the gas can provide reducing (or oxidizing) power. The solid is thus in quasi-equilibrium with the gas phase and operates within what has been termed the thermo-kinetic limit. [30, 55] At high gas flow rate, the material response can no longer keep pace with the rate at which the reactant species are supplied, and the change in oxidation state is limited by material kinetic factors: surface reaction rate

and/or bulk solid-state diffusion. The material in this case operates in the material-kinetic limited regime. We consider these extreme regimes below, recognizing that material behavior in the real experiment may be dictated by a combination of rate-limiting factors, depending on gas flow rate (relative to the quantity of oxide), surface reaction constant, bulk diffusivity, and material microstructure.

2.2.1 Regimes of limiting behavior

In the thermo-kinetic limit (gas-phase limit), the surface reaction rate and bulk diffusivity are so fast as to have no impact on the overall reaction rate between oxide and gas. We have recently presented an analytical treatment of the physical situation in which the flow rate is sufficiently low that the change in material oxidation state is limited by the capacity of the gas to supply/remove oxygen from the sample.[30] Under such conditions the change with time in oxygen non-stoichiometry, δ, of a reactive oxide is described by

$$\frac{\partial \delta}{\partial t} = \frac{2F}{n_{\mathrm{CeO}_x}} \left(\frac{p\mathrm{O}_2(\delta) - p\mathrm{O}_2^{in}}{P_{\mathrm{tot}} - p\mathrm{O}_2(\delta)} \right) \tag{2.1}$$

where F is molar flow rate of gas, n_{CeO_x} is the total moles of the oxide (taken here to be ceria), P_{tot} is the total pressure of gas, and $p\mathrm{O}_2^{\mathrm{in}}$ is the oxygen partial pressure supplied upon application of the perturbation. The term $p\mathrm{O}_2(\delta)$ is the time-dependent oxygen partial pressure of the gas inside the reaction chamber, in equilibrium with the solid of oxygen content δ. By definition, δ varies with time from the initial to final state, and hence $p\mathrm{O}_2(\delta)$ also varies with time. The expression given in Eq.(2.1) is arrived at by applying an oxygen mass balance requirement to the system. It is valid when (in addition to effectively instantaneous equilibration in the solid state) (1) the oxygen content in the oxide is spatially homogeneous, and (2) the oxygen partial pressure in the gas phase within the chamber is also spatially homogenous (*i.e.,* perfect mixing within the confines of the reaction chamber).

This result can be used to derive the conductance relaxation behavior under gas phase-limited kinetics. If $p\mathrm{O}_2(\delta) \ll P_{\mathrm{tot}}$, Eq.(2.1) can be simplified to

$$\frac{\partial \delta}{\partial t} \approx \frac{2F}{P_{\text{tot}} n_{\text{CeO}_x}} \left(p\text{O}_2(\delta) - p\text{O}_2(\delta_f) \right) \tag{2.2}$$

where it is recognized that $p\text{O}_2^{\text{in}}$ corresponds (irrespective of the simplification) to the equilibrium oxygen partial pressure of the material with the oxygen nonstoichiometry of the final state, and thus $p\text{O}_2^{\text{in}} = p\text{O}_2(\delta_f)$. Since the oxygen partial pressure change, $p\text{O}_2(\delta) - p\text{O}_2(\delta_f)$, is very small in a relaxation measurement, Eq.(2.2) can be further simplified by taking a Taylor expansion,

$$\frac{\partial \delta}{\partial t} \approx \frac{2F}{P_{\text{tot}} n_{\text{CeO}_x}} \left(\left. \frac{\partial p\text{O}_2(\delta)}{\partial \delta} \right|_{\delta=\delta_\text{f}} \right) (\delta - \delta_\text{f}) = -\text{Z}\,(\delta - \delta_\text{f}) \tag{2.3}$$

where Z is defined as

$$\text{Z} = \frac{2F}{P_{tot} n_{\text{CeO}_x}} \left(- \left. \frac{\partial p\text{O}_2(\delta)}{\partial \delta} \right|_{\delta=\delta_\text{f}} \right) \tag{2.4}$$

The solution to this 1$^{\text{st}}$ order differential equation is a simple exponential expression. For a material in which the conductivity is proportional to the oxygen concentration (as would be expected under a sufficiently small perturbation in $p\text{O}_2$) the normalized conductance will follow the same form, given as:

$$\frac{G(t) - G_\text{i}}{G_\text{f} - G_\text{i}} = \frac{c_\text{O}(t) - c_{\text{O,i}}}{c_{\text{O,f}} - c_{\text{O,i}}} \approx 1 - \exp\left(-\frac{t}{\tau}\right) \tag{2.5}$$

where G is the conductance, G_i and G_f are the initial and final conductance values, respectively, t is time, and τ is the relaxation time constant, defined according to

$$\frac{1}{\tau} = \frac{2}{P_{tot}} \frac{F}{n_{\text{MO}_x}} \left(- \left. \frac{\partial p\text{O}_2(\delta, T)}{\partial \delta} \right|_{\delta=\delta_\text{f}} \right) \tag{2.6}$$

where P_{tot} is the total pressure, F is the molar flow rate of gas, n_{MO_x} is the number of moles of oxide, $p\text{O}_2(\delta,\text{T})$ is the equilibrium oxygen partial pressure of a gas with the oxide at a nonstoichiometry δ at temperature T, and δ_f is the final equilibrium nonstoichiometry of the oxide. The term $p\text{O}_2(\delta,\text{T})$, a material specific quantity, which expresses the gas-phase oxygen partial pressure at which the material attains an equilibrium oxygen nonstoichiometry of δ. It is to be emphasized that the relaxation time of Eq. (2.6) is entirely unrelated to a conventional reactor flush time, a time

constant which reflects the characteristics of the experimental configuration, but bears no relationship to the thermodynamic properties of the materials under study. Moreover, while theoretically expected, the thermo-kinetic characteristic time has not been experimentally observed in a relaxation experiment. [53]

From the form on Eq. (2.6), it is immediately evident that increasing the normalized gas flow rate (flow rate per unit oxide) monotonically decreases the relaxation time. However, this relationship cannot hold indefinitely. At extremely large normalized flow rates, material kinetic factors, such as the surface reaction step and/or bulk diffusion, ultimately become important. Of these, the relaxation behavior in the surface reaction limited regime of a material with a simple geometric shape is well known. The relaxation will follow an exponential profile, similar in form to Eq. (2.5), with a characteristic time that depends on sample dimensions. It can be shown that a porous material behaves similarly, where the relevant dimension is the volume specific surface area (SSA) or *A/V*, where A is the total surface area of the porous material and V is its volume (excluding pores). In this case, the rapid bulk diffusion implies the absence of a concentration gradient within the solid phase, expressed as

$$c_{\mathrm{O}}(\overrightarrow{r}, t) = c_{\mathrm{O}}(t) \left(\overrightarrow{r} \in R \right) \tag{2.7}$$

where $\vec{r}$ is the position variable and R is the region inside the oxide. When the final $p\mathrm{O}_2$ surrounding the oxide, which drives the oxygen concentration to the new equilibrium state of $c_{\mathrm{O,f}}$ $(= c_{\mathrm{O}}(\infty))$, is fixed throughout the relaxation process, and the surface reaction is first order in oxygen concentration, the oxygen flux (J) at the surface of and inside the oxide is

$$J(\overrightarrow{r}, t) = \begin{cases} k_{\mathrm{Chem}}(t) \left[c_{\mathrm{O,f}} - c_{\mathrm{O}}(t) \right] & \left(\overrightarrow{r} \in S \right) \\ J(t) \approx 0 & \left(\overrightarrow{r} \in R \text{ and } \overrightarrow{r} \notin S \right) \end{cases} \tag{2.8}$$

where k_{Chem} is the surface reaction rate constant, and S is the surface domain of the oxide. In the absence of sources or sinks of oxygen, the rate of change in concentration in the volume element is determined by the flux of oxygen entering it (the continuity relation):

$$\frac{\partial c_{\mathrm{O}}(t)}{\partial t} = \frac{\partial J(\overrightarrow{r}, t)}{\partial \overrightarrow{r}} \tag{2.9}$$

The rate of change in concentration over the total volume of the oxide can be obtained by inserting Eq. (2.8) for the flux into Eq. (2.9) and then integrating, giving

$$\int_R \frac{\partial c_{\mathrm{O}}(t)}{\partial t} dV = \int_S k_{\mathrm{Chem}}(t) \left[c_{\mathrm{O,f}} - c_{\mathrm{O}}(t) \right] dA \tag{2.10}$$

$$\frac{\partial c_{\mathrm{O}}(t)}{\partial t} = \frac{k_{\mathrm{Chem}}(t) A}{V} \times \left[c_{\mathrm{O,f}} - c_{\mathrm{O}}\,(t) \right] \tag{2.11}$$

where V and A are, respectively, the volume and surface area of the oxide. The solution to Eq. (2.11) has a simple exponential form, analogous to that of Eq. (2.5). If the total conductance again changes linearly with oxygen concentration, the normalized conductance is then

$$\frac{G(t) - G_{\mathrm{i}}}{G_{\mathrm{f}} - G_{\mathrm{i}}} = \frac{c_{\mathrm{O}}(t) - c_{\mathrm{O,i}}}{c_{\mathrm{O,f}} - c_{\mathrm{O,i}}} = 1 - \exp\left(-\frac{k_{\mathrm{Chem}} A}{V} t \right) = 1 - \exp\left(-\frac{t}{\tau} \right) \tag{2.12}$$

where the time constant is now defined by

$$\frac{1}{\tau} = \left(\frac{k_{Chem} A}{V} \right) \tag{2.13}$$

This result has been presented without derivation by Kim *et al.* [56] In this limit, material thermodynamics, gas flow rate, and sample mass no longer play a role. However, as has been noted previously, the relaxation profiles in the thermo-kinetic and surface-reaction limited regimes are identical in functional form. [53]

If the bulk diffusion lengths of the oxide are long relative to the characteristic length defined by $D_{\mathrm{Chem}}/k_{\mathrm{Chem}}$, where D_{Chem} is the chemical diffusion coefficient, then diffusion will play a role in determining the overall relaxation profile. In such a case, the oxygen concentration in the solid will depend on position as well as time. Accordingly, the solution to the concentration profile will depend sensitively on the architecture of the porous material. Although a general solution cannot be written, in principle, a finite element treatment that accounts for Fickian diffusion in the bulk along with a reaction flux across the oxide-gas interface could be used to describe the relaxation behavior of a material with arbitrary pore architecture. In light of known solutions for simple geometries, [57] such treatment would be unlikely to produce an exponential function of the form of Eq. (2.5).

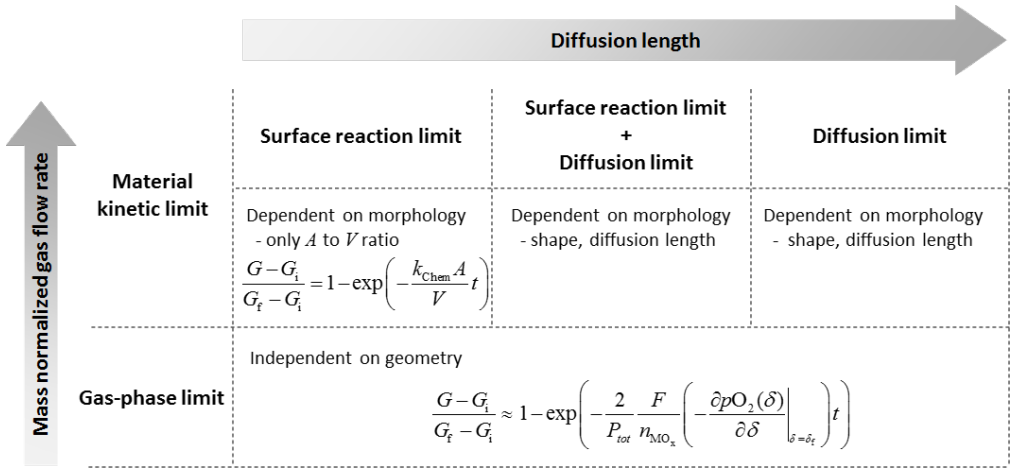

Figure 2.1: Phase space of parameters establishing the rate limiting step(s) in the reaction of an oxide with a flowing reactant gas, and regimes of limiting behavior. With increasing normalized gas flow rate material kinetic factors become dominant over thermodynamic factors. Within the material kinetic regime, increasing diffusion length causes diffusion to become dominant over surface reaction.

The overall phase space for the various regimes considered is presented in Figure 2.1, along with the functional form of the relaxation profile for each regime. Because relaxation influenced by bulk-diffusion limitations cannot generally be described by a simple exponential profile, evidence of diffusion effects can be detected simply from profile analysis. However, extraction of the diffusion coefficient would be extremely challenging. This challenge is conveniently circumvented when evaluating typical porous ceria structures for thermochemical fuel production. All studies to date indicate that material kinetic limitations arise from low surface reaction rates, with no influence of bulk diffusivity. [8] Accordingly, we focus hereafter on thermo-kinetic and surface reaction limited behaviors.

2.2.2 Influence of flow rate, morphology, and temperature on relaxation behavior

In the thermo-kinetic regime the inverse of the characteristic relaxation time is linearly proportional to the normalized gas flow rate. The slope relating the two is readily computed from knowledge of the material thermodynamic properties. Specifically, from Eq. (2.6), one obtains

$$\frac{d(1/\tau)}{d(F/n_{\mathrm{MO_x}})} = \frac{2}{P_{tot}}\left(-\left.\frac{\partial p\mathrm{O_2}(\delta,T)}{\partial\delta}\right|_{\delta=\delta_\mathrm{f}}\right) = \frac{2}{P_{tot}}\frac{p\mathrm{O_2}(\delta_\mathrm{f},T)}{\delta_\mathrm{f}}\left(-\left.\frac{\partial \ln p\mathrm{O_2}(\delta,T)}{\partial \ln\delta}\right|_{\delta=\delta_\mathrm{f}}\right) \tag{2.14}$$

At the temperatures and oxygen partial pressures of interest here the slope decreases with temperature. This result which can be understood by recognizing that, although the slope of log δ vs. log $p\mathrm{O_2}$ (atm) is approximately constant (between 1/5 and 1/6), [32, 58] under the conditions of interest, the absolute value of increases . The relaxation time thus depends on the normalized flow rate as shown schematically in Figure 2.2(a). For reference, the value of $\left.\frac{\partial p\mathrm{O_2}(\delta,T)}{\partial\delta}\right|_{\delta=\delta_\mathrm{f}}$ at a $p\mathrm{O_2}$ of 8.2×10^{-4} atm (as used in this work) is presented in Supplemental information (Figure 2.14).

In the surface reaction limited regime, one can anticipate the behavior of $1/\tau$ vs. normalized flow rate at different temperatures for two materials with differing specific surface areas to appear as shown in Figure 2.2(b). The relaxation time constant in both cases is independent of flow rate and decreasing with increasing temperature. However, that of the oxide with smaller specific surface area (SSA) is larger than that for the other. Here it is assumed that the surface reaction constant increases monotonically with temperature, as is typical. [59, 60]

The experimentally observed relaxation time constant will always correspond to the larger of the two values of τ implied by the thermo-kinetic and surface reaction limited regimes (i.e., the slower process will be rate-limiting). Thus, the overall $1/\tau$ will be given as Figure 2.2(c), with a transition from gas-limited to material-kinetic-limited behavior with increasing flow rate. The schematic further reveals that the transition point between the two regimes shifts to higher flow rate with increasing temperature or increasing specific surface area (with all else held equal).

The interplay of temperature, gas flow rate and surface area are more clearly revealed in an Arrhenius representation. To that end, from expressions (2.6) and (2.13), one obtains, respectively, the logarithmic relations

$$\log\left(\frac{1}{\tau}\right) = \log\left(k_{\mathrm{Chem}}(\delta,T)|_{\delta=\delta_\mathrm{f}}\right) + \log\left(\frac{A}{V}\right) \tag{2.15}$$

and

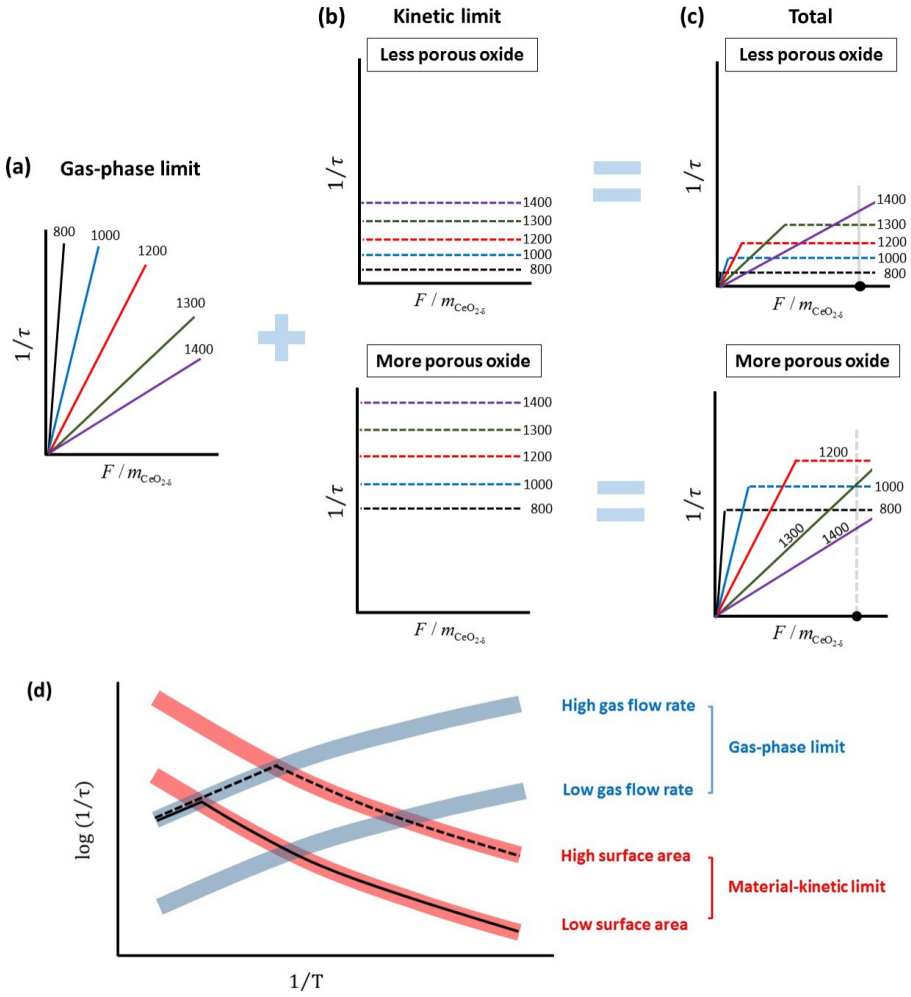

Figure 2.2: Schematic behavior of the relaxation time constant (τ): (a-c) as a function of normalized flow rate (F, where the normalization is with respect to quantity of oxide, either mass or moles) at various temperatures for oxides of low and high specific surface area, in which the redox reaction is in the regime of (a) the gas-phase limit, (b) the surface reaction limit, and (c) a combination of the gas-phase and the surface reaction limits. (d) log ($1/\tau$) as a function of temperature. The black dotted and solid lines in (d) correspond to τ for the more high and low specific surface area oxides, respectively, at the fixed flow rate marked in (c). Blue and Red thick curves are guides to the eye.

$$\log\left(\frac{1}{\tau}\right) = \log\left(-\frac{\partial pO_2(\delta,T)}{\partial\delta}\bigg|_{\delta=\delta_f}\right) + \log\left(\frac{2F}{P_{tot}n_{MO_x}}\right) \tag{2.16}$$

Here it is recognized that, in addition to its temperature dependence, k_{Chem} typically

depends also on oxygen stoichiometry (generally manifest as a dependence on pO_2); for consistency with the behavior of the gas-limited regime, we define it relative to the τ at the conclusion of the relaxation experiment. The second terms in the right-hand side of Eqs. (2.15) and (2.15) are independent of temperature (as well as being independent of oxygen partial pressure). They serve only to uniformly translate the value of $\log(1/\tau)$ along the y-axis in the Arrhenius representation, raising its value with increasing normalized flow rate or volume-specific surface area, Figure 2.2(d). Because the relaxation will be limited by the slower process, a transition from a material-kinetic-limited to a gas-limited regime will occur on heating, with the cross-over temperature being dependent on the normalized gas flow rate and the specific surface area of the oxide. Consider specifically the case in which conductance relaxation is measured as a function of temperature at the same fixed, large value of normalized gas flow rate for two materials with differing specific surface areas as indicated by the vertical lines in Figure 2.2(c). The behavior of the low SSA oxide will follow the solid black line in Figure 2.2(d), transitioning to gas-limited behavior at relatively high temperature. In contrast, the high SSA oxide will follow the dotted black line, with the transition occurring at a lower temperature. Significantly, in the gas-limited regime, the observed relaxation rate will be independent of the oxide morphology. Overall, it is evident that one must take care to understand the regime under which the measurement is performed if one is to meaningfully extract material properties.

2.3 Sample Preparation

Ceria of four different morphologies was prepared for conductance relaxation measurements: (i) a dense polycrystalline compact; (ii) a highly porous, low SSA structure with unimodal pore distribution; (iii) a highly porous structure, high SSA oxide with bimodal pore distribution; [48] (iv) and a 'less porous' monolith of large volume. The majority of the relaxation studies were performed with the two highly porous structures. For the polycrystalline compact, ceria powder (Aldrich, 211575, 99.9 % purity) was compressed under uniaxial pressure at 100 MPa, followed by cold isostatic pressing at 250 MPa. The green body was then sintered under stagnant air at 1500 °C for 10 h. The relative density of the resulting material was > 96 % of the theoretical value. The sample was cut and polished into the shape of a parallelepiped 0.79 mm × 4.71 mm × 16.3 mm in linear dimensions and 0.3930 g in mass.

The highly porous samples were reticulated porous ceramic (RPC) structures. The RPC fabrication process permits facile dimensional control at the macroscopic lengthscale. [61, 62] As is typical for RPC fabrication, a polyurethane sponge template with large scale pores, 3 mm, (Figure 2.3a) was coated with a ceramic slurry (Figure 2.3(b)). Upon removal of the polymer at high temperature, a macroporous monolith consisting of a network of struts with open porosity was obtained (Figure 2.3(c)). The starting powder for RPC preparation here was a mixture of coarse (Alfa Aesar, 11328, 5 micron powder, 99.9 %) and fine (STREM chemicals, 58-1400, < 7 nm, > 99.7 %) ceria combined in a 7:3 ratio. The powders were mixed with water in a 6:4 powder:water weight ratio, to which Darvan® 821A (Vanderbilt Minerals, 14442, 5 wt% relative to ceria) was added as a dispersant, and carboxymethyl cellulose sodium (CMC, Tokyo Chemical Industry, C0603, 0.25 wt% relative to ceria) was added as a thickening agent. To create the RPC with bimodal pore structure, hereafter RPC-50, 50 vol% carbon pore-former (STREM chemicals, 93-0601, 325 mesh, vol% relative to ceria) was added to the slurry. [48] The RPC with unimodal pore structure, preparation of which did not include this additional pore former, is hereafter referred to as RPC-00.

The slurries were ball-milled for 24 h using YSZ (yttria-stabilized ZrO_2) grinding media. After this homogenization, commercial 10 PPI (pores per inch) Polyurethane

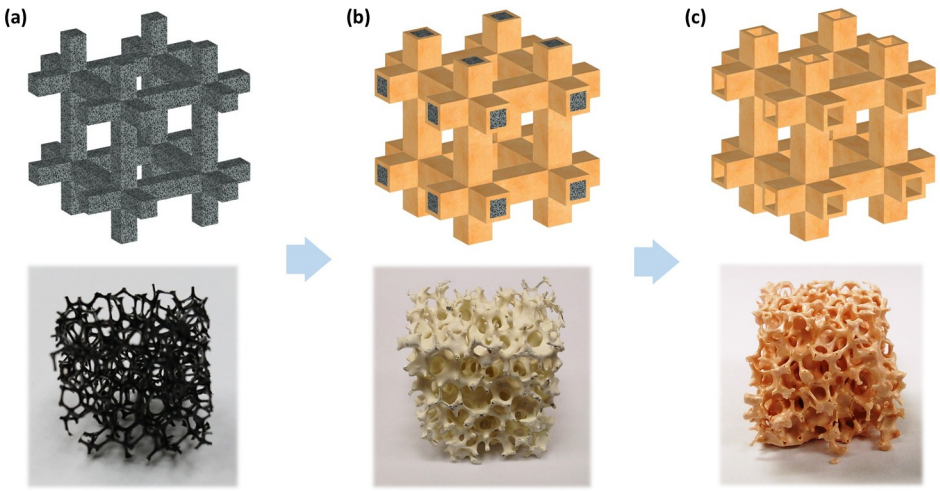

Figure 2.3: Images outlining the RPC fabrication process: (a) sacrificial polyurethane foam, (b) foam coated with ceramic slurry, and (c) final fired structure.

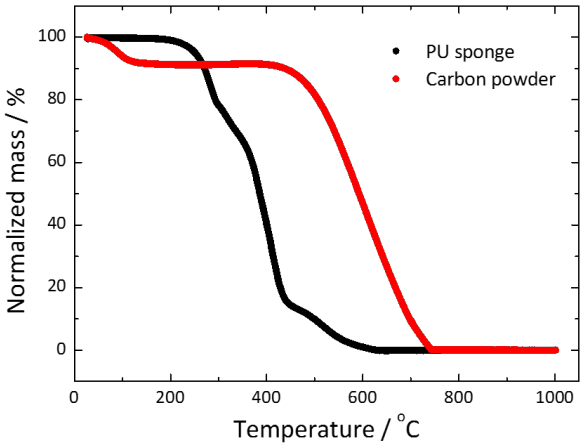

Figure 2.4: TGA profiles of polyurethane sponge and carbon powder.

(PU) sponges (Foam-Partner, Fritz Nauer AG) of cylindrical shape were immersed in the slurry and then dried at 70 °C for 1.5 h. After 4 repetitions of this coating step, the samples were fired under stagnant air to gently remove the polyurethane matrix and carbon pore-former. The heat treatment protocol was selected on the basis of the thermal decomposition behavior of the organic components as guided by thermogravimetric analysis (TGA), Figure 2.4. TG measurements were performed on polyurethane sponge and carbon powder with a mass of 110 and 41 mg, respectively, in a thermal analyzer (Netzsch STA 449 F5) using an alumina crucible. The sample heated up to 1000 °C at a ramp rate of 10 °C/min with flowing Ar (100 sccm) + air (30 sccm). Regarding the protocol, specifically, the materials were heated stepwise under stagnant air to 500 °C for RPC-00, and to 900 °C for RPC-50, at a rate of 1 °C/min with intermediate 30 min holds at 300, 325, and 500 °C. The temperature was then raised up to 1500 °C at a rate of 5 °C/min and held for 5 h. The image in Figure 2.3(c) is that of a typical structure RPC-00 structure.

The 'less porous' monolith, hereafter PM, was prepared from coarse ceria powder (Alfa Aesar, 11328). This was combined with starch (Alfa Aesar, A11961, 37.5 wt% relative to ceria) then ball-milled (YSZ milling media) for 24 h in anhydrous ethanol. After drying at 40 °C, graphite powder (Alfa Aesar, 14735, 98 wt% of ceria) was added to this mixture. The composite powder was uniaxially pressed at 40 MPa and subsequently sintered using the same heat-treatment protocol as employed for RPC-50 (stepwise heating to gently oxidize and remove organics, with final hold

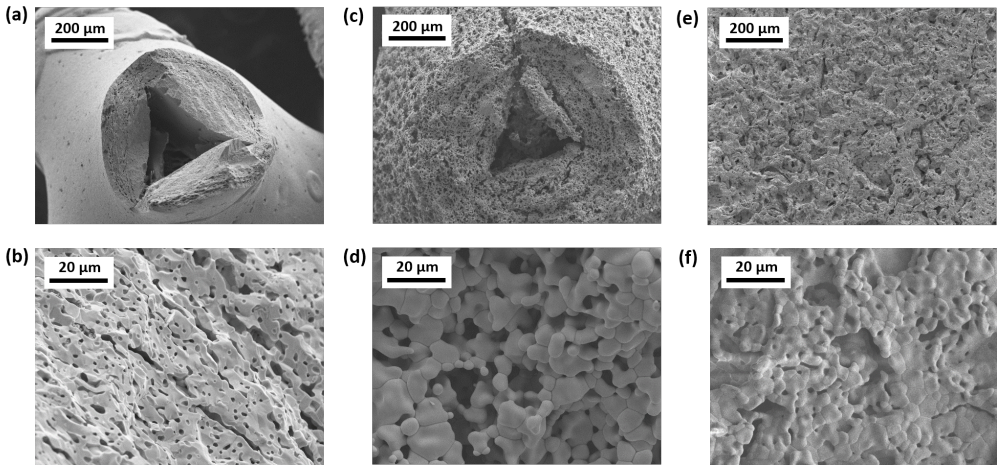

Figure 2.5: SEM micrographs of the cross-sectional fracture surfaces of porous ceria: (a)-(b) RPC-00, (c)-(d) RPC-50, and (e)-(f) PM.

at 1500 °C). The dimensions, mass, and implied porosity of the resulting structures are listed in Table 2.1.

Scanning electron microscopy images (Hitachi S4800-II cFEG SEM), Figure 2.5, reveal the three porous materials to display very different pore architectures. While the two RPCs have similar macroscopic porosities (~ 86 %), RPC-50 has a visibly larger volume-specific surface area (*A/V*) and a higher concentration of open pores within the struts. The PM has a relatively random distribution of pore sizes, with both open and closed pores evident, and porosity of 61.5 %. The ranking of the volume-specific surface area of this material relative to the two RPCs is not immediately apparent from the images. Attempts to determine *A/V* by gas absorption (BET) methods were unsuccessful due to the relatively low mass-specific surface areas. Mercury intrusion porosimetry and X-ray tomography measurements, Table 2.2, confirmed the substantially higher *A/V* of RPC-50 relative to the RPC-00. However, the results are not entirely quantitative because of assumptions about pore structure required in order to convert mercury intrusion behavior to accessible surface area, and because of the extensive image processing required to estimate specific surface area from tomographic results.

Table 2.1: Dimensions, mass, and porosity of cylindrical ceria structures. Number in parentheses indicates uncertainty in the final digit(s) as obtained from the variance between multiple measurements.

Sample	radius (cm)	height (cm)	mass (g)	porosity (%)
RPC-00	0.27(4)	1.040(9)	0.23070(5)	86(3)
RPC-50	0.245(16)	1.194(10)	0.23770(5)	85.4(14)
PM	0.4478(5)	0.267(1)	0.46660(5)	61.5(6)

Table 2.2: Volume specific surface area by Mercury porosity and X-ray tomography measurements

Sample	Mercury intrusion porosimetry (mm^{-1})	X-ray tomography (mm^{-1})
RPC-00	80	25
RPC-50	800	370

2.4 Relaxation Behavior: Methods, Results, and Discussion

2.4.1 Methods

DC conductance relaxation profiles were measured in a small volume reactor ($\sim$ 23 cm^3). The dense rectangular sample was evaluated using a true four-probe configuration, whereas the porous materials were measured in quasi-four-probe arrangements, Figure 2.6. Pairs of contacts were applied to the distant ends of the dense sample by tightly wrapping Pt wires around notches made at the far ends of the sample, Figure 2.6(a). For the two RPCs, struts at either end were wrapped with Pt wire (Figure 2.6(b)), and Pt paste (Platinum ink A3788A, BASF Catalysts) was then applied to the contact points. In the case of the PM, two small holes ($\sim$ 1 mm in diameter) were drilled through the sample at opposing sides close to the circumference. As with the RPCs, Pt wires were passed through these holes, firmly secured, and then contacted to the oxide using Pt paste, Figure 2.6(c). For all experiments, the pO_2 was measured *in situ* using a zirconia based oxygen sensor (SIRO2 C700+, Ceramic Oxide Fabricators, Australia) placed approximately 2 cm downstream of the sample.

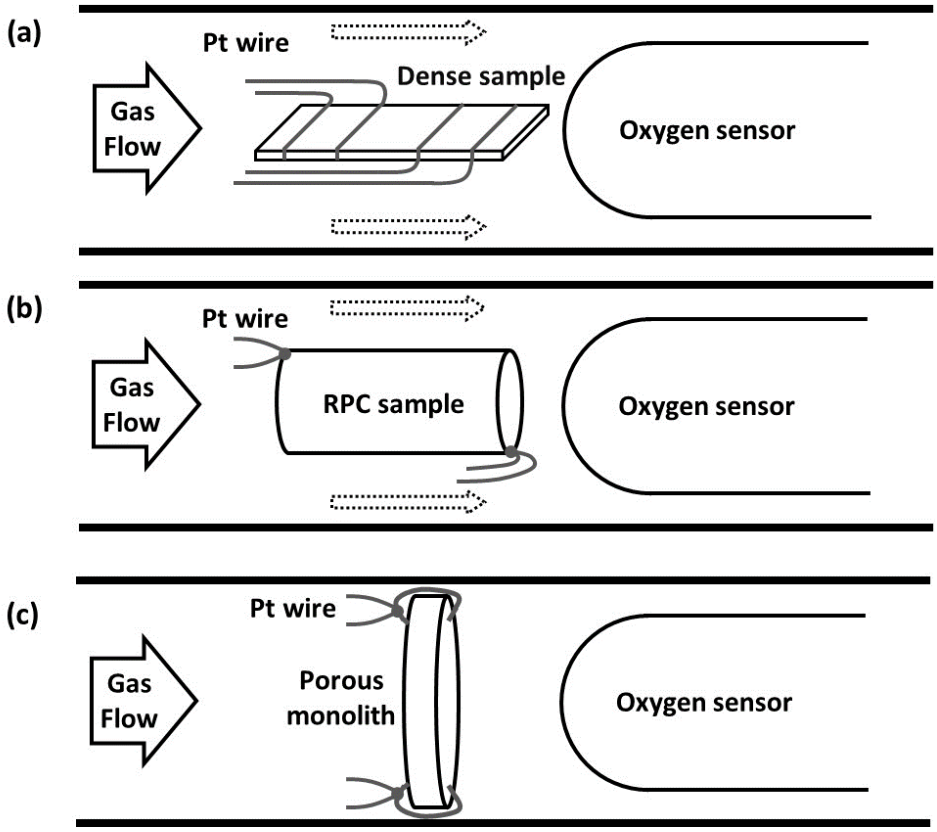

Figure 2.6: Schematics of electrical conductance relaxation test system: (a) dense polycrystalline bulk, (b) RPCs, and (c) porous monolith samples.

The conventional dense sample was utilized to measure k_{Chem} as a function of temperature over the range 800 to 1400 °C under high gas flow conditions at which gas-limitations are overcome, using specifically, a flow rate of 300 standard cubic centimeters per minute (sccm), equating to 763 sccm/g or 1.31×10^5 sccm/mol. The conductance profiles were recorded upon abruptly changing the oxygen partial pressure from 1.5×10^{-3} to 7.9×10^{-4} atm, achieved using digitally controlled mass flow controllers that provided predetermined mixtures of Ar and O_2. We define the oxygen partial pressure in the final state as that of the measurement, consistent with the expression in Eq. (2.6). The response of the two RPCs was measured using the same step change in pO_2 and same range of temperatures (800, 1000, 1200, 1300, and 1400 °C), but with the flow rate varied from 150 to 500 sccm, implying mass and mole normalized flow rates of ~ 600 to ~ 2100 sccm/g or ~ 1.0×10^5 to ~ 3.6 $\times 10^5$ sccm/mol, respectively. The PM sample was evaluated to provide additional flow rate dependent data at 1400 °C. The step change in pO_2 was $1.6 \times 10^{-3} \rightarrow 8.2$ $\times 10^{-4}$ atm, and the flow rate was varied from 50 to 400 sccm. Because a larger

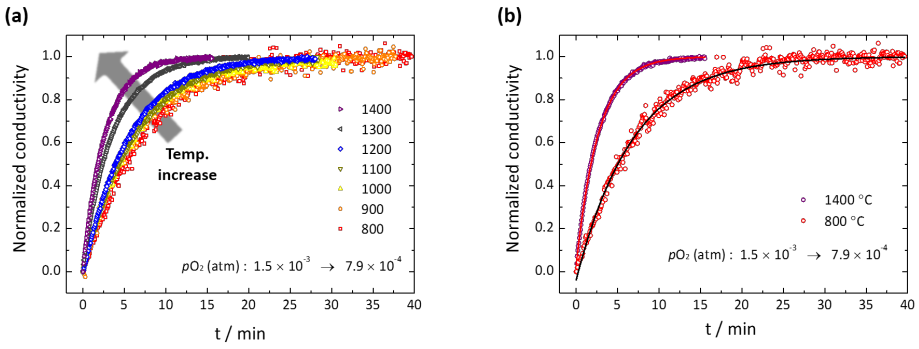

Figure 2.7: Conductivity relaxation profiles for bulk ceria under the small step change in pO_2 ($1.5 \times 10^{-3} \rightarrow 7.9 \times 10^{-4}$ atm) from (a) 800 to 1400 °C. (b) The profiles at 800 and 1400 °C are shown with the best fit result (solid lines).

oxide sample was employed, this provided access to smaller values of oxide mass normalized flow rates (107 to 857 sccm/g), without having to decrease the flow rate to levels that jeopardize pO_2 control.

2.4.2 Results and Discussion

All the normalized relaxation profiles measured in this work were described well by a simple exponential decay function, as given generically in Eq. (2.5), indicating the absence of bulk diffusion effects on the kinetic response. For the dense sample, measured as a function of temperature, Figure (2.7), the fits yielded reduced R^2 values > 0.993 and percent error of 0.8 %. The surface reaction constant obtained from this analysis, taking $\tau = a/k_{\text{Chem}}$, where $2a$ is the thickness of the sample in the thinnest direction, is shown in Figure (2.8). The value measured at 1400 °C is consistent with the reported value in reference [53], performed using a dense compact at this single temperature. The surface reaction constant as measured here generally increases with temperature, with a change in slope on the Arrhenius plot at ~ 1180 °C. Further discussion of the behavior of k_{Chem} and comparison to the sparse literature available on the surface properties of ceria at this high temperature is presented in the SI (Figure 2.16). Of relevance here is that the trend with temperature aligns with the discussion of the expected impact of changing parameters on the measured relaxation time.

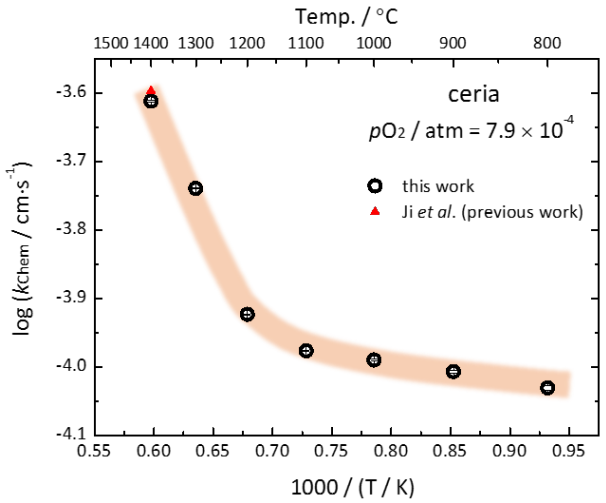

Figure 2.8: Surface reaction constant k_{Chem} of ceria as a function of temperature obtained from the best fits to the relaxation profiles as shown in Figure 2.7. Shown for comparison is the result in reference [53]. Colored band is a guide to the eye.

The normalized conductance relaxation profiles for RPC-00 and RPC-50 are presented in Figure 6 for selected temperatures and for the highest and lowest gas flow rates examined. The reduced R^2 values for fits of the entire range of RPC profiles against Eq. (2.5) were > 0.992 and percent error of was < 1.9 %. At 800 and 1000 °C, the relaxation characteristics of both RPC-00 and RPC-50 are insensitive to flow rate, indicating that at these temperatures, the process is in the surface reaction limited regime for all flow rates of 200 sccm and higher (850 sccm/g). At 1200 °C, only RPC-00 continues to display a flow rate independent response, whereas at 1400 °C the profiles of both the RPC-00 and RPC-50 are flow rate dependent, with higher flow resulting in faster relaxation, indicative of entry into the thermo-kinetic regime.

The relaxation times measured over the broad range of temperatures and flow rates examined are summarized in Figure 2.10. The trends generally follow the predicted behavior (Figure 2.2(c)). The $1/\tau$ values measured from RPC-00 are largely independent of flow rate for temperatures up to 1300 °C, whereas they increase monotonically with flow rate at 1400 °C. In the case of RPC-50, a flow-rate independent $1/\tau$ is similarly evident at lower temperature. At 1200 °C, $1/\tau$ is initially linearly dependent on flow rate, then sharply transitions to a region where it is flow-rate independent. At the higher temperatures, the relaxation behavior is always dependent on the gas supply for the flow rates probed, similar to RPC-00. The

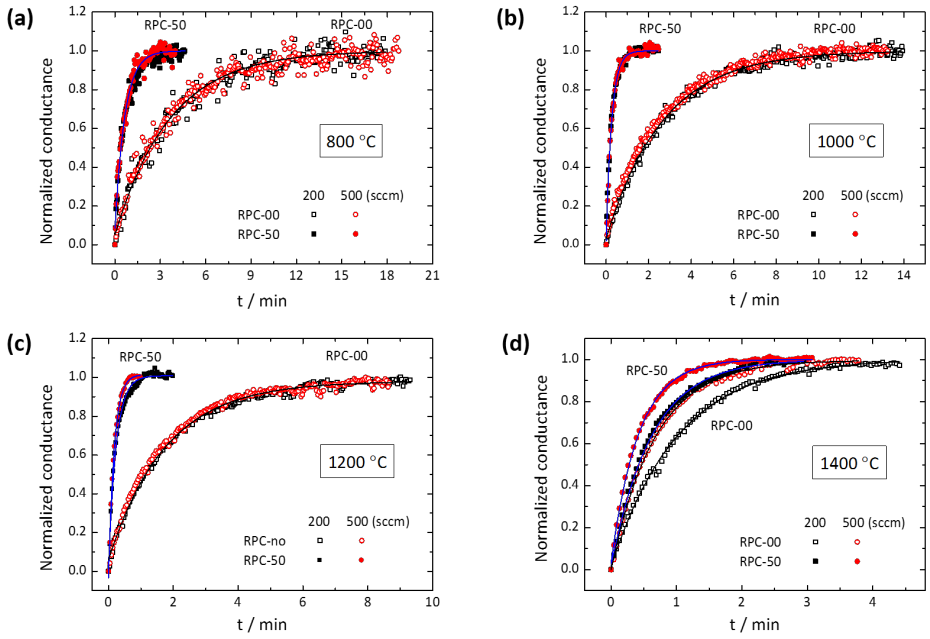

Figure 2.9: Conductance relaxation profiles at flow rates of 200 and 500 sccm for RPC-00 and RPC-50 (approximately 850 and 2100 sccm/g, respectively) under a small step change in pO_2 ($1.5 \times 10^{-3} \rightarrow 7.9 \times 10^{-4}$ atm) at (a) 800, (b) 1000, (c) 1200, and (d) 1400 °C, respectively. Solid lines are the best fit exponential decay function (Eq. (2.12) or (2.5)).

data for a selected high and selected low flow rate are recast in Arrhenius format in Figure 2.11. The results again follow the predicted behavior (Figure 2.2(d)). At low temperatures, at which the response is governed by the surface reaction rate, the sample with higher surface area has a relaxation time constant 5-6 times greater than that with low surface area, and the response times for both samples decrease with temperature. At high temperature, in the gas-phase limit, the relaxation time constants of the two types of samples approach one another, and the response times increase with temperature. Thus, if one inadvertently assigned the response to the surface reaction behavior, one would obtain, in this high temperature, low gas flow-rate regime, a peculiar material which displays a surface reaction constant that decreases with temperature.

Beyond their temperature dependence, the absolute values of the relaxation time constants in the gas-phase limited regime merit discussion. In principle, in this regime the two types of materials should relax at precisely the same rate, and the time constant can be precisely predicted from the thermodynamic properties of the

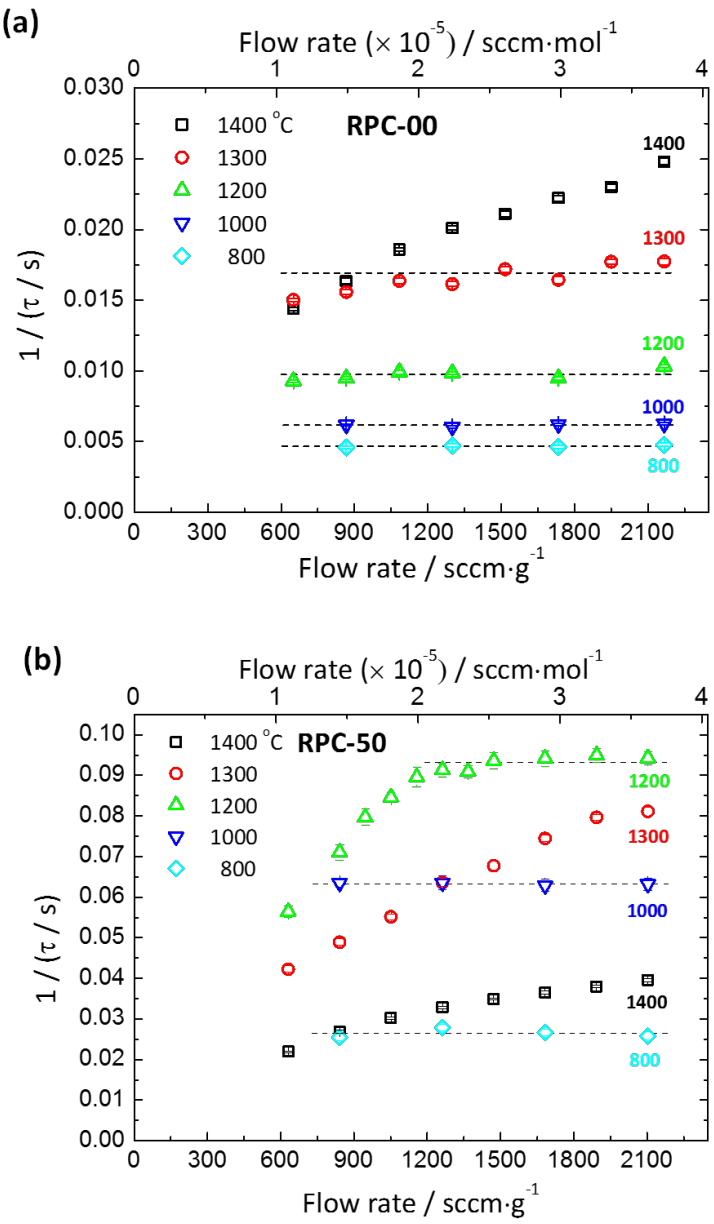

Figure 2.10: Relaxation time constant for a small step change in pO_2 ($1.5 \times 10^{-3} \rightarrow 7.9 \times 10^{-4}$ atm) extracted from fits of the type shown in Figure 2.9 as a function of flow rate at several temperatures in the ragne of 800 ~ 1400 °C for (a) RPC-00 and (b) RPC-50. Dotted lines show the average value in the material-kinetic regime.

oxide according to Eq. (2.6). Examination of Figure (2.10) and Figure (2.11) and reveals, however, that the two materials do not relax at the same rates as each other in the high temperature and low gas-flow rate regime, and nor does either match the thermodynamic prediction. For example, at 1400 °C and a mass-normalized flow rate of 640 sccm/g, the relaxation time constants for the RPC-00 and RPC-50 sam-

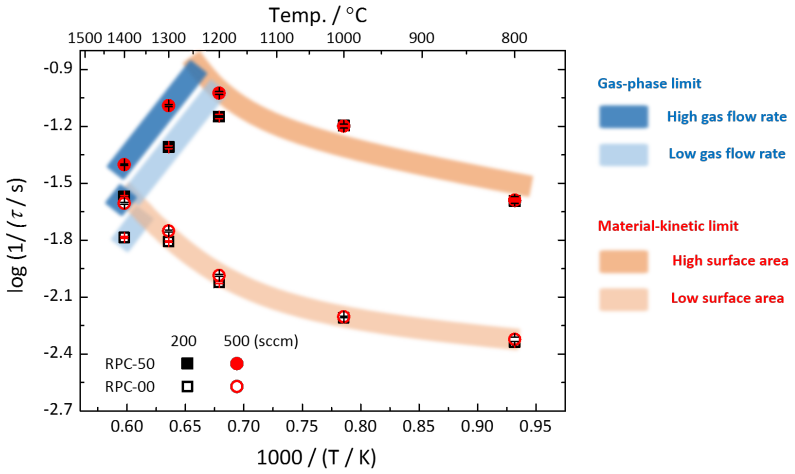

Figure 2.11: log $(1/\tau)$ as a function of temperature for ceria RPCs at gas flow rates of 200 and 500 sccm, for which raw relaxation profiles are presented in Figure (2.10). Symbols are the experimental result. Blue and orange shaded bands are guides to the eye.

ples are ~ 70 and ~ 46 s, respectively, as compared to the expected value of 21.6 s. A potential reason for this discrepancy lies in the details of the sample arrangement in the reaction chamber. Eqs. (2.5) and (2.6) are valid when the gas surrounding the sample is uniform in composition, effectively attaining the exit gas composition instantaneously on entry into the reaction chamber. However, the cross-sectional areas of the RPC samples used for this study, with radii of ~ 0.26 cm, were substantially smaller than the cross-sectional area of the reaction chamber, with radius 0.5 cm, suggesting that some gas may flow past the sample at a distance far enough away that the gas is not 'felt' by the oxide. Furthermore, the large pores in the RPCs may result in composition gradients even within the macroscopic volume of the sample.

Recognition of the possible impact of unfavorable gas flow dynamics on the measurement of the relaxation time in the gas-limited regime motivated examination of the PM sample, which has a larger cross-sectional area (~ 80 % that of the chamber vs. ~ 25 %), smaller pores, and lower porosity than the RPC samples, Table 2.1. Similar to the other samples, fits to the PM relaxation profiles according to Eq. (2.5) yielded R^2 values > 0.996 and percent error < 1.4 % (Figure 2.12). The time constants obtained at 1400 °C from the two RPCs and the PM are compared in Figure (2.13) to that of the theoretically predicted value. Faster relaxation time for the PM sample over the RPCs is clearly evident, as is a sharper transition between

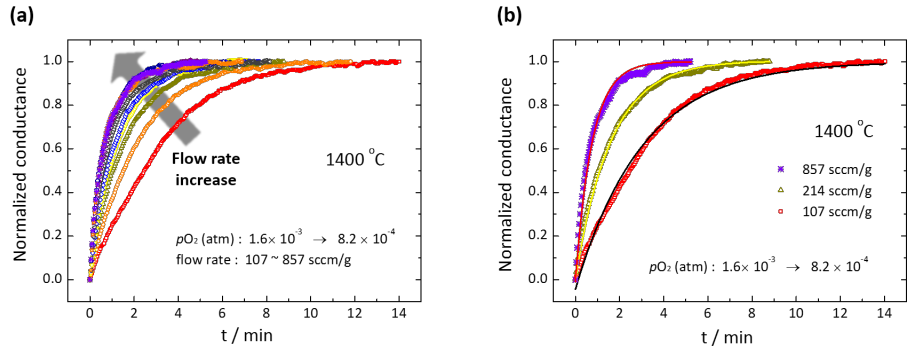

Figure 2.12: Conductance relaxation profiles for PM sample under a small step change in pO_2 ($1.6 \times 10^{-3} \rightarrow 8.2 \times 10^{-4}$ atm) at 1400 °C (a) in the range of the flow rate from 107 to 857 sccm/g. (b) The profiles at flow rates of 107, 214 and 857 sccm/g (50, 100, 400 sccm, respectively) are shown with the best fit result (solid lines).

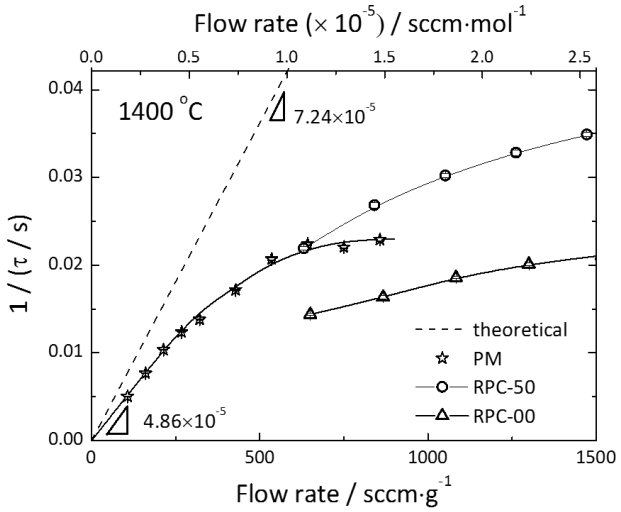

Figure 2.13: Relaxation time constant as a function of flow rate at 1400 °C for the three different types of porous ceria structures of this study, compared to the theoretical value expected under gas-limited kinetics. The latter is computed according to Eq. (2.14) using the thermodynamic data of Panlener *et al.* [32] Solid lines are guides to the eye.

gas-flow and surface reaction limited regimes. Nevertheless, even the PM does not relax as quickly as expected in the thermokinetic regime, suggesting limitations due to gas flow dynamics have not been fully resolved. The faster response time of the RPC-50 sample over the RPC-00 sample within the gas-limited regime may be due to the fact that the large-scale pores in RPC-00 are larger than those in RPC-50 (the former has thinner, denser struts). Larger pores may generate substantial gas-phase

compositional non-uniformity within the volume of the RPC-00 structure. Further discussion is provided in Supplemental information (Figures 2.17 and 2.18). Overall, the response rates of these porous materials point to the value of engineering pore structure and morphology and macroscopic material dimensions to manipulate gas flow dynamics. However, within the thermo-kinetic regime increasing specific surface area cannot directly influence the response rate by simply providing a greater number of reaction sites.

Returning to the behavior in the material-kinetic regime, here the relaxation times obtained from the dense and porous structures are expected to be related according to

$$\frac{\tau_d}{\tau_p} = \frac{a_d A_p}{V_p} \tag{2.17}$$

where subscripts d and p signify dense and porous, respectively. The measured relaxation times for the RPC-00 structure in the material-kinetic region, Figure 2.10(a), are 2 to 4 times smaller than those of the dense sample (as measured to generate Figure 2.8), suggesting a volume specific surface area of 5 to 10 mm^{-1}. The analogous amplification for the RPC-50 is 12 to 32 times, suggestive of a volume specific surface area of 30 to 80 mm^{-1}. These values would equate to the close-packing of particles with diameters of 300-600 μm in the case of RPC-00 and 40-100 μm in the case of RPC-50, generally consistent with the large feature sizes of Figure 2.3 and Figure 2.5. The specific surface areas implied by the relaxation experiments are, however, substantially lower than those obtained from preliminary X-ray tomography analyses (Figure 2.15), which yielded 25 and 370 mm^{-1}, respectively, for the RPC-00 and RPC-50 structures. Whereas the tomography result refers to the total surface area, including that from internal pores, catalytic enhancement is possible only from open pores, explaining at least some of the differences in surface areas measured by these two methods. Indeed, a much greater fraction of the pores of RPC-50 are closed compared to those of RPC-00, such that the factor of 15 difference between the two RPCs in tomography-inferred specific surface area is not fully replicated in the kinetic response. Analytical methods for treating tomography data obtained from RPCs with dual-scale porosity, which go beyond the scope of the present work, are described in depth by Ackermann *et al.* [63]

2.5 Conclusions

The results presented here demonstrate several important features of the kinetic response of ceria, a representative nonstoichiometric oxide, to small, stepped perturbation in oxygen partial pressure. First, when the bulk diffusion lengths are small enough that transport through the oxide bulk can be treated as infinitely fast, the conductance relaxation profile will follow an exponential decay curve. This will be true whether the process is limited by surface reaction kinetics or is limited by the supply of sweep gas. Second, the process will be gas-phase limited under conditions of low normalized gas flow rate, high temperature, or high specific surface area of the oxide. Under such conditions, the relaxation time is dependent only on the thermodynamic properties of the oxide and the normalized gas flow rate, with no influence of pore architecture, so long as the pathway of the gas ensures its full interaction with the solid phase. Conversely, the process will be material-kinetic (specifically surface-reaction) limited under conditions of high normalized gas flow rates, low temperature, or low specific surface area. Under these conditions, the relaxation time is dependent only on the surface reaction constant k_{Chem}, and the *accessible* volume-specific surface area, *A/V*. Third, the interplay between these process parameters implies that the transition between material-kinetic and gas-phase limitations will shift to higher temperatures as specific surface area is decreased or normalized gas flow rate is increased.

These results have implications for both fundamental characterization of materials and for design of reactive components for solar-driven thermochemical cycling. For materials characterization, it becomes evident that it is imperative to assess the measurement regime if one is to properly interpret the relaxation time. Typically, one aims to employ a relaxation method for the determination of surface reaction constants. At high temperature, at which both the oxygen non-stoichiometry and the surface reaction constant can be large, the thermo-kinetic response can easily overwhelm the surface reaction response. Peculiar behavior of k_{Chem}, with an apparently decreasing value with increasing temperature, is a feature of measurements in the gas-phase limited regime. The remedy to this situation is simply to increase the gas flow rate until one observes a constant relaxation time. For thermochemical fuel production, typical porous structures have short bulk diffusion lengths such that diffusion limitations do not appear. Furthermore, gas flow rates are low so as to minimize the energy penalty of heating large volumes of gas. At the high tempera-

tures of oxide reduction, this low flow rate can place the material response within the gas-phase limited regime. A deviation between the relaxation expected on the basis of material thermodynamic properties and the observed relaxation behavior can thus be used as a diagnostic for evaluating the accessibility of the solid to the sweep gas.

Supplemental Information of Ch.2

log (1/τ) vs. 1/T behavior for ceria under gas-phase limitation

The reduction enthalpy and entropy of ceria were used to complete the correlation in all range of temperature and pO_2 vs. δ. From the data set of (pO_2, T), [32] the value of $\log\left(-\frac{\partial pO_2(\delta,T)}{\partial\delta}\Big|_{\delta=\delta_f}\right)$ in Eq. (2.16) is calculated at the fixed pO_2 of 8.2×10^{-4} atm. The result is depicted in Figure 2.14.

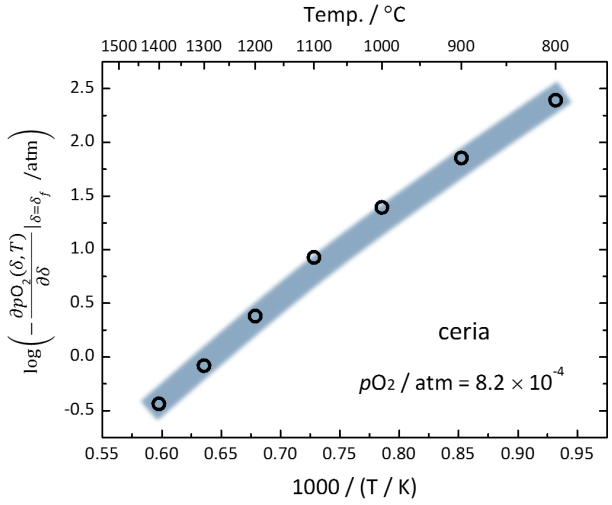

Figure 2.14: $\log\left(-\frac{\partial pO_2(\delta,T)}{\partial\delta}\Big|_{\delta=\delta_f}\right)$ at a pO_2 of 8.2×10^{-4} atm as a function of temperature.

Volume specific surface area measurements

Mercury Intrusion Porosimetry: RPC-00 and RPC-50 samples with a mass of 0.3316 g and 0.4028 g, respectively, were characterized by mercury intrusion porosimeter (Micromeritics Autopore V, USA). The specific surface area values were taken from the cumulative pore area.

X-ray Tomography: RPC-00 and RPC-50 samples were scanned at 2-BM beamline of Advanced Photon Source at Argonne National Laboratory. X-ray beam was filtered with 15-mm Si and 20-mm glass blocks. A sample was rotated in 0 - 180 degree angle range and x-ray projection images were taken at discrete angle position with 0.12 degree/step. The x-ray microscope is composed of a 20μm thick LuAG:Ce scintillator, a 10× mitutoyo long working distance microscope lens, and a pco.edge

camera. Tomographic slice images were reconstructed with Tomopy3, and Avizo® was used for tomographic structure visualization and calculation of area-volume ratio.

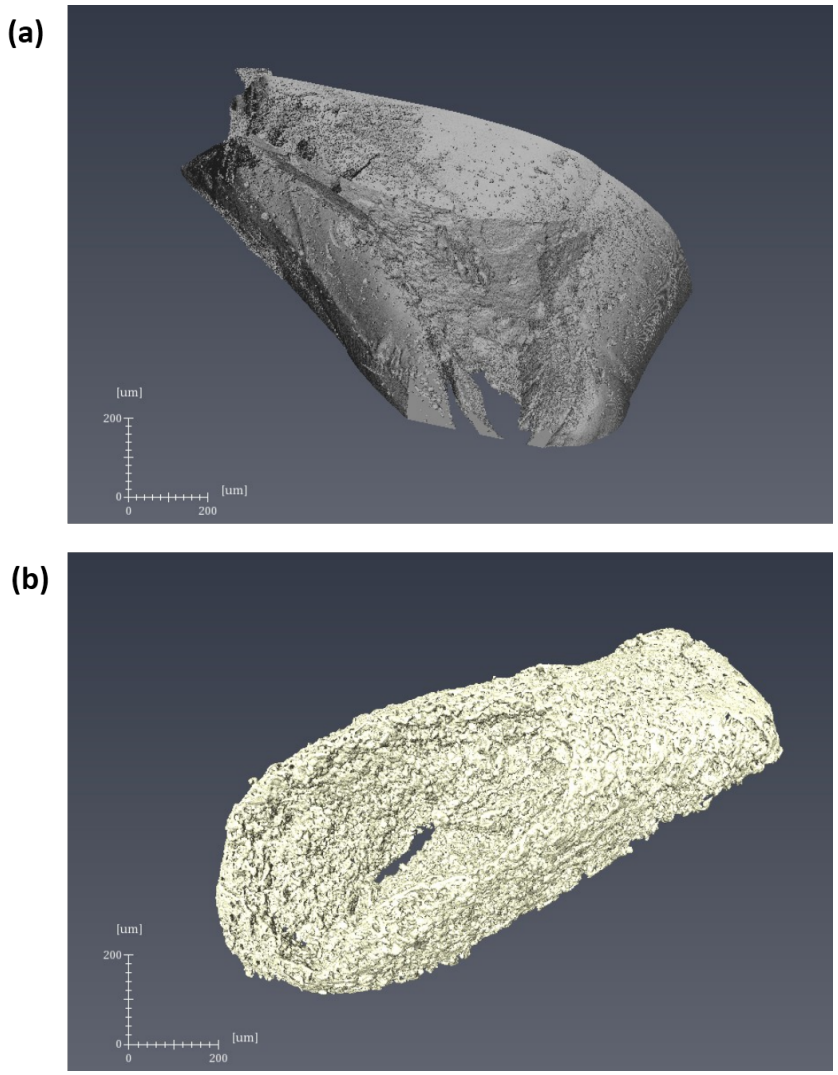

Figure 2.15: Reconstructed 3D images of preliminary X-ray tomography analysis for (a) RPC-00 and (b) RPC-50.

Relaxation profiles and surface reaction constant of dense ceria The surface reaction constant of ceria as measured here is shown in Arrhenius format in Figure 2.16, along with two other results reported in the literature. The single datapoint from reference [53] is derived from an ECR measurement at 1400 °C over a range of pO_2 values. The agreement with the present data is good, which is significant

because the measurement is made using a different sample.

In addition to these k_{Chem} measurements, Kamiya *et al.* reported the value of k^*, obtained from isotope exchange methods, for temperatures from 800 to 1300 °C. [64] As discussed at some length in the literature, k_{Chem} and k^* measure different characteristics of a material, and computing one from the other requires knowledge of the thermodynamic factor ($d \ln a_{\mathrm{O}} / d \ln c_{\mathrm{O}}$, where a_{O} is oxygen activity and c_{O} is oxygen concentration) and electronic transference number. [18] Nevertheless, it is noteworthy that Kamiya *et al.* observed a k^* that monotonically increased with temperature, showing a single slope in the Arrhenius representation [described according to k^* (m/s) = 1.93×10^{-3} exp[-136 (kJ·mol^{-1})/RT]. Somewhat surprisingly, those authors reported that their high purity undoped ceria exhibited extrinsic behavior below about 1000 °C, as manifest in a change in slope in the dependence of $\log(D_{\mathrm{Chem}})$ vs. 1/T, but with no comparable change in slope in the analogous plot for k_{Chem}. It would be reasonable to attribute the change in slope evident in Figure 2.8 of the present work in to a transition between intrinsic and extrinsic behavior given the comparable levels of impurities in the Kamiya and present samples. However, no attempt has been made here to prove or disprove such a hypothesis. Another possible explanation for the change in slope is impurity segregation to the surface-exposed grain boundaries layer. [65–67] It has been reported that such segregation can affect gas-solid reactions [68–70] and may be expected to play a role here as the present conductivity relaxation was performed using polycrystalline ceria with grain size of ~10 μm.

Also shown in Figure 2.16 are a set of three datapoints from Knoblauch *et al.* These authors measured the surface reaction constant by mass relaxation methods (in a conventional thermogravimetric analyzer) from 1300 to 1410 °C. [71] They reported that the surface reaction constant decreases with temperature, in stark contrast to the present results. It is possible that this unusual observation is a result of performing measurements within the thermo-kinetic regime. The normalized gas flow-rate employed by those authors was 93 sccm/g at a $p\mathrm{O}_2$ of 7×10^{-4} atm, and the quoted k_{Chem} at 1400 °C 1.69×10^{-4} cm/s. As implied by Eqs. (2.15)-(2.16), in order to ensure one is operating in the material-kinetic regime, the mass-normalized flow rate must obey $\frac{F}{m_{\mathrm{CeO_2}}} > \frac{k_{\mathrm{Chem}}}{a} \frac{P_{\mathrm{tot}}}{2M_{\mathrm{CeO_2}}} \left(- \frac{\partial p\mathrm{O}_2(\delta)}{\partial \delta} \Big|_{\delta=\delta_{\mathrm{f}}} \right)^{-1}$. For the sample thickness of ~ 1 mm and gas exchange occurring only from one side of the sample, the required flow rate is ~ 400 sccm/g, substantially greater than what the authors employed.

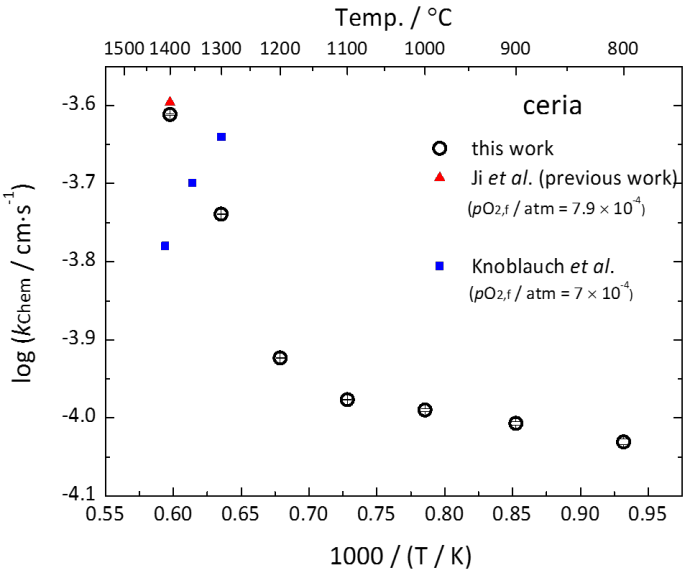

Figure 2.16: The surface reaction rate constant, k_{Chem}, for ceria as a function of temperature at sufficiently high flow rates (763 sccm/g). Shown for comparison is the result reported by Knoblauch *et al.* [71] and from Ji *et al.* [53]

Behavior of time constant in a system maximizing the utilization of sweep gas

Support for the conclusion that insufficient interaction between the solid and gas phases results in a relaxation time in the thermo-kinetic regime that is larger than theoretically expected emerges upon examination of the correlation between the oxygen partial pressure detected at the downstream sensor, Figure 2.6, and the sample conductance. If the gas (upon entering the chamber) and the solid phases are entirely in equilibrium through the relaxation, and the step change in $p\mathrm{O}_2$ is small enough that it induces a proportional change in conductance, [58] then the oxygen partial pressure and conductance should depend on time in an identical manner. Thus, a plot of $G(t)$ vs. $p\mathrm{O}_2(t)$ (a parametric function of time) should yield a straight line extending from the initial to the final values of the two quantities. The same is also true of a plot of the normalized logarithmic values, *i.e.*, $\frac{\log G(t) - \log G_{\mathrm{i}}}{\log G_{\mathrm{f}} - \log G_{\mathrm{i}}}$ vs. $\frac{\log p\mathrm{O}_2(t) - \log p\mathrm{O}_{2,\mathrm{i}}}{\log p\mathrm{O}_{2,\mathrm{f}} - \log p\mathrm{O}_{2,\mathrm{i}}}$, where the initial and final pairs of values are (0,0) and (1,1). This behavior is shown as the red line in Figure 2.17. If, however, the solid does not attain equilibrium with the gas as a consequence of slow surface reaction kinetics, and the gas flow is high enough that the gas composition is unaffected by adsorption or release of oxygen from the solid, then the oxygen partial pressure in the gas phase will immediately attain the final value (equal to the inlet value), whereas the conductance will require

finite time to reach the final state. A plot of the normalized logarithmic values of conductance vs. oxygen partial pressure then follows the path (0,0) → (1,0) → (1,1), shown schematically in the dark blue lines of Figure 2.17. The intermediate case is that in which the gas-phase oxygen partial pressure is, at any given point in time, closer to its final value than the conductance is. This behavior is represented by the dotted curve in Figure 2.17. Such a response can be expected from a gas that does not fully interact with the sample and, as a consequence, does not induce a change in conductance as quickly as the change in gas composition occurs.

Plots of normalized log conductance vs. normalized log pO_2 at 1400 °C are presented in Figure 2.18 for the three porous samples. At low gas flow-rates the porous monolith displays essentially ideal behavior for the gas-limited case, Figure 2.18(a). With an increase in gas flow rate, the behavior deviates slightly from the ideal case, Figure 2.18(b). The RPC-00 sample, Figure 2.18(c), which displays relaxation times furthest from the values implied from the thermodynamic properties of ceria, Figure 2.13, has a profile in the normalized log G vs. normalized log pO_2 plots which deviates most significantly from the idealized red line. The RPC-50 sample, has intermediate behavior both in terms of the measured relaxation times, Figure 2.13, and the correlation between G and pO_2, Figure 2.17(d). Neither of the RPC samples displays the idealized profiles for the limit of material-kinetic controlled response, consistent with the fact that the relaxation has not yet reached the flow rate independent regime, Figure 2.10.

One can also consider the gas-solid interaction likelihood from the perspective of the gas diffusion dynamics. The gas-phase diffusion coefficient of O_2 at 1400 °C in the O_2-Ar mixture employed in this work is approximately 4.5 $cm^2 \cdot s^{-1}$. [72] To provide the gas from the periphery of the reactor sufficient time to come in contact with the ~ 10 mm long sample, the gas velocity should be no greater than 9.1 $cm \cdot s^{-1}$ and hence the flow rate no greater than 76 sccm. The actual gas flow rates utilized in this study, up to 500 sccm, greatly exceeded this value. For measurement of the surface reaction constant, the need to limit the gas velocity to ensure sufficient time for gas-solid interaction conflicts with the requirement that the normalized gas flow rate exceed thermodynamic limit. As shown by the PM sample, these competing requirements can be addressed by creating structures that fill the cross-sectional area of gas flow. Overall, the experimental observations are consistent with the interpretation that the relaxation times are prolonged in the RPC samples because

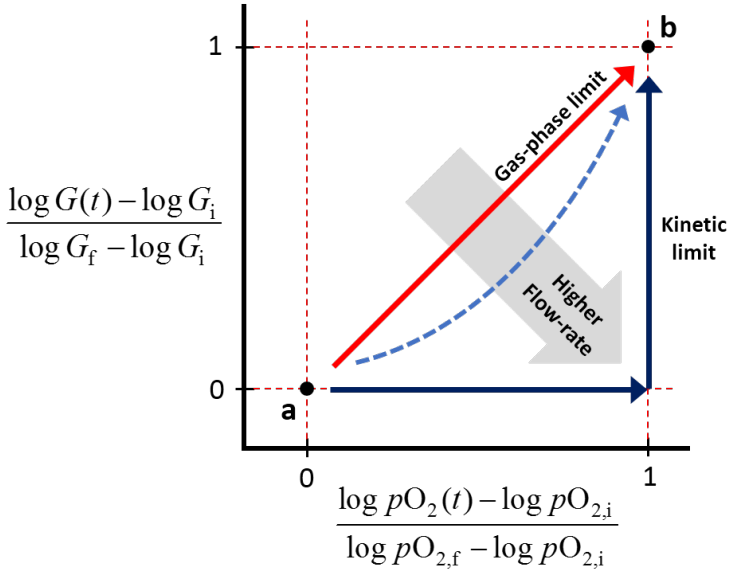

Figure 2.17: Changes of normalized log G vs. normalized log pO_2 with time at which the equilibrium state changes from "a" to "b".

of the poor interaction of the gas phase with the reactive solid, and underscore the importance of optimal design of gas flow patterns and porous material architecture for maximizing catalytic response.

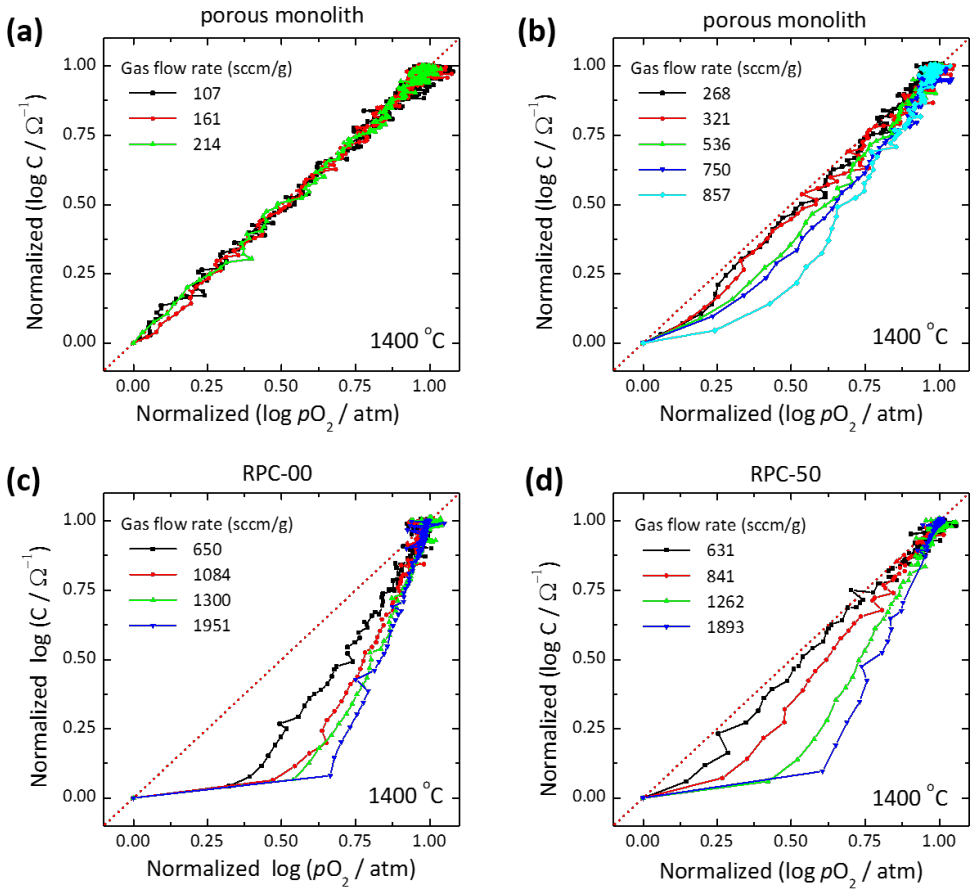

Figure 2.18: Normalized log G vs. normalized log pO_2 graphs at 1400 °C for (a) porous monolith at low gas flow rates (107, 161, 214 sccm/g), (b) porous monolith at high gas flow rates (≥ 268 sccm/g), (c) RPC-00, and (d) RPC-50.

Chapter 3

MATERIAL-KINETIC PROPERTY AT HIGH TEMPERATURE: ELECTRICAL CONDUCTIVITY RELAXATION METHOD

3.1 Introduction

The present study is focused in particular on the kinetics of oxygen uptake/release by ceria, in particular at temperatures relevant to thermochemical fuel production. While the thermodynamic properties of ceria at temperatures as high as 1500 °C and over a wide partial pressure range are known to a high degree of confidence, [32, 58, 73, 74], the same is not true of the kinetic properties. Indeed, only two papers could be found in the literature that attempt to measure diffusivity at temperatures above 1200 °C. [26, 64] In principle, diffusivity can be computed [52] from conductivity and defect concentrations, which are known at high temperature for ceria [32, 58], but the calculation relies on assumptions that may not be entirely valid. Even more striking than the absence of transport measurements is the dearth of studies of surface reaction rates of ceria at temperatures at these high temperatures, with again only two papers on the topic. [64, 71]

Furthermore, in consideration of atmospheric conditions in thermochemical fuel production system, such as H_2O, CO_2, combination of H_2O/CO_2, and particularly in pressure swing mode due to the thermolysis of H_2O/CO_2 at high temperature, H_2O/O_2 or CO_2/O_2, would affect to reaction kinetics, especially to the surface reaction at the solid/gas interface. Therefore, the quantitative knowledge of the material kinetic property itself in the appropriate thermodynamic conditions is essential to compare and sort out the candidate materials and to optimize the structure of the material in the aspect of kinetics. Lane *et al.*[12] reported that the surface reaction is affected by the gas species. Yashiro *et al.*[25] also found that the surface reaction rate constants are not directly related with oxygen partial pressure but depend on the gas species. However, they simply showed that phenomenal behavior without any fundamental suggestions.

Here, we investigate the kinetic property, particularly the surface reaction of ceria at 1400 °C by electrical conductivity relaxation (ECR) method with a combination of

well-defined sample geometries and well-designed reactor configurations for excellent gas control and rapid gas exchanges.[21–23, 27, 53, 75, 76] In particular, based on the exquisitely controlled pH_2O as well as pO_2, we will show how the activities of H_2O and O_2 affect to the surface reaction rate, and will discuss about how the surface reaction of the oxides has to be generally analyzed with respect to atmospheric conditions. This knowledge of the material-kinetic properties at such high temperatures, the flow-rate at the transition between gas-phase and material-kinetic limits (discussed in chapter 2) can be anticipated for the highest efficiency in the thermochemical system.

3.2 Theory

3.2.1 Derivation of equations for relaxation profiles in conductivity

A particularly convenient and well-established technique for measuring material kinetic properties – surface reaction rate, k_{Chem}, and bulk chemical diffusivity, D_{Chem} – is the (isothermal) electrical conductivity relaxation (ECR) method with well-defined geometry sample.[21–23, 27, 75, 76] Here, a small perturbation in gas phase oxygen chemical potential (oxygen partial pressure) causes a material to undergo a small change in oxidation state, which in turn, typically results in a change in conductivity. Under appropriate experimental conditions, the flux across the surface of the oxide is

$$J_{\mathrm{O}} = k_{\mathrm{Chem}} \left(c_{\mathrm{O,eq}} - c_{\mathrm{O,S}} \right) = -D_{\mathrm{Chem}} (\nabla c_{\mathrm{O}})_{\mathrm{S}} \tag{3.1}$$

where $c_{\mathrm{O,eq}}$ is the oxygen concentration of the oxide at equilibrium with the gas phase, and $c_{\mathrm{O,S}}$ is the oxygen concentration just within the oxide surface(s).[57] The associated change in conductivity, σ, with time, t, for a thin, planar sample (in which oxygen incorporation/excorporation occurs only along one dimension) is given by[57, 77–79]

$$\frac{\sigma(t) - \sigma_{\mathrm{i}}}{\sigma_f - \sigma_{\mathrm{i}}} = 1 - \left[\sum_{n=1}^{\infty} \frac{2L^2}{\beta_n^2 \left(\beta_n^2 + L^2 + L \right)} \exp\left(-\frac{\beta_n^2 D_{\mathrm{Chem}} t}{a^2} \right) \right] \tag{3.2}$$

where σ_i and σ_f are the initial and final conductivity values, respectively, and the

sample thickness is $2a$ (with exchange occurring on both surfaces of the thin sample). The $\{\beta_n\}$ are the positive roots of

$$\beta_n \tan \beta_n = \tilde{L}; \quad \tilde{L} = \frac{a k_{\text{Chem}}}{D_{\text{Chem}}} \tag{3.3}$$

and $\tilde{L}$ is a dimensionless length reflecting the relative importance of diffusion and surface reactivity to the overall relaxation rate. The experimental requirements for the validity of this expression include (1) use of a sufficiently small perturbation such that (i) k_{Chem} and D_{Chem} can be treated as constants, that (ii) these properties respond linearly to the perturbation magnitude,[18] that (iii) conductivity varies linearly with oxygen content, and (iv) that the material does not change temperature due to heat release during oxidation or heat adsorption during reduction; (2) use of a sufficiently small reactor volume such that the reactor flush time is much shorter than the material relaxation time; and (3) use of a sufficiently large gas flow rate such that the gas composition surrounding the oxide remains constant over the course of the measurement. When $k_{\text{Chem}} \ll D_{\text{Chem}}/a \quad (\tilde{L} \ll 1)$, the surface reaction dominates the relaxation process, and Eq.(3.2) reduces to

$$\frac{\sigma - \sigma_{\text{i}}}{\sigma_f - \sigma_{\text{i}}} = 1 - \exp\left(-\frac{k_{\text{Chem}}}{a} t\right) = 1 - \exp\left(-\frac{1}{\tau} t\right) \tag{3.4}$$

This simple exponential expression has been widely employed for determining k_{Chem} from the relaxation profiles of thin samples.

3.2.2 Thermodynamic driving force of oxides for H_2O dissociation

Here, we consider the oxygen nonstoichiometric oxide which has (oxygen) ionic and electronic charge carriers in the bulk oxide. The thermodynamic feasibility of the oxide towards oxidation by dissociating H_2O is readily assessed through the consideration of ΔG of oxidation reaction of the oxide in comparison to ΔG° for hydrogen oxidation reaction, at standard state.[8] The hydrogen oxidation reaction and its ΔG° are expressed as

$$H_2(g) + \frac{1}{2} O_2(g) \rightarrow H_2O(g) \tag{3.5}$$

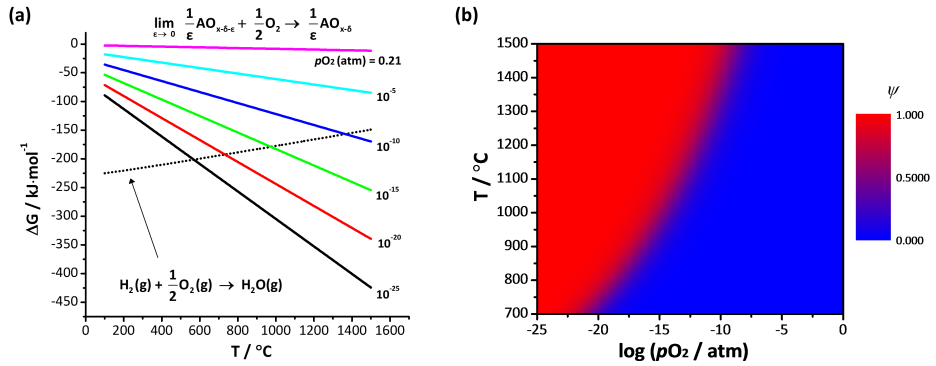

Figure 3.1: (a) Gibbs free energy of the gas-phase hydrogen oxidation reaction in standard state (black dotted line) and that of oxidation of the oxides with respect to pO_2 (colored solid lines), and (b) reaction extent of H_2O dissociation reaction driven by the oxides as a function of T and pO_2.

$$\Delta G^{o}_{H_2O}(T) = -RT \ln K_{H_2O} = -RT \ln \left(\frac{pH_2O}{pH_2 \cdot {pO_2}^{1/2}} \right) \tag{3.6}$$

and the value of $\Delta G^{o}_{H_2O}(T)$ is known in a wide range of temperature.[31] For the nonstoichiometric oxide, the oxidation reaction with an infinitesimal change in nonstoichiometry (ε) and its ΔG on a per mole atomic oxygen basis are expressed as

$$\lim_{\varepsilon\to 0} \frac{1}{\varepsilon}AO_{x-\delta-\varepsilon} + \frac{1}{2}O_2(g) \rightarrow \frac{1}{\varepsilon}AO_{x-\delta} \tag{3.7}$$

$$\Delta G_{oxide}(T, \delta) = -RT \ln({pO_2}^{-1/2}) \tag{3.8}$$

It implies that if the nonstoichiometric oxides, whatever the material is, are in the equilibrium state at the fixed T and pO_2, ΔG_{oxide} for every oxide is determined as a peculiar value by Eq. (3.8) regardless of the value of δ. The ΔG values for the oxidation of hydrogen and nonstoichiometric oxide as a function of T and ΔG_{oxide} (Figure 3.1(a)) indicate that the thermodynamic power of the oxide towards oxidation by dissociating H_2O increases as increasing T and/or decreasing pO_2. From the difference between ΔG_{oxide} and $\Delta G^{o}_{H_2O}$, the reaction extent of steam to hydrogen conversion driven by the oxidation of the oxide, ψ, can be thermodynamically calculated.[55] Combining Eq. (3.5) and (3.7) gives the expression of the oxidation

reaction for the oxide from H_2O, and therefore ψ is expressed only as a function of T and pO_2:

$$\lim_{\varepsilon \to 0} \frac{1}{\varepsilon} AO_{x-\delta-\varepsilon} + H_2O(g) \rightarrow \frac{1}{\varepsilon} AO_{x-\delta} + H_2(g) \tag{3.9}$$

$$\Delta G_{oxide}(T, \delta) - \Delta G^{o}_{H_2O}(T) = -RT \ln \left(\frac{pH_2}{pH_2O} \right) = -RT \ln \left(\frac{\psi}{1-\psi} \right) \tag{3.10}$$

From Eq. (3.10), the behavior of ψ is presented in the contour plot in Figure 3.1(b) with respect to T and pO_2. It is apparent that the oxide has higher thermodynamic power to dissociate H_2O where ψ approaches 1 (the red regime appeared at higher temperature and/or lower pO_2). For example, the oxide has ψ of 2.06×10^{-8} at 800 °C in log (pO_2 / atm) of -3, whereas ψ of 4.66×10^{-4} at 1400 °C in the same pO_2, indicating that H_2O is more favorable to play as the oxidizing agent at higher high temperature.

3.2.3 Surface reaction rate of oxidation in O_2/H_2O atmosphere

The oxygen nonstoichiometry of the oxide is a material property which is a predetermined property only by temperature and pO_2. Thus, perturbation in pO_2 of surrounding gas toward the higher drives the oxide to undergo a change in oxidation state to a new equilibrium state, Eq. (3.11). If the reduced oxide is exposed to higher pO_2 containing non-negligible humidity ($pH_2O > \sim 0$) in relatively high temperature and low pO_2 regime at which the oxide has high thermodynamic driving force to be oxidized by dissociating H_2O, an another independent pathway for the oxidation exists, Eq. (3.12).

$$\frac{1}{2} O_2(g) + 2Ce'_{Ce} + V^{\bullet\bullet}_{O} \rightarrow O^{\times}_{O} + 2Ce^{\times}_{Ce} \tag{3.11}$$

$$H_2O(g) + 2Ce'_{Ce} + V^{\bullet\bullet}_{O} \rightarrow H_2(g) + O^{\times}_{O} + 2Ce^{\times}_{Ce} \tag{3.12}$$

The chemical redox reaction of the oxides, in principle, is typically considered as consisting of a surface reaction at a gas/solid interface (k_{Chem}) and a chemical

diffusion inside the oxide (D_{Chem}). The dominance of each step in overall reaction is determined from a relative magnitude of a diffusion length of the oxide and a characteristic length defined by $D_{\mathrm{Chem}}/k_{\mathrm{Chem}}$. If in a condition of diffusion length $\gg$ characteristic length, the chemical diffusion in the oxide governs equilibration kinetics toward new equilibrium oxygen nonstoichiometry, and the surface reaction does in an opposite condition. For the former, it is obvious that the kinetics of chemical diffusion is not affected by the reaction pathway differentiated by the species of oxidants, because i) the chemical diffusion is only dependent of the interplay of ionic and electronic charge carriers in the oxide, and ii) the amount of incorporated neutral oxygen at the very surface layer of the oxide is always sufficient due to the much faster surface reaction in this case. Therefore, the oxidation kinetics is always identical whether the oxygen is sourced only from O_2 (Eq. (3.11)), or from both of O_2 and H_2O (Eq. (3.11) and (3.12) together) if the final pO_2 is identical. For the latter, conversely, the existence of H_2O (more accurately, the activity of oxidants in gas) has impact on the surface reaction, because the surface reaction is a result of the interplay of defect-chemical charge carriers in the oxide as well as the species of oxidants/reductants in atmosphere. For example, if the supplying gas consists of H_2O and O_2 at high temperature as depicted in Figure 3.2(a), possibly due to the thermolysis of H_2O, the oxidation in the surface reaction limited regime will be controlled by the activities of H_2O and O_2, simultaneously.

Only for the case in which the oxidation reaction of the oxide is limited by the surface reaction rate due to the much faster chemical diffusion through the oxide, the impact of H_2O on k_{Chem} can be readily unveiled by analyzing the relaxation behavior of oxygen concentration toward new equilibrium state under small perturbation in pO_2. In the humidified atmosphere, the total oxygen flux across the surface of the oxide ($J_{\mathrm{O,tot}}$) can be considered as a simple summation of two different oxygen fluxes sourced from O_2 ($J_{\mathrm{O,O_2}}$) and H_2O ($J_{\mathrm{O,H_2O}}$) under an assumption that the two fluxes are independent each other as shown in Figure 3.2(b). If the small perturbation in pO_2 drives small oxygen concentration change in the oxide, then both oxygen fluxes through the interface of solid/gas, $J_{\mathrm{O,O_2}}$ and $J_{\mathrm{O,H_2O}}$, can be assumed as first order reaction with respect to oxygen concentration. This statement results in an expression of oxygen flux correlated with k_{Chem} as below:[52]

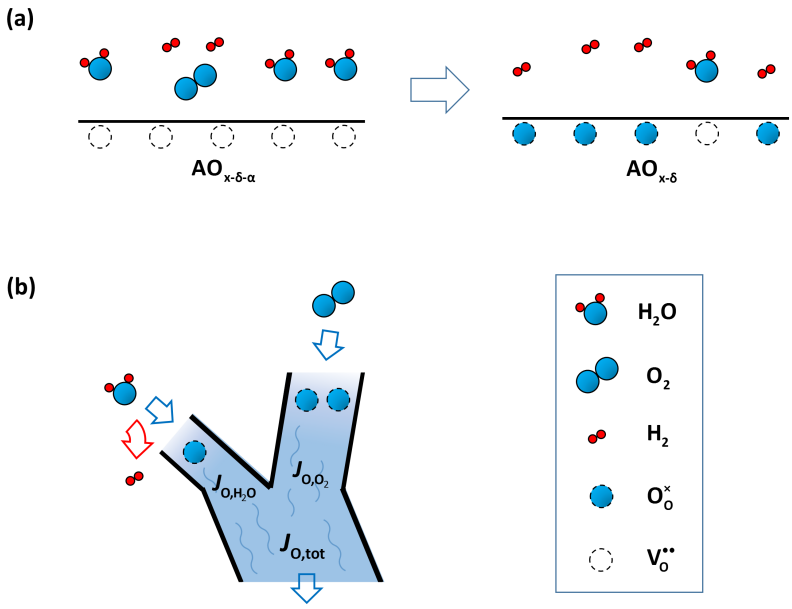

Figure 3.2: Schematics of (a) oxygen incorporation at the gas/solid interface and (b) total oxygen flux at high temperature in O2/H2O atmosphere.

$$\begin{aligned} J_{\mathrm{O,tot}} &= J_{\mathrm{O,O_2}} + J_{\mathrm{O,H_2O}} \\ &= k_{\mathrm{Chem,O_2}}(c_{\mathrm{O,eq}} - c_{\mathrm{O,surf}}) \;+\; k_{\mathrm{Chem,H_2O}}(c_{\mathrm{O,eq}} - c_{\mathrm{O,surf}}) \\ &= (k_{\mathrm{Chem,O_2}} + \; k_{\mathrm{Chem,H_2O}})\,(c_{\mathrm{O,eq}} - c_{\mathrm{O,surf}}) \\ &= k_{\mathrm{Chem,tot}}(c_{\mathrm{O,eq}} - c_{\mathrm{O,surf}}) \end{aligned} \tag{3.13}$$

where $c_{\mathrm{O,eq}}$ is the oxygen concentration of the oxide at equilibrium with the gas phase, $c_{\mathrm{O,surf}}$ is the oxygen concentration just within the oxide surface, $k_{\mathrm{Chem,O_2}}$ and $k_{\mathrm{Chem,H_2O}}$ are respectively the surface reaction rate constant relevant to O_2 and H_2O, and $k_{\mathrm{Chem,tot}}$ is the simple sum of $k_{\mathrm{Chem,O_2}}$ and $k_{\mathrm{Chem,H_2O}}$. By applying a continuity relation relevant to the oxygen concentration and the oxygen flux, and by solving the differential equation with respect to the time dependent oxygen concentration ($c_{\mathrm{O,surf}}$), the normalized oxygen concentration follows a simple exponential form. Since the sufficiently small driving force for the oxidation is considered here, *i.e.* small perturbation in $p\mathrm{O_2}$, the total electrical conductivity of the oxide (σ) is proportional to the oxygen concentration, and thus normalized conductivity also has the identical functional form as given

$$\frac{c - c_i}{c_f - c_i} = \frac{\sigma - \sigma_i}{\sigma_f - \sigma_i} = 1 - \exp\left(-\frac{k_{\mathrm{Chem,tot}}}{a}t\right) = 1 - \exp\left(-\frac{k_{\mathrm{Chem,O_2}} + k_{\mathrm{Chem,H_2O}}}{a}t\right) \tag{3.14}$$

where subscripts i and f signify initial and final states, respectively. This derivation implies that the conductivity relaxation at which the surface reaction governs overall reaction will follow the simple exponential decay behavior embedding $k_{\mathrm{Chem,tot}}$ ($= k_{\mathrm{Chem,O_2}} + k_{\mathrm{Chem,H_2O}}$) in the humidified conditions. Under the condition without humidity, $k_{\mathrm{Chem,tot}}$ should be $k_{\mathrm{Chem,O_2}}$, therefore, one can easily separate $k_{\mathrm{Chem,H_2O}}$ from $k_{\mathrm{Chem,tot}}$ by calculating $k_{\mathrm{Chem,tot}} - k_{\mathrm{Chem,O_2}}$ under the physically reasonable assumption that $k_{\mathrm{Chem,O_2}}$ is independent of $p\mathrm{H_2O}$ and $k_{\mathrm{Chem,H_2O}}$ is independent of $p\mathrm{O_2}$. The experimental results for separating $k_{\mathrm{Chem,H_2O}}$ and $k_{\mathrm{Chem,O_2}}$ will be shown below.

3.3 Experimentals

High temperature ECR studies were performed on undoped, polycrystalline ceria using a free-standing thin-sample geometry. Commercial undoped ceria powder (Inframat Advanced Materials, USA) was compacted into a parallelepiped by uni-axial die-pressing at 100 MPa, followed by cold isostatic pressing at 300 MPa. The green body was sintered at 1500 °C for 10 h, and a compact with density > 95% of theoretical was obtained. The sample, 0.3825 g in mass, 0.56 mm in thickness, 5.48 mm in width and ~19 mm in length, was polished down to 3 μm roughness. In a previous analysis of the conditions of applicability of the 1-D solution to the composition profile (embodied in Eqs. (3.2) and (3.4)), we found that the 1-D model is valid for rectangular-shaped samples so long as the edge thickness is less than ~20% of next largest dimension.[21] Here, the thickness is only 10% of the sample width, justifying the analysis according to the 1-D model. Conductivity was measured using DC methods in a four-probe configuration. Contact was made by tightly wrapping Pt wires around notches made at the far ends of the sample. Gas and temperature control were provided by an in-house constructed ECR reactor with a sample chamber of approximately 23 cm^3 in volume. The sample was placed lengthwise within the 1 cm diameter chamber. The oxygen partial pressure and temperature were measured *in situ* using a zirconia based oxygen sensor ($SIRO_2$

C700+, Ceramic Oxide Fabricators, Australia) placed approximately 2 cm from the sample. The relaxation behavior was characterized at 1400 °C (recorded sample temperature) in the range of -4.3 ≤ log (pO_2 / atm) ≤ -2.0, achieved by flowing mixtures of dry O_2 and Ar. Two sets of exploratory experiments were first performed. In the first set, the impact of sweep gas flow rate on both the steady state pO_2 and the relaxation time was examined. In the second set of exploratory experiments, the impact of the magnitude of the step change in pO_2 was examined at flow rates high enough to ensure material-kinetic limited behavior.[80] With the conditions for obtaining reliable material kinetic parameters and specifically k_{Chem} values determined ($\Delta \log(pO_2/\mathrm{atm}) \leq 0.13$ and $F \geq 523$ sccm/g), relaxation profiles were measured over the entire pO_2 range of interest and the dependence of k_{Chem} on pO_2 evaluated. Absence of solid-state diffusion contributions (from all experiments) was established by analyzing the relaxation profiles according to Eq.(3.2) using an in-house written Matlab code.[21] The maximum value of that was encountered was ~0.26, implying that $D_{\mathrm{Chem}} \gg a^2/\tau$ ($i.e.$, $\gg k_{\mathrm{Chem}}^{\mathrm{apparent}} \cdot a$) and thus that bulk diffusion contributes negligibly to the relaxation kinetics. Moreover, fits utilizing Eq.(3.2) and those utilizing the simple exponential form of Eq.(3.4) yielded statistically identical values of τ (and thus of $k_{\mathrm{Chem}}^{\mathrm{apparent}}$), providing further evidence of negligible solid-state diffusion effects.[21]

For ECR measurements under humidified conditions, another sample was prepared using undoped ceria powder (Aldrich, 211575, 99.9% purity) followed by identical pressing and sintering processes. The relative density exceeded 96% of the theoretical density, and the sintered sample was cut by low speed diamond saw (Buehler, Isomet Low speed saw, US) to a parallelepiped and polished down to 3 μm. The final dimension of the sample was 0.79 (thickness) × 4.71 (width) × ~16.3 (length) mm^3, and the mass was 0.393 g. Scanning electron microscopy image (Hitachi S4800-II cFEG SEMinstrument), Figure 3.17, reveals that the material was fully dense with the grain size of 8.9 ± 1.8 μm.

In ECR measurements, the re-equilibrations of the conductivity were driven by the small perturbation in only pO_2 (ΔpO_2) or in both pO_2 (ΔpO_2) and pH_2O (ΔpH2O) as specified in Figure 3.3. The pH_2O was measured by an ex-situ humidity sensor (Hygroclip IM-1, Rotronic Instruments, UK) attached at the outlet of the chamber. The desired pO_2 was obtained by employing gas mixture of Ar/O_2 at the total flow rate of 300 sccm. The pH_2O was controlled by passing the mixture of Ar/O_2 through an oven-heated water bath held at specific temperatures. To avoid the condensation of water, gas lines from the water bath to the ends of the line, including humidity

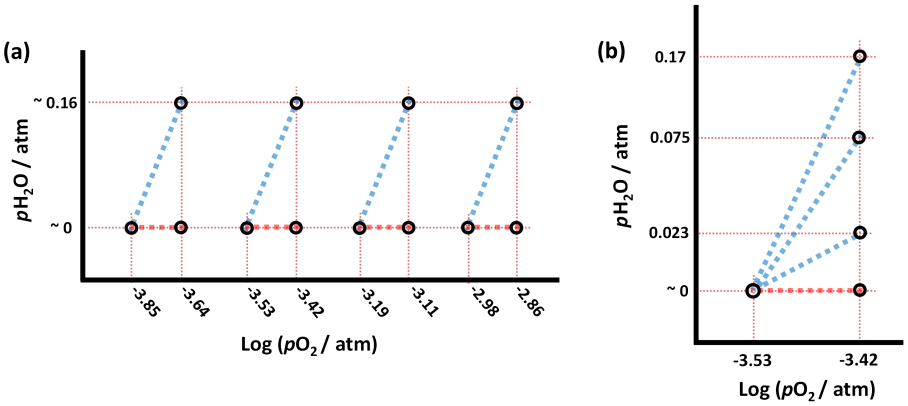

Figure 3.3: The detail of experimental pO_2 and pH_2O conditions at 1400 °C: The small perturbation in only pO_2 (ΔpO_2) or in both of pO_2 (ΔpO_2) and pH_2O (ΔpH_2O).

sensor were heated to ~90 °C. To obtain the almost identical pO_2 in different humidified conditions, *i.e.* different pH_2Os, the mixing ratio of Ar and O_2 was elaborately controlled based on the promptly measured pO_2. The pH_2Os denoted in Figure 3.3 are the values at 1400 °C converted from the measured pH_2Os around 90 °C. The detail is shown in Supplemental Information.

3.4 Results and Discussion

3.4.1 Materials evaluation

A key requirement for successful ECR experiments is that the material conductivity vary with oxygen partial pressure. As summarized in Figure 3.4, the conductivity of ceria indeed shows a clear dependence on oxygen partial pressure (where the latter is that recorded by the oxygen sensor). The present results are consistent with earlier work of Blumenthal *et al.*[81], and the observed power law exponent of -0.179 ± 0.001 approximately obeys the $pO_2^{-1/6}$ dependence suggested from the defect-chemical analysis reported by Tuller,[58] in which it is demonstrated that the dominant defect species are oxygen vacancies and free electrons. The sensitivity of the (n-type) conductivity to pO_2 enables the use of relatively small step changes in oxygen partial pressure for the ECR measurements. In particular, for a step change in $\log(pO_2/\text{atm})$ of 0.068, a typical value utilized in this work, the conductivity changes by about 2.8 %, which is easily detected. In addition, the conductivity was

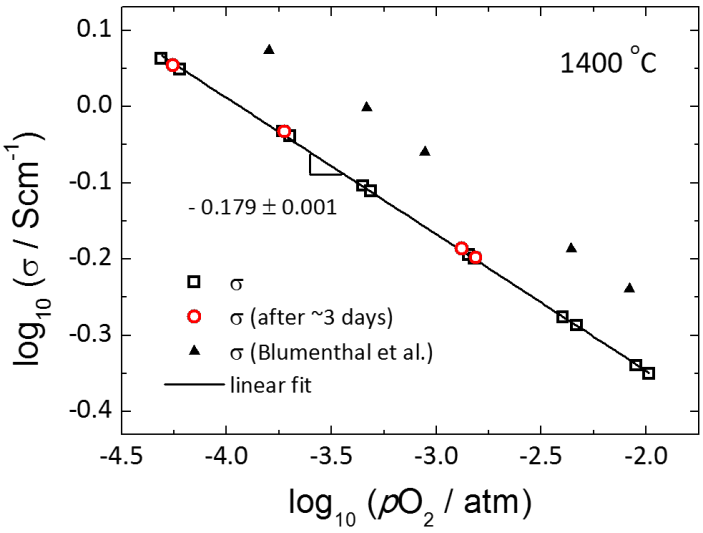

Figure 3.4: Total electrical conductivity of ceria as a function of pO_2 at 1400 °C. Red open circle is the conductivity measured after ~3 days, black line shows the best linear fit, and black filled triangle is from the work of Blumenthal et al. [81] for comparison.

invariant over a measurement period of 3 days, indicating excellent stability of both the sample and the electrodes, despite the very high temperature (1400 °C).

3.4.2 Influence of the magnitude of the pO_2 perturbation

Conductivity relaxation profiles obtained for both oxidizing and reducing directions are presented in Figure 3.5 (gas flow rate of 784 sccm/g) for two experimental conditions with similar mean oxygen partial pressures of (a) 6.7×10^{-5} atm and (b) 6.0×10^{-5} atm, but different values of $|\Delta\log(pO_2)|$: (a) 0.19 and (b) 0.13. At this very high gas flow rate, gas-phase limitations are overcome. The profiles reveal significant difference between oxidation and reduction directions in the case of the larger perturbation. In contrast, the pair of profiles obtained under the smaller perturbation are very similar. The extracted k_{Chem} values for the small perturbation experiment are $(2.404 \pm 0.003) \times 10^{-5}$ cm/s for oxidation ($k^{\mathrm{ox}}_{\mathrm{Chem}}$) and $(2.278 \pm 0.006) \times 10^{-5}$ for reduction ($k^{\mathrm{red}}_{\mathrm{Chem}}$), within 5% of one another, with reduced R^2 values >0.999. The large perturbation experiment yielded profiles that surprisingly

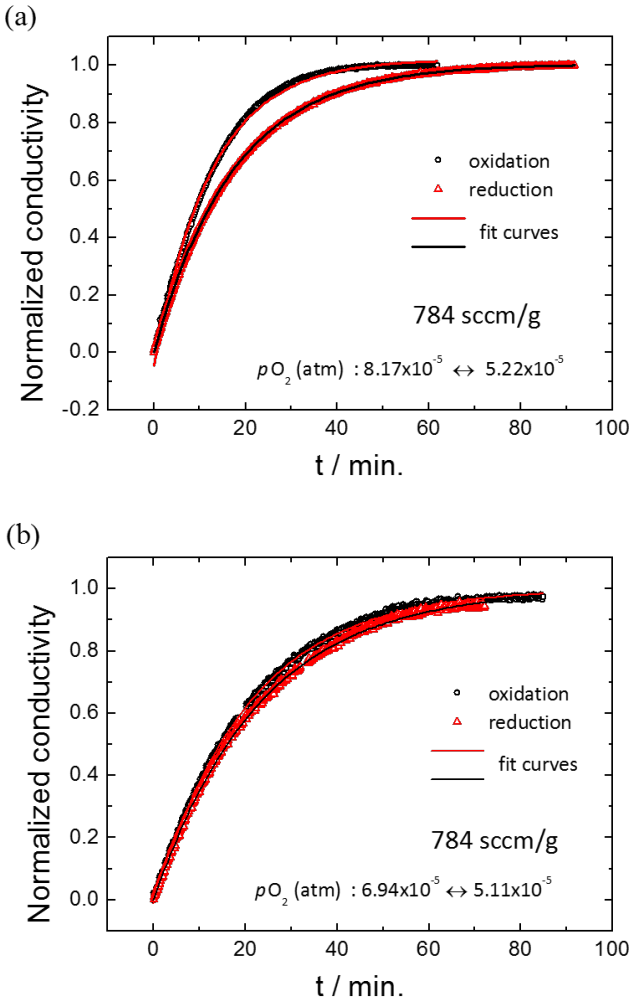

Figure 3.5: Conductivity relaxation profiles upon oxidation and reduction under (a) relatively large pO_2 change ($8.17 \times 10^{-5} \leftrightarrow 5.22 \times 10^{-5}$ atm), showing inequivalence of the forward and reverse profiles and thus application of too large of a step change, and (b) small pO_2 change ($6.94 \times 10^{-5} \leftrightarrow 5.11 \times 10^{-5}$ atm), showing almost identical forward and reverse profiles and thus application of a sufficiently small step change. Solid lines are the best fits to Eq. (3.3); all measurements are performed at 1400 °C and with sufficiently high flow rate (784 sccm/g) to avoid gas-phase limitations.

were also well-described by the exponential form of Eq. (3.4). The two surface reaction rate constants extracted are $k^{ox}_{Chem} = (3.725 \pm 0.021) \times 10^{-5}$ cm/s ($R^2 = 0.998$) and $k^{red}_{Chem} = (2.690 \pm 0.002) \times 10^{-5}$ cm/s ($R^2 = 0.999$), which differ by 38%.

A substantial difference between the rate constants derived in the two directions (as encountered for the large perturbation measurements) immediately implies that the system is no longer in the simple linear regime. Nevertheless, the profiles, as

noted, are well fit by a single exponential expression, a result that others have also observed when the step change is not excessively large.[80, 82] Asymmetry between $k_{\mathrm{Chem}}^{\mathrm{ox}}$ and $k_{\mathrm{Chem}}^{\mathrm{red}}$ under large step changes $p\mathrm{O}_2$ has been reported previously, but with significant inconsistencies. Wang *et al.*[80] found $k_{\mathrm{Chem}}^{\mathrm{ox}} > k_{\mathrm{Chem}}^{\mathrm{red}}$ and further reported that the rate constant was largely determined by the value of the final oxygen partial pressure. For a k_{Chem} that increases with increasing oxygen partial pressure, dependence solely on the final $p\mathrm{O}_2$ automatically implies their result of $k_{\mathrm{Chem}}^{\mathrm{ox}} > k_{\mathrm{Chem}}^{\mathrm{red}}$. The relative values determined here may also be due to the same combination of factors (measured k_{Chem} depends on final $p\mathrm{O}_2$, and true k_{Chem} increases with increasing $p\mathrm{O}_2$). On the other hand, Merkle and Maier report that k_{Chem} depends on both initial and final oxygen partial pressures during oxidation, and solely on the initial $p\mathrm{O}_2$ in the reduction direction (a result supported theoretically), and hence no generalization is possible with respect to the relative magnitudes of $k_{\mathrm{Chem}}^{\mathrm{ox}}$ and $k_{\mathrm{Chem}}^{\mathrm{red}}$.[82] In contrast, Lohne *et al.* predict $k_{\mathrm{Chem}}^{\mathrm{ox}} > k_{\mathrm{Chem}}^{\mathrm{red}}$ when gas stagnation effects become important.[76] Most significant for the present study is that it is possible to apply perturbations that are small enough to ensure almost equal values between $k_{\mathrm{Chem}}^{\mathrm{ox}}$ and $k_{\mathrm{Chem}}^{\mathrm{red}}$, and hence that the system remains essentially in the linear regime. For the subsequent measurement of k_{Chem} as a function of oxygen partial pressure, appropriately small step changes were applied.

3.4.3 Surface reaction rate constant in dry conditions

The dependence of k_{Chem} on $p\mathrm{O}_2$ over the range $-4.3 \leq \log(p\mathrm{O}_2 \text{ / atm}) \leq -2.0$ is summarized in Figure 3.6, for measurements performed using gas flow rates of either 784 or 1046 sccm/g and $\Delta\log(p\mathrm{O}_2/\mathrm{atm})$ values of less than 0.13. The oxygen vacancy content, as reported by Panlener *et al.*[32] is also shown in the figure for comparison. As with all the other relaxation profiles measured in this work, those measured in the construction of Figure 3.6 were well described by a simple exponential form. The reduced R^2 values were in all cases > 0.997 and the (error of k_{Chem})/ k_{Chem} was < 1.7%. The error bar reported in the figure for k_{Chem} reflects the difference between the values measured in the oxidation and reduction directions, whereas as that reported for $p\mathrm{O}_2$ reflects the perturbation range. The equivalence of the results at 784 and at 1046 sccm/g demonstrates that across the entire $p\mathrm{O}_2$ regime of measurement, the relaxation behavior was free of gas-phase limitations.

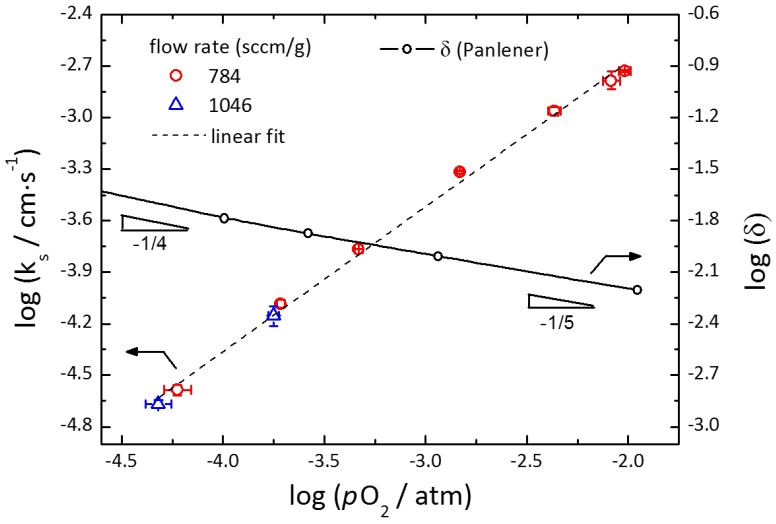

Figure 3.6: The surface reaction rate constant, k_{Chem}, for the oxidation/reduction of undoped ceria as a function of $p\mathrm{O}_2$ at sufficiently high flow rates (784 and 1046 sccm/g) at 1400 °C. Shown for comparison is also the oxygen non-stoichiometry, δ, as reported by Panlener *et al.*,[32] on a comparable log scale. The vacancy concentration is given by δ, whereas the electron concentration is given by 2δ.

All values of k_{Chem} in Figure. 3.6 lie on a single straight line expressed as

$$\log\left(k_{\mathrm{Chem}}/\mathrm{cm}\cdot\mathrm{s}^{-1}\right) = (0.84 \pm 0.02) \times \log\left(p\mathrm{O}_2/\mathrm{atm}\right) - (0.99 \pm 0.05) \qquad (3.15)$$

The power dependence observed here (with a power law exponent m of 0.84 ± 0.02) is unusual in its magnitude, lying at the extreme upper end of the range of values reported for other mixed ion and electron conductors.[83] It is also unusual in that it reflects the properties of an n-type material catalyzing the reaction between gaseous O_2 and oxygen ions in the solid state. Globally, this can be expressed in Kroger-Vink notation[83–85] as

$$\mathrm{O}_2(g) + 2\mathrm{V}_{\mathrm{O}}^{\bullet\bullet} + 4e' \rightleftharpoons 2\mathrm{O}_{\mathrm{O}}^{\times} \qquad (3.16)$$

In the much more commonly examined p-type materials used in the cathodes of solid oxide fuel cells, the reaction is typically expressed as

$$\mathrm{O}_2(g) + 2\mathrm{V}_{\mathrm{O}}^{\bullet\bullet} \rightleftharpoons 2\mathrm{O}_{\mathrm{O}}^{\times} + 4\mathrm{h}^{\bullet} \qquad (3.17)$$

reflecting the greater abundance of holes ($h^{\bullet}$) than free electrons. In those materials, a positive m (reported values range from 0.14 to 0.82) coincides with an increase in the concentration of the dominant electronic defects with increasing oxygen partial pressure.[21] It has been suggested that $m \cong 3/4$ (for a system with hole concentration that depends on oxygen partial pressure according to a 1/4 power law exponent, and with a low adsorbate coverage as is typical of high temperatures) occurs when reduction of diatomic oxygen from the superoxo to the peroxo species is the rate-limiting step, specifically[86]

$$O_{2,ad}^{-} \rightarrow O_{2,ad}^{2-} + h^{+} \tag{3.18}$$

Although the discussion is nominally based on an evaluation of p-type conductors, this result is, in principle, independent of the nature of the dominant electronic species. Moreover, such a reaction can be rate-limiting even when monoatomic oxygen ions (O_{ad}^{-}), entropically favored at high temperatures, are the predominant adsorbate species. Whether this interpretation can be applied to the behavior of high-temperature, undoped ceria, in which the dominant electronic defects are electrons and the pO_2 power law exponent describing the concentration of the minority hole species is ~0.18, remains uncertain. Not only is the defect chemistry substantially different, but also the extent of the experimental data is somewhat limited to support a detailed mechanistic model.

3.4.4 Surface reaction rate constant in humidified conditions

The relaxation profiles in electrical conductivity are presented in Figure 3.7 and Figure 3.8. To confirm that the experiments were performed in the material-kinetic limit, not in the gas-phase limit due to insufficient supply of sweep gas considered as oxidants/reductants, the effect of gas flow rates on the relaxation profiles was examined in the humidified and dry atmospheric conditions, respectively (Figure 3.18). The relaxation behavior was independent of the flow rate, therefore it verifies that the overall reactions were limited by the material-kinetics, and the gas supply of 300 sccm was sufficient to avoid gas-phase limitation in this study.

All of the relaxation profiles are well described by the exponential decay expression in Eq. (3.12) with reduced $R^2 > 0.997$ and (error of k_{Chem})/$k_{Chem} < 1.1$ %, which

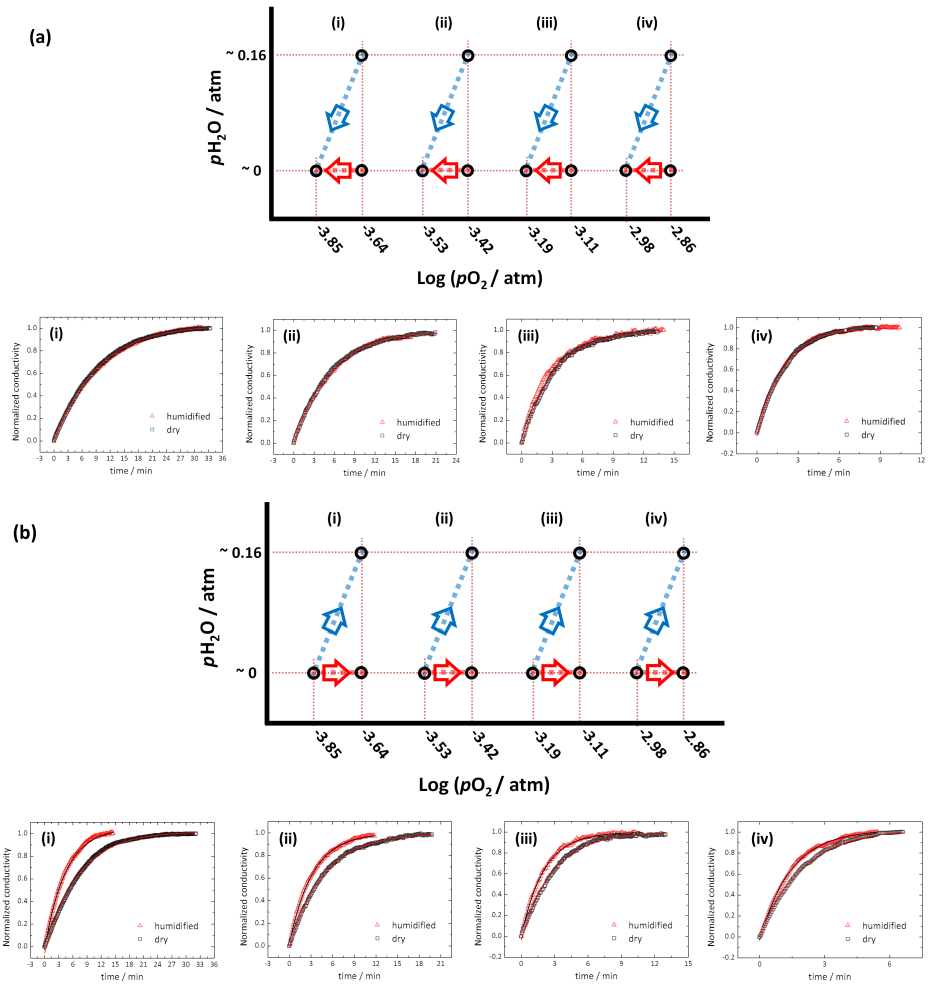

Figure 3.7: Normalized conductivity relaxation profiles along (a) reduction to the identical condition, and (b) oxidation to different $p\mathrm{H_2O}$ but same $p\mathrm{O_2}$ conditions. The detail of $p\mathrm{O_2}$ and $p\mathrm{H_2O}$ values is specified as denoted in the graph at the top of each. Solid lines in the relaxation profiles are the best fits to Eq. (3.14).

means that the redox reaction is limited only by the surface reaction. The values of k_{Chem} at $p\mathrm{H_2O}$ = ~0, *i.e.* $k_{\mathrm{Chem,O_2}}$, show good agreement with the value obtained from previous dense sample for dry conditions. (Figure 3.19), and those lie on a single straight line expressed as:

$$k_{\mathrm{Chem,O_2}}/cm \cdot s^{-1} = 10^{-(1.14\pm0.04)} \cdot (p\mathrm{O_2}/atm)^{0.79\pm0.01} \tag{3.19}$$

For the reduction reaction, as Wang *et al.* and Merkle *et al.* pointed out that the reaction rate is largely determined by the value of the final gas atmosphere,[80, 82] the relaxation profiles in the identical final $p\mathrm{O_2}$ and $p\mathrm{H_2O}$ conditions show

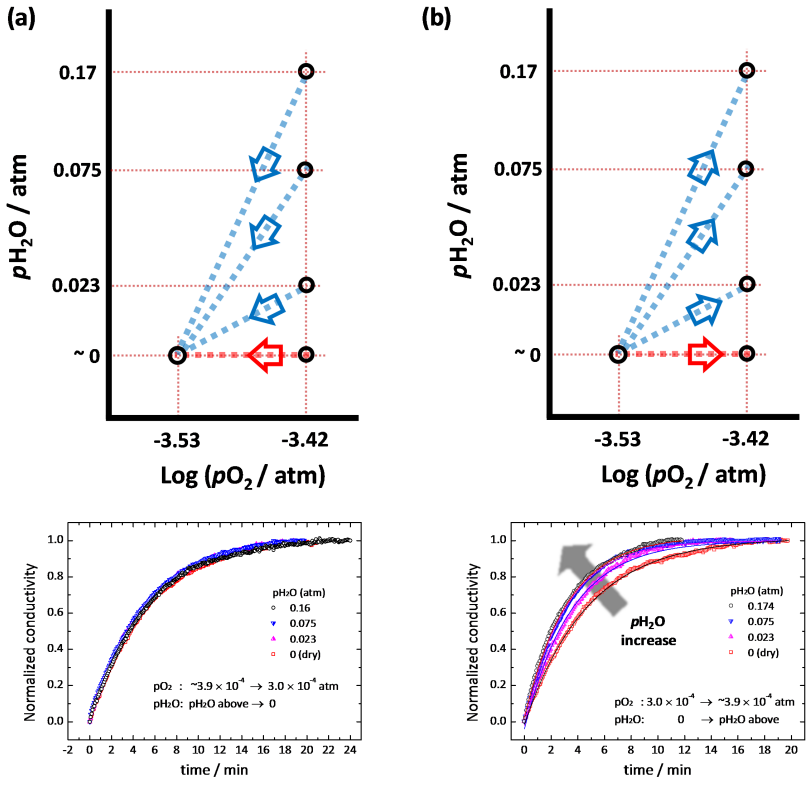

Figure 3.8: Normalized conductivity relaxation profiles along (a) reduction to the identical condition, and (b) oxidation to the different pH_2O conditions. Solid lines in the relaxation profiles are the best fits to Eq. (3.14).

the same profiles regardless of initial pO_2 and pH_2O as presented in Figure 3.7(a) and Figure 3.8(a). For the oxidation reaction as shown in Figure 3.7(b), there is a clear increase in the relaxation rate in the humidified condition compared to the rate in the dry condition, and the magnitude of enhancement in the rate becomes smaller as pO_2 approaches to the higher at fixed pH_2O (~ 0.16 atm). Furthermore, Figure 3.8(b) shows that the relaxation rate is enhanced as pH_2O increases from ~0 to 0.17 atm at fixed pO_2 ($10^{-3.42}$ atm). This behavior is clearly seen in Figure 3.9, showing the $k_{Chem,tot}$ values which are extracted from the relaxation profiles in the oxidation reaction. As discussed in the part of theory, the assumption of $k_{Chem,H_2O}=f(pH_2O) \neq f(pO_2)$ and $k_{Chem,O_2}=f(pO_2) \neq f(pH_2O)$ enables one to extract k_{Chem,H_2O} from two different values, which are $k_{Chem,tot}$ obtained at pH_2O = ~0 ($=k_{Chem,O_2}$) and $k_{Chem,tot}$ in the humidified conditions. From this approach, the extracted k_{Chem,H_2O} in the construction of Figure 3.10 as a function of pH_2O tends to increase with pH_2O. By taking a linear fit to all values of k_{Chem,H_2O}, the expression gives a correlation of

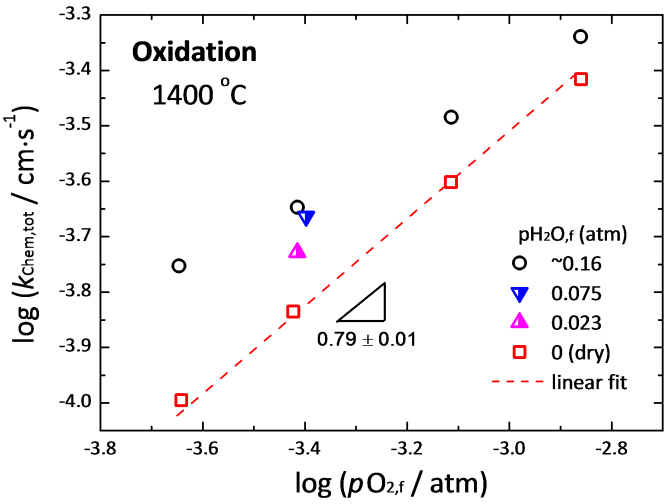

Figure 3.9: The total surface reaction rate constant, $k_{\mathrm{Chem,tot}}$, for the oxidation of ceria extracted from conductivity relaxation profiles in Figure 3.8(b) and 3.9(b) at 1400 °C.

$$k_{\mathrm{Chem,H_2O}}/cm \cdot s^{-1} = 10^{-(3.86\pm0.02)} \cdot (p\mathrm{H_2O}/atm)^{0.31\pm0.02} \tag{3.20}$$

By combining Eq. (3.19) and (3.20), is generalized as

$$\begin{aligned} k_{\mathrm{Chem,tot}}/cm \cdot s^{-1} =& (k_{\mathrm{Chem,O_2}}/cm \cdot s^{-1}) + (k_{\mathrm{Chem,H_2O}}/cm \cdot s^{-1}) \\ =& 10^{-(1.14\pm0.04)} \cdot (p\mathrm{O_2}/atm)^{0.79\pm0.01} \\ &+ 10^{-(3.86\pm0.02)} \cdot (p\mathrm{H_2O}/atm)^{0.31\pm0.02} \end{aligned} \tag{3.21}$$

and the three k_{Chem} results as a function of $p\mathrm{O_2}$ and $p\mathrm{H_2O}$ are displayed in Figure 3.11 all together with the experimental results. As a reminder, the result is applied only to the material-kinetic limited condition. The experimental conditions in this study satisfy the followings: i) the oxide has enough driving force to dissociate $\mathrm{H_2O}$ for taking the oxygen from $\mathrm{H_2O}$ due to relatively high temperature and/or low $p\mathrm{O_2}$, and therefore two oxidants ($\mathrm{O_2}$, $\mathrm{H_2O}$) participate in the oxidation reaction of the oxide; ii) enough oxidants are supplied (i.e., sufficiently high molar gas flow rate per mole of oxide) compared to the absolute oxygen nonstoichiometry change driven by the perturbation in $p\mathrm{O_2}$. More precisely regarding the judgement of the enough amount of supplied oxidants, 2 × $p\mathrm{O_2}$ × (gas flow rate) would be regarded as the supplied amount of oxygen from $\mathrm{O_2}$ gas per unit time. For $\mathrm{H_2O}$, $p\mathrm{O_2}$ × ψ × (gas flow rate) would be the supplied oxygen from $\mathrm{H_2O}$ if the oxide reacts with all of

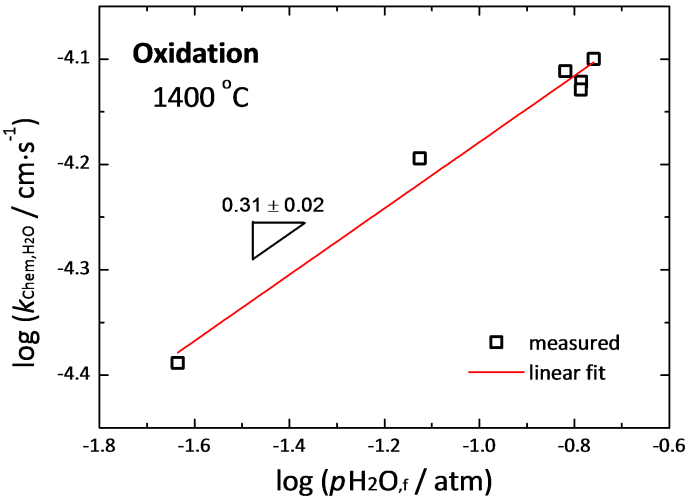

Figure 3.10: The surface reaction rate constant relevant to H_2O, k_{Chem,H_2O}, for the oxidation of ceria as a function of final pH_2O at 1400 °C.

the supplied H_2O. This understanding guides how to interpret the oxidation kinetics in thermochemical fuel production both through temperature swing and pressure swing modes, as well as in the surface reaction study as the fundamental material evaluation. For example, in the thermochemical cycling through the pressure swing at which the oxide is reduced at high temperature (~1500 °C) and then exposed to the humidified atmosphere at the identical temperature, the surrounding will be the mixture of H_2O and O_2 due to the thermolysis of H_2O. Therefore, the oxidation kinetics, if the supplying gases are sufficient to overcome the gas-phase limit, will be controlled by $k_{Chem,tot}$, which is the sum of k_{Chem,O_2} and k_{Chem,H_2O}.

For the thermochemical cycling through the temperature swing at which the oxide is reduced at high temperature (~1500 °C) and then exposed to the humidified atmosphere at low temperature (~800 °C), the initial state of the oxide at low temperature is assigned to the relatively large nonstoichiometry which is equilibrated in low pO_2 at that temperature (the effective pO_2 of ~10^{-21} atm at 800 °C for ceria), and therefore the oxide potentially dissociate H_2O for taking the oxygen from that. It implies that the oxidation kinetics will be identified by k_{Chem,H_2O}. In a similar way, if one tries to examine the surface reaction rate constant of the material by the chemical relaxation methods (*e.g.*, electrical conductivity relaxation or mass relaxation) in very reduced atmosphere obtained by flowing H_2/H_2O/Ar or CO/CO_2 mixtures, the overall oxidation reaction will be controlled by k_{Chem,H_2O} or k_{Chem,CO_2}, not by k_{Chem,O_2}, because i) the supplied amount of O_2 is not sufficient in such a low

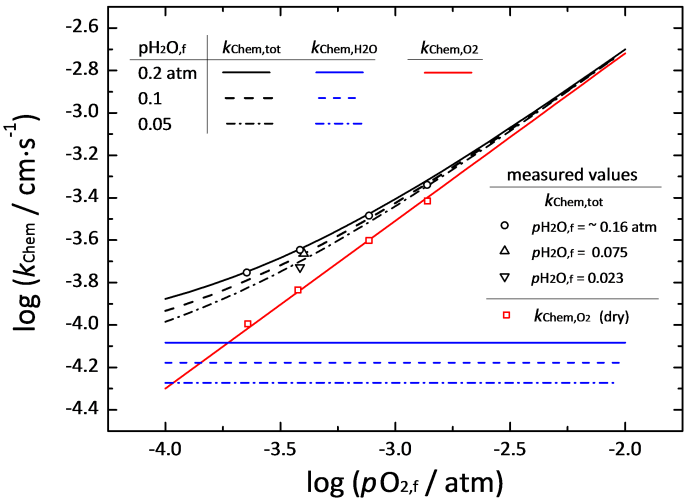

Figure 3.11: The three surface reaction rate constants, $k_{\mathrm{Chem,O_2}}$ (in Eq. (3.19), red straight line), $k_{\mathrm{Chem,H_2O}}$ (in Eq. (3.20), blue straight lines), and $k_{\mathrm{Chem,tot}}$ (in Eq. (3.21), black curved lines) of oxidation reaction, respectively, in comparison with the experimentally obtained $k_{\mathrm{Chem,tot}}$ for the oxidation reaction as a function of pO2 and $p\mathrm{H_2O}$ at 1400 °C.

$p\mathrm{O_2}$ regime and ii) the material has strong thermodynamic driving force to dissociate $\mathrm{H_2O}$ or $\mathrm{CO_2}$ as anticipated in Figure 3.1(b). It implies that $p\mathrm{H_2O}$ or $p\mathrm{CO_2}$ would be decisive parameters governing the overall oxidation reaction in such a reduced atmosphere. Significantly, Yashiro et al.[25] and Lane et al.[12] already suggested that surface reaction rate is not directly related to oxygen partial pressure but depends on the gas species. To sum, the surface reaction rate of the nonstoichiometric oxide is not only a function of temperature and $p\mathrm{O_2}$, but also a function of $p\mathrm{H_2O}$ in certain conditions such as high temperature and/or low oxygen partial pressure.

3.5 Conclusions

The surface reaction constant of undoped ceria, accurately measured at 1400 °C under high gas flow rates, displays a surprisingly steep dependence on oxygen partial pressure, with a power law exponent of 0.84 ± 0.02 in the range of -4.3 ≤ log(pO$_2$ / atm) ≤ -2.0. Under these conditions, the dominant defect species, oxygen vacancies and free electrons, both decrease in concentration with increasing pO$_2$, suggesting other factors are at play. This result appears to be amongst the first reports of k_{Chem} for the direct reaction of an n-type oxide with oxygen. By analogy to p-type conductors, we speculate that the rate-determining step involves diatomic oxygen species.

The k_{Chem} was also investigated as a function of pH$_2$O via ECR. The conductivity relaxation profiles driven by small perturbation in even in both of pO$_2$ (ΔpO$_2$) and pH$_2$O (ΔpH$_2$O) were well explained by the simple exponential decay expression at which only one k_{Chem} value was contained. From the fact that the total oxygen flux at the interface of gas/solid is a simple sum of each flux sourced from O$_2$ and H$_2$O, it is shown that k_{Chem} in the humidified conditions consists of a sum of $k_{\mathrm{Chem,O_2}}$ and $k_{\mathrm{Chem,H_2O}}$. From this correlation, $k_{\mathrm{Chem,O_2}}$ and $k_{\mathrm{Chem,H_2O}}$ were successfully separated in the range of (~0 ≤ (pH$_2$O / atm) ≤ ~0.16) and ($10^{-3.85}$ ≤ log (pO$_2$ / atm) ≤ $10^{-2.86}$). This result implies that the surface reaction rate of the nonstoichiometric oxide is not only a function of temperature and pO$_2$, but also a function of pH$_2$O in certain conditions such as high temperature and/or low oxygen partial pressure; thus one should carefully consider pH$_2$O as another thermodynamic parameter affecting the surface reaction rate.

Supplemental Information of Ch.3

Influence of flow rate

Relaxation profiles obtained as a function of gas flow rate are presented in Figure 3.13 over the range of 78 to 523 sccm/g. A clear increase in the relaxation rate with increasing flow rate is evident. The largely flow-rate independent characteristics of the reactor alone, Figure 3.16 (Supplemental Information), justify attribution of this behavior to the material and its interaction with the reactant gas. All of the relaxation profiles were well described by the exponential form with reduced R^2 values >0.9997 and (error of τ)/τ < 0.2%. The quality of the fit to the lowest flow rate (78 sccm/g) and the highest flow rates (523 sccm/g) data sets are shown in Figure 3.13(b) as representative examples.

The resultant set of relaxation time constants are summarized in Figure 3.14, along with the behavior predicted at low flow rate for a gas-phase limited process and at high flow rate for a surface-reaction limited process. The τ are indeed flow-dependent at low flow rates (78–418 sccm/g) and flow-independent at high flow rates (418–523 sccm/g). However, the low flow regime does not match the thermo-

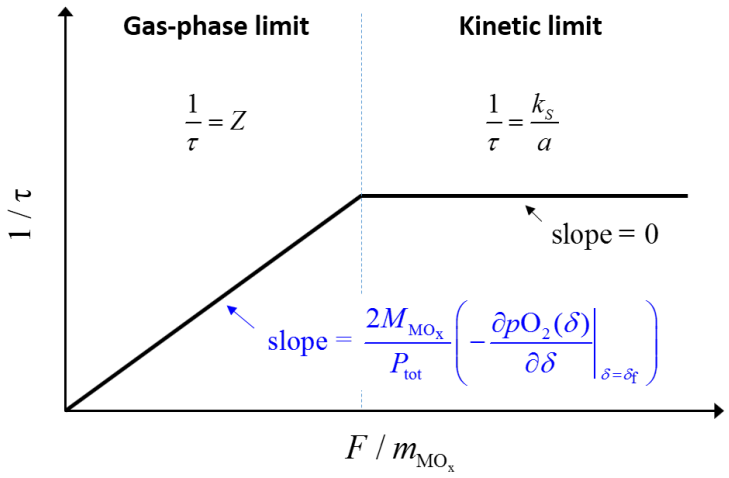

Figure 3.12: Schematic illustration of the time constant as a function of the flow rate under the gas-phase limit and the surface reaction limit.

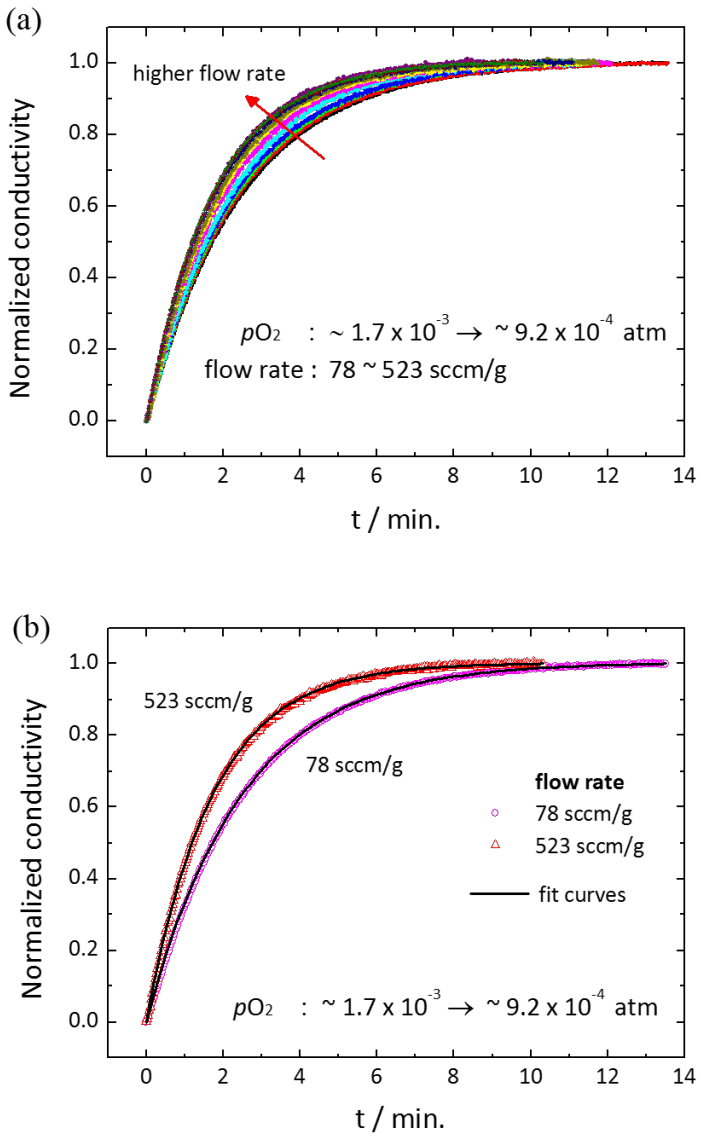

Figure 3.13: Conductivity relaxation behavior at 1400 °C for a pO_2 switch from (1.6 ± 0.2) × 10^{-3} to (9.1 ± 1.0) × 10^{-4} atm: normalized conductivity relaxation profiles at (a) various flow rates (78 to 523 sccm/g), and (b) 78 and 523 sccm/g. Solid lines are the best fits to the exponential decay function.

dynamic expectation, and moreover, the transition between the two regions is much more gradual than shown schematically on Figure 3.12. The deviation is attributed to the strong likelihood that only a small portion of the gas interacts with the solid as it passes through the reactor, and thus the effective gas flow rate per unit mass of oxide is much lower than the supplied value. Indeed, given the small width of the sample (5.48 mm) relative to the 1 cm inner diameter of the reaction chamber

and an estimated gas-phase diffusion coefficient of O_2 in the O_2–Ar mixture of 4.5 cm^2s^{-1} at 1400 °C,[72] it can be readily computed that a residence of time of at least 0.26 s is required for the gas at the periphery of the reactor to come in contact with the center of the sample. Achieving such a residence time over the 1.9 cm length of the sample, in turn, requires a gas velocity of ≤7.3 cm/s, equivalent to a flow rate of ≤35 sccm. The utilized flow rates are much higher, consistent with the suggestion that $k_{\mathrm{Chem}}^{\mathrm{apparent}}$ is lowered from the theoretical value because the gas does not fully interact with the sample.

A key conclusion to be drawn from these flow rate dependent measurements is that at high flow rates material kinetic properties can successfully be accessed. The exponential form of the relaxation profile observed here in the flow-rate independent regime implies that the surface reaction step dominates the relaxation behavior, with negligible contribution from solid-state diffusion (*i.e.*, $D_{\mathrm{Chem}} \gg k_{\mathrm{Chem}} \cdot a$ under these measurement conditions). Significantly, the profiles continue to obey an exponential form even when gas flow rate is important, as predicted from an analysis of gas-phase limited dynamics. While seeking out flow-rate independent behavior seems, perhaps, self-evident as a minimum criterion for determining whether true material behavior has been measured,[87] documentation of such behavior appears relatively rare. Moreover, Lohne *et al.* have gone so far as to suggest that, at high temperatures and low oxygen partial pressures, flow rates (specifically, gas phase velocities) cannot be made large enough to avoid experimental artifacts resulting from unfavorable gas dynamics, in turn, caused by uptake or release of oxygen from the oxide.[76] On the basis of numerical simulations, the authors conclude that boundary layer effects, which create a gradient in gas composition from the sample surface to elsewhere in the gas phase, cannot be overcome, implying that plateau behavior cannot be observed. The results obtained here, in which a plateau clearly emerges, demonstrate that, in fact, even at high temperatures and relatively low oxygen partial pressures ($<10^{-3}$ atm), kinetic properties can be determined by ECR methods. The discrepancy between the two works likely results because the oxygen release from ceria under the present experimental condition is not as large as that for the material and conditions considered by Lohne *et al.*[76] Furthermore, the carrier gas used here is Ar, which leads to a relatively high gas-phase diffusivity and diminishes boundary layer effects.

In the absence of *a priori* knowledge of the material properties, a simple way

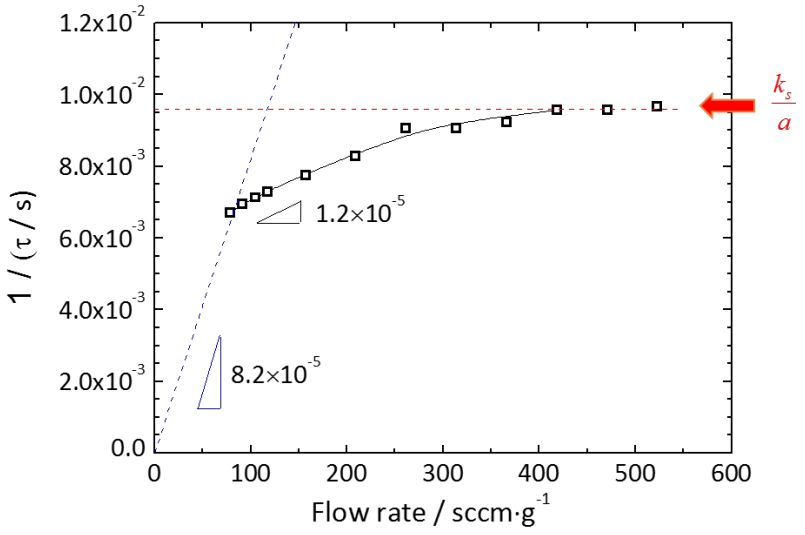

Figure 3.14: The time constant as a function of flow rate derived by fitting to an exponential decay (Eqns. (3.3) or (2.4)). The dotted lines are expected trends under the gas-phase limit (blue) and the surface reaction limit (red). The solid curve is a visual guidance for the measured values.

to distinguish the two types of behaviors is to evaluate the impact of flow rate (F) on the time constant (τ). Whereas τ is insensitive to F when the material is limited by surface reaction kinetics, it is inversely dependent on F when the system is under gas-phase control. The situation is depicted schematically in Figure 3.12. As indicated in the figure, one can expect $1/\tau$ to vary linearly with F up to a value, F_{tr}, at which Z = k_{Chem}/a. This equality yields

$$\frac{F_{\mathrm{tr}}}{m_{\mathrm{CeO_2}}} = \frac{k_{\mathrm{Chem}}}{a}\frac{P_{\mathrm{tot}}}{2M_{\mathrm{CeO_2}}}\left(-\left.\frac{\partial p\mathrm{O_2}(\delta)}{\partial\delta}\right|_{\delta=\delta_{\mathrm{f}}}\right)^{-1} \tag{3.22}$$

where $m_{\mathrm{CeO_2}}$ is the total mass of the oxide, $M_{\mathrm{CeO_2}}$ is the molar mass of the oxide, and $n_{\mathrm{CeO_2}} \approx \frac{m_{\mathrm{CeO_2}}}{M_{\mathrm{CeO_2}}}$. Although not exploited in this work, it is noteworthy that this transition flow rate depends not only on the sample mass, but also on the sample thickness ($2a$).

Knowledge of the surface reaction rate across the oxygen partial pressure regime of interest, in combination with the known redox thermodynamics of ceria, enables a precise evaluation of the transition flow rate expected to delineate gas-phase and

material-kinetic limited regimes. An approximate solution for $F_{\mathrm{tr}}(p\mathrm{O}_2)$ can be obtained by insertion of Eq. (3.15) into Eq. (3.22). A more precise solution, valid beyond the constraint of $p\mathrm{O}_2(\delta) \ll P_{\mathrm{tot}}$, can be obtained by numerical treatment of Eq. (3.23).

$$\frac{\partial \delta}{\partial t} = \frac{2F}{n_{\mathrm{CeO}_x}} \left(\frac{p\mathrm{O}_2(\delta) - p\mathrm{O}_2^{in}}{P_{\mathrm{tot}} - p\mathrm{O}_2(\delta)} \right) \tag{3.23}$$

where F is molar flow rate of gas, n_{CeO_x} is the total moles of the oxide (taken here to be ceria), P_{tot} is the total pressure of gas, and $p\mathrm{O}_2^{\mathrm{in}}$ is the oxygen partial pressure supplied upon application of the perturbation. The term $p\mathrm{O}_2(\delta)$ is the time-dependent oxygen partial pressure of the gas inside the reaction chamber, in equilibrium with the solid of oxygen content δ.

The results of these two methods of computing $F_{\mathrm{tr}}(p\mathrm{O}_2)$ are presented in Figure 3.15(a), and a schematic illustrating the expected behavior of the relaxation time as a function of flow rate at different $p\mathrm{O}_2$ values presented in Figure 3.15(b). For the conditions explored (1400 °C with $p\mathrm{O}_2$ ranging from $10^{-4.5}$ to $10^{-1.5}$ atm) the two methods of calculation produce essentially identical results. More significantly, it is evident that the gas flow rates required to ensure that gas phase limitations are overcome increase dramatically with decreasing oxygen partial pressure. This is a consequence of the redox thermodynamics of ceria, in which the magnitude of $\mathrm{d}p\mathrm{O}_2/\mathrm{d}\delta$ decreases with decreasing $p\mathrm{O}_2$, causing the slope in the flow rate dependent regime of $1/\tau$ (= Z) to decrease. In principle, the decreasing value of k_{Chem} with decreasing $p\mathrm{O}_2$, Figure 3.6, would shift $F_{\mathrm{tr}}(p\mathrm{O}_2)$ to lower flow rate, but this effect is overwhelmed by the thermodynamic behavior. Along with the computed curves, shown in Figure 3.15(a), is the flow rate at which the relaxation behavior was observed to become independent of flow rate. As noted above, this substantial difference is tentatively attributed to a large volume of gas flowing past the sample without interacting with it, in other words, insufficient mixing in the gas phase as a consequence of limited mass transport in the gas. Overall, it is apparent that identification of a suitable flow rate for one set of experimental conditions may not be sufficient to ensure that gas-phase limitations have been overcome for all experimental conditions of interest.

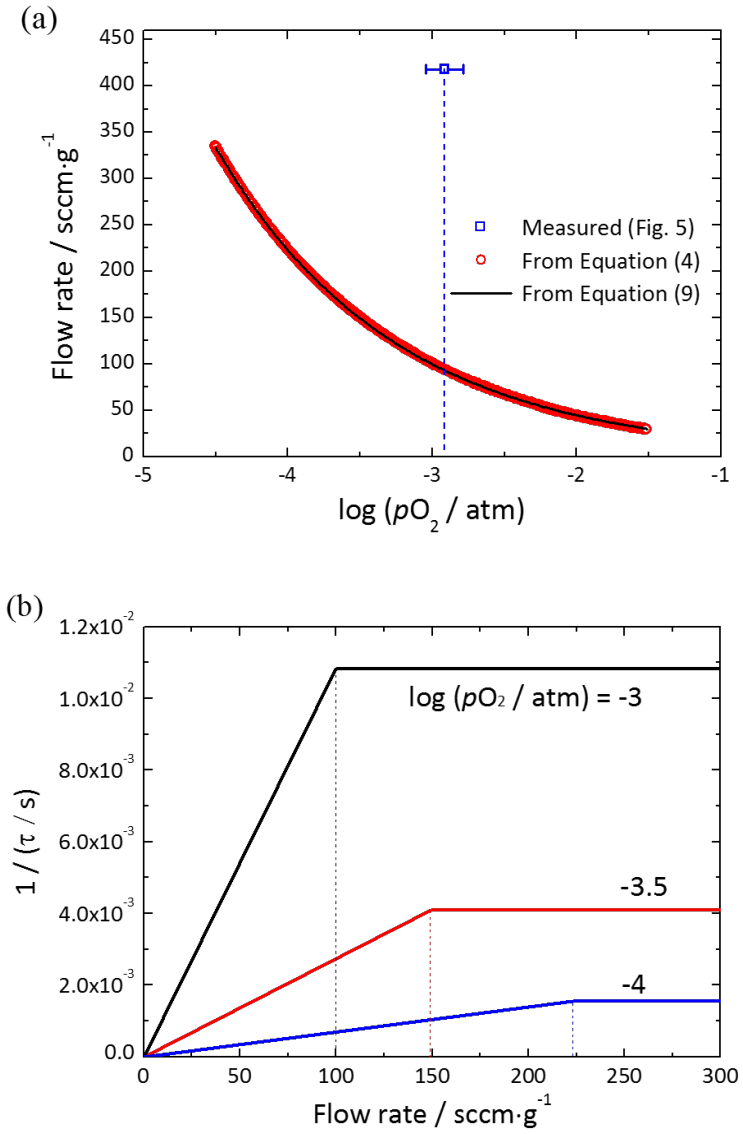

Figure 3.15: (a) Theoretically calculated flow rate at a transition point from the gas-phase to the surface reaction limits for undoped ceria within the range of pO_2 from $10^{-4.5}$ to $10^{-1.5}$ atm at 1400 °C. Red circles are calculated from numerical treatment of Eqn. (3.23), the solid curve is from Eqn. (3.22), and the blue open square is the value experimentally observed in Figure 3.14. (b) $1/\tau$ vs. flow rate at pO_2 = 10^{-3}, $10^{-3.5}$, and 10^{-4} atm. The dotted vertical lines indicate the flow rate at the transition point for each value of pO_2.

Impact of flow rate on steady state pO_2 of experimental apparatus

As shown in Figure 3.16(a), for the majority of the experimental conditions, the measured oxygen partial pressure coincided with the supplied value. At the lowest flow rates, however, the actual pO_2 in the system deviates somewhat from the nominal value, as shown for two representative values of $(1.59 \pm 0.02) \times 10^{-3}$ and $(7.82 \pm 0.14) \times 10^{-4}$ atm. This is a result of slight leaks becoming important relative to the volume of gas supplied. The greatest deviation of $\sim 40\%$ is smaller, by about a factor of 2, than the typical step change in pO_2 employed in this study. Thus, the impact of the deviation of the actual pO_2 from the nominal value is negligible.

The influence of slight leaks on the reactor flush time is also greatest at low gas flow rates. Shown in Figure 3.16(b) are the normalized pO_2 profiles for relatively large step changes between 8.0×10^{-4} and 1.6×10^{-3} atm ($|\Delta \log(pO_2/\text{atm})| = 0.30$). Under these conditions, the reactor response time-constant (τ), established by fitting an arbitrary exponential profile of the form of Eq. (3.3), reaches a stable value of $\sim$ 10 s for flow rates of 100 sccm and higher. At the lowest flow rate, the time constant rises slightly to $\sim$ 12.5 s. The shortest material response time encountered in this work was $\sim$ 103 s, almost an order of magnitude larger than the longest reactor response time, indicating that the material rather than reactor behavior was captured over the entire range of conditions evaluated.

The results presented in Figure 3.13 and 3.14, showing a relaxation time constant that is dependent on flow rate might, at first glance, be attributed to an artifact of the increasing influence of leaks at low flow rates. For such an explanation to apply, it would require that k_{Chem} decrease with increasing oxygen partial pressure. However, as shown in Figure 3.6 , the surface reaction rate increases with increasing pO_2, and hence leaks cannot be responsible for the observed behavior.

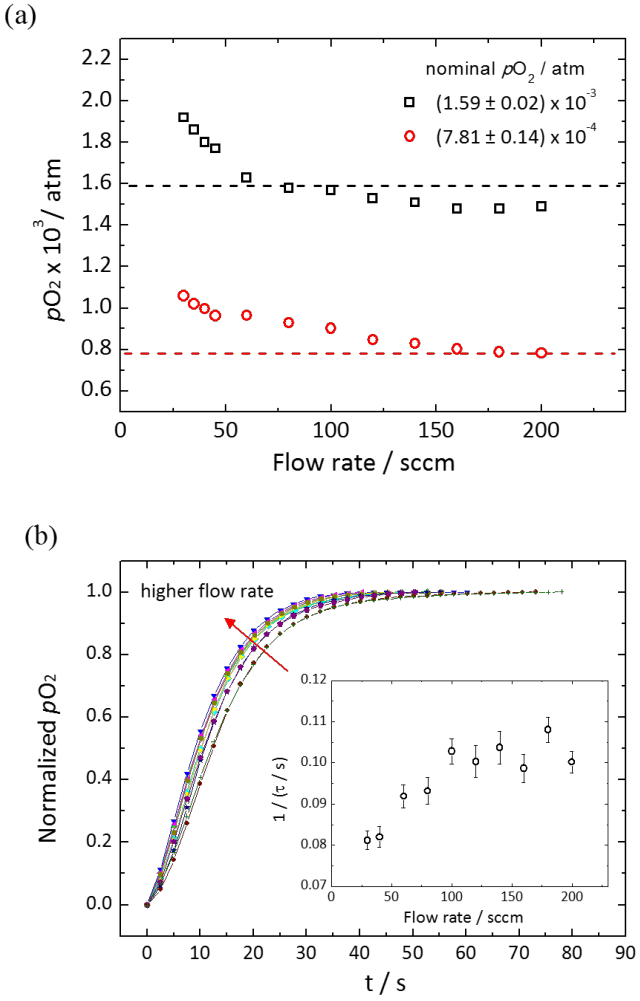

Figure 3.16: Impact of flow rate on steady state oxygen partial pressure and on the time scale of response of the experimental apparatus to step changes in oxygen partial pressure: (a) Variation in steady state oxygen partial pressure as a function of flow rate (as recorded by the in situ oxygen sensor) for nominal input pO_2 values as specified and also indicated by the horizontal dashed lines; (b) reactor relaxation profiles as a function of flow rate for switching between $(1.59 \pm 0.02) \times 10^{-3}$ and $(7.82 \pm 0.14) \times 10^{-4}$ atm. Inset shows reactor relaxation times. All measurements at T = 1400 °C. The range of flow rates examined, where 30 to 200 sccm correspond, for a typical sample mass of 0.38 g, to mass normalized flow rates of 78 to 523 sccm/g.

Calculation of pH_2O

For converting pH_2O at ~90 °C to that at 1400 °C, the reaction of thermolysis of H_2O(g) is considered as below. Hereafter, subscripts *LT* and *HT* indicate the measured at low and high temperature, respectively.

	$H_2O(g)$	$\rightarrow$	$H_2(g)$	+	$^1/_2O_2(g)$
initial (90 °C)	(pH_2O_{LT}/p_{tot})		~ 0		$(pO_{2,LT}/p_{tot})$
change	- x		x		$^1/_2x$
final (1400 °C)	$(pH_2O_{LT}/p_{tot})-x$		x		$(pO_{2,LT}/p_{tot}) + {}^1/_2x$

(3.24)

where p_{tot} is total pressure considered as 1 atm here, $pO_{2,LT}$ is the oxygen partial pressure at ~90 °C which is unknown, and x is the concentration of H_2O consumed by thermolysis. The pH_2O_{LT} $pO_{2,HT}$ are the experimentally measured values by the *ex-situ* humidity sensor (~ 90 °C) and in-situ oxygen sensor (1400 °C) at total pressure of 1 atm, therefore,

$$\frac{pO_{2,HT}}{p_{tot}} = \frac{pO_{2,LT} + ({}^1/_2x \cdot p_{tot})}{p_{tot} + ({}^1/_2x \cdot p_{tot})} \tag{3.25}$$

$$\frac{pH_2O_{HT}}{p_{tot}} = \frac{pH_2O_{LT} - (x \cdot p_{tot})}{p_{tot} + ({}^1/_2x \cdot p_{tot})} \tag{3.26}$$

The expression for the thermodynamic equilibrium constant, K_{H_2O}, for reduction reaction at 1400 °C is given

$$K_{H_2O,red}(1400^oC) = \frac{x \cdot [(pO_{2,LT}/p_{tot}) + {}^1/_2x]^{1/2}}{(pH_2O_{LT}/p_{tot})-x} \tag{3.27}$$

By solving simultaneous equations of Eq. (3.25) and (3.27) for pO_2, *LT* and x, pH_2O at 1400 °C is simply calculated by Eq. (3.26). The results for actual experimental conditions are summarized in Table 3.1.

Table 3.1: Thermodynamic calculation of pH_2O at 1400 °C

pO_2 at 1400 °C / atm (in-situ)	pH_2O at $90C/atm$ (ex-situ)	pO_2 at $90C$ (calculation)	pH_2O at 1400 °C / atm (calculation)
2.258×10^{-4}	0.1640	1.455×10^{-4}	0.1638
3.850×10^{-4}	0.1743	3.195×10^{-4}	0.1742
3.922×10^{-4}	0.0750	3.643×10^{-4}	0.0749
3.783×10^{-4}	0.0232	3.695×10^{-4}	0.0232
7.694×10^{-4}	0.1519	7.291×10^{-4}	0.1518
1.378×10^{-4}	0.1637	1.345×10^{-4}	0.1636

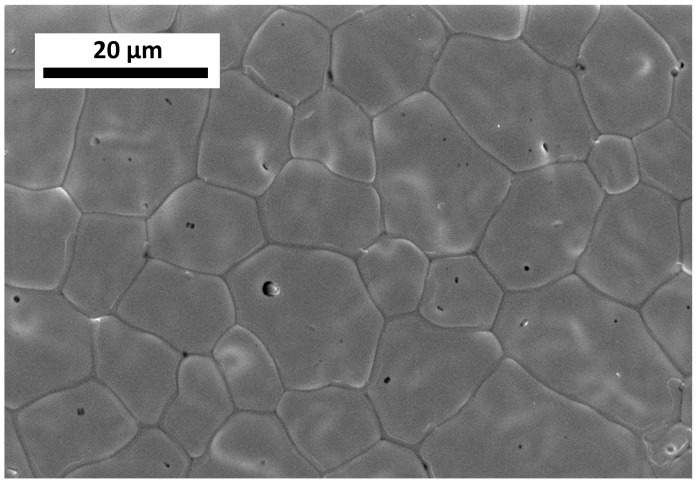

Figure 3.17: SEM micrograph of surface of dense ceria.

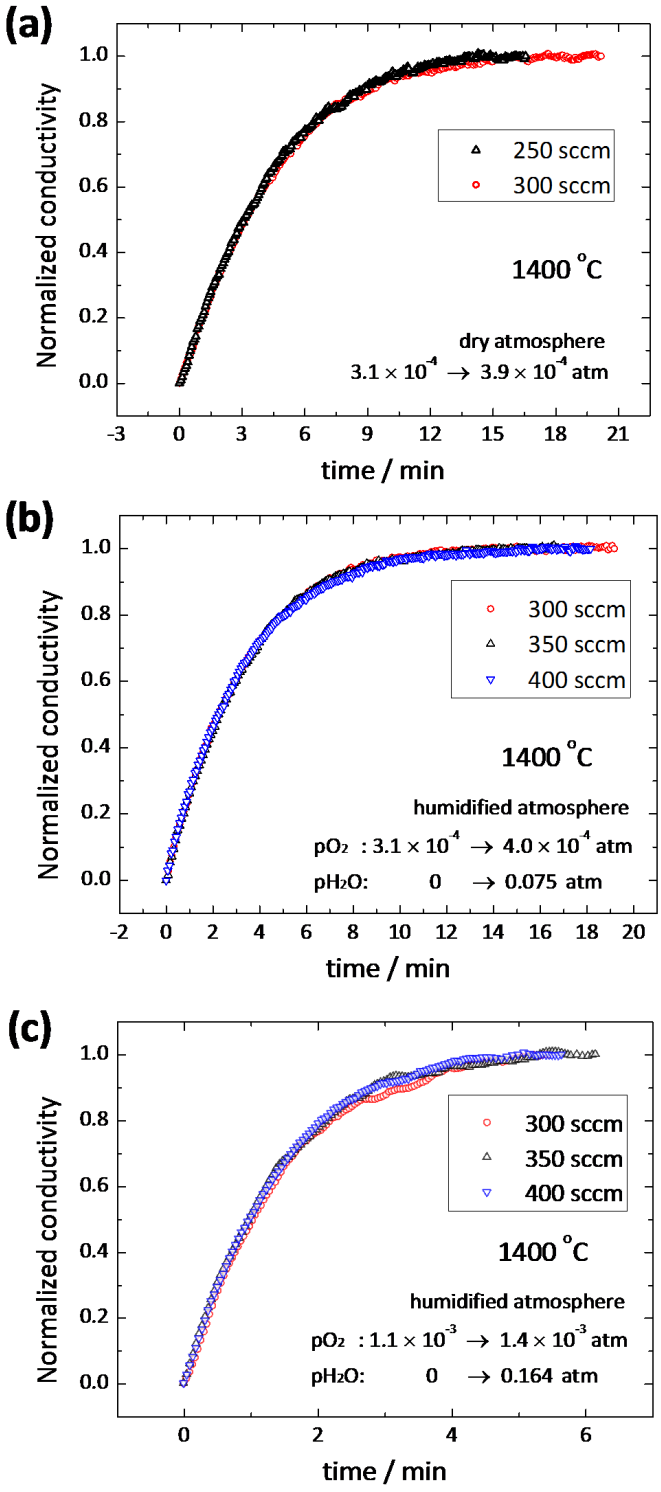

Figure 3.18: Normalized conductivity relaxation profiles at various flow rates (a) in dry and (b-c) humidified atmosphere at 1400 °C.

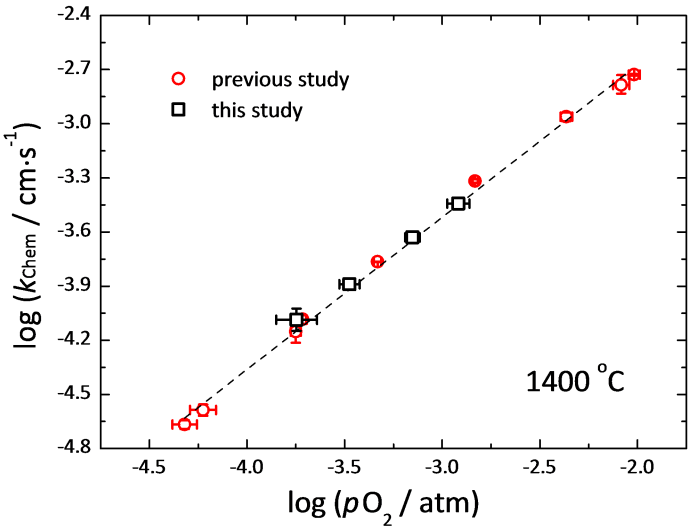

Figure 3.19: Surface reaction constant of O_2, k_{Chem,O_2}, of ceria as a function of pO_2 at 1400 °C obtained from the best fits to the relaxation profiles in Figure 3.7.

Chapter 4

MATERIAL-KINETIC PROPERTY AT MODERATE TEMPERATURE: MASS RELAXATION METHOD

4.1 Introduction

The electrical conductivity relaxation method is perhaps the most widely employed among the available methods for determining k_{Chem} (along with the chemical diffusion coefficient, D_{Chem}) because of the ease with which high precision conductivity measurements can be made using samples of almost arbitrary dimensions. In some instances, however, mass changes in a material may occur in response to a change in oxygen partial pressure without a concomitant change in conductivity. This will occur, for example, in a predominant electronic conductor which displays a Brouwer region of $n = p$ (where n is the free electron concentration and p is the hole concentration) despite a variable concentration of the minority ionic defects, specifically, oxygen vacancies, within that regime. For such a material, an alternative method is required. A mass relaxation experiment can provide the required sensitivity and, moreover, offers the possibility of directly yielding the oxygen content as a function of thermodynamic conditions.

To date, mass relaxation experiments have been performed using conventional thermogravimetric analyzers. [24–26, 88] This approach suffers, however, from two key drawbacks. The first is about the gas flow configuration such that a step change in oxygen partial pressure cannot be readily applied to the material; upstream mixing typically creates a less sharply defined oxygen partial pressure profile. The second is that the change in gas composition introduces a change in buoyancy that is recorded by the instrument as a mass change, which becomes convoluted with the true mass change. Additional challenges arise from the need to use a large sample to record a detectable mass change. This requirement can result in an undefined spatial gradient in oxygen concentration about the sample, and may also preclude measurement of k_{Chem}, which requires use of thin samples with short-to-negligible diffusion lengths.

In this work, a new system for precise mass relaxation studies is introduced, and a proof-of-principle study is carried out using 10% praseodymium-doped ceria

(10PCO). The new methodology relies on the use of a piezocrystal microbalance for measurement of small mass changes in a thin film of the oxide. As quartz loses its piezoelectric properties above 573°C [89] and becomes largely unusable for thin-film mass sensing above 300°C, [90] this system is based on gallium phosphate, which remains in the appropriate crystalline phase to about 970 °C. [91, 92] Measurements are made here at a temperature of 700 °C and an oxygen partial pressure range 10^{-4} to 10^{-2} atm, across which 10PCO undergoes measurable stoichiometry changes but exhibits regions of negligible conductivity change. [93] The newly developed experimental station displays very short flush times and has the precision required to perform accurate mass relaxation studies for extraction of material kinetic parameters. By use of a thin-film sample, the relaxation profiles directly yield the surface reaction constant, without need for intensive fitting to the data to deconvolute k_{Chem} from D_{Chem}.

4.2 Backgrounds

Piezocrystal microbalances are routinely used to measure the mass of a thin film. Deposition of a film on a piezocrystal induces a shift in the bulk shear wave resonance frequency relative to that of the crystal alone.[91] The composite resonance frequency, f_{R} (that of the system composed of the crystal and the film), is a function of the masses of the crystal and film, their shear-mode acoustic impedances, and the specific measurement geometry.[94] An exact solution has been reported for a one-dimensional geometry in which the film is additionally treated as a purely mechanical resonator, with no electrical influence on the piezoelectric behavior of the crystal. [95–98] This treatment is the basis of the Z-match method employed in modern quartz crystal monitors of film thickness in commercial film growth systems.[99] If the relevant material properties are known, the mass (and hence film thickness) measurement is accurate over shifts in frequency up to several tens of percent.[100, 101] In practice, however, due to the poor availability of shear modulus values which enter into the acoustic impedance, film thickness monitors are typically employed in conjunction with direct experimental calibrations, a procedure that must be periodically repeated due to continuous addition of deposited film from one growth to the next.[99]

When film thickness is small, the shift in frequency is also small, and the relationship between mass and frequency can be treated as linear.[102] Similarly, even if a film is already deposited on a piezocrystal, application of a small amount of additional mass to the composite system results in an approximately linear response as evident, for example, from the relationship between film mass and frequency shift, reported for a range of systems in the comprehensive analysis by Benes.[98] In this study, oxygen nonstoichiometry, δ, changes of less than 0.035 are explored, corresponding to film mass changes of just 0.33 % and much smaller changes in the mass of the composite system. Thus, even for a high mismatch in acoustical impedance between crystal and film, the resulting small-frequency shifts are safely treated as proportional measures of changes in mass (and hence in stoichiometry). Accordingly, the change in resonance frequency with time during the relaxation experiment directly yields the change in nonstoichiometry with time, a result expressed as

$$\frac{f_R(t) - f_R(0)}{f_R(\infty) - f_R(0)} = \frac{m_F(t) - m_F(0)}{m_F(\infty) - m_F(0)} = \frac{\delta(t) - \delta(0)}{\delta(\infty) - \delta(0)} \tag{4.1}$$

where $t = 0$ corresponds to the initial state, $t = \infty$ to the final state, and m_F is the mass of the film. Two piezoelectric materials have been considered in the literature for mass sensing at elevated temperatures: langasite ($La_3Ga_5SiO_{14}$) and gallium orthophosphate ($GaPO_4$).[92] The latter, whose piezoelectric phase is isostructural to α-quartz, has recently become commercially available as a piezoelectric material.[91] In addition to its high Curie temperature, it displays, for appropriate orientations, a relatively temperature-insensitive resonance frequency over a large range of temperatures.[103] Furthermore, it has a high electromechanical coupling constant, about twice as high as AT-cut quartz.[104] The few instances in which $GaPO_4$ has been utilized for high-temperature monitoring of mass changes demonstrate its promise for the present application. [90, 105, 106]

Praseodymium-doped ceria has recently been suggested as a high-productivity material for solar-driven thermochemical generation of hydrogen, with 10 % Pr showing optimal performance.[107] As a consequence of the variable valence of Pr, this system has also been the subject of several electrochemical studies.[93, 108–111] The defect chemical properties of the specific composition 10PCO have been comprehensively evaluated in the context of its consideration as a cathode in solid oxide

fuel cells.[93] At temperatures between 600 °C and 900 °C and oxygen partial pressures of $\sim 10^{-6}$ to $\sim 10^{-12}$ atm, Pr is almost fully reduced (to 3+) and Ce is almost fully oxidized (to 4+). Under these conditions, the stoichiometry can be approximated as $Ce_{0.9}Pr_{0.1}O_{1.95}$ and the material is a predominant ionic conductor with a pO_2-independent conductivity. Under higher oxygen partial pressures, Pr becomes increasingly oxidized to the 4+ state, generating non-negligible hole conductivity via the Pr impurity band; simultaneously, the oxygen vacancy concentration decreases, lowering the ionic conductivity. These opposing conductivity changes result in an oxygen partial pressure regime (between 10^{-4} and 10^{-2} atm, depending on temperature) over which the oxygen stoichiometry changes but the conductivity, within sensitivity limits, does not. These are precisely the conditions at which a mass relaxation experiment can reveal kinetic properties that a conductivity relaxation experiment cannot. The measurements performed here encompass this pO_2 range as well as more oxidizing conditions. Interestingly, at the highest oxygen partial pressures, the conductivity becomes dominantly n-type (with a conductivity that decreases with increasing pO_2) because the Pr impurity band within the band gap of the host oxide is almost filled.

In principle, a relaxation experiment can yield both the surface reaction and bulk chemical diffusion coefficient of a redox active oxide. The solutions describing the manner in which the oxygen stoichiometry varies with time and position across such an oxide (when the step change in oxygen partial pressure is sufficiently small as to justify an assumption of a linear response) are well known.[57] When the diffusion length is small relative to the characteristic length defined by the diffusion coefficient and surface reaction constant, the material response will be dominated by the surface reaction step. For a film of thickness a, this criterion becomes $a \ll L_C = D_{Chem}/k_{Chem}$ and, when it is obeyed, the solution to the 1-D mass relaxation problem reduces to

$$\frac{\delta(t) - \delta(0)}{\delta(\infty) - \delta(0)} = 1 - \exp\left(-\frac{k_{Chem}}{a}t\right) \tag{4.2}$$

Chen *et al.* have reported L_C of 10PCO to be $\sim 3.6 \times 10^3$ μm at 670 °C, [111] implying that in a 10 μm-thick film, bulk mass diffusion will play no role in limiting the relaxation behavior. Thus, a fit of the functional form of Eq. (4.2) to the normalized resonance frequency profile, which is directly proportional to the oxygen

stoichiometry profile, Eq. (4.1), will yield the surface reaction constant.

4.3 Experimentals

Commercial y-11.1° cut $GaPO_4$ piezocrystal (R-30, Piezocryst GmbH, diameter of 13.97 mm, thickness of 200 μm) with ~1 μm thick Pt electrodes covering over almost entire front side and deposited as a double-anchor shape at the back side was used as a mass sensor by detection of bulk shear waves, in Figure 4.1(a). The $GaPO_4$ crystal with Pt electrodes was annealed at 800 °C for 24 hours in stagnant air prior to deposit 10PCO film on the Pt electrode for improving the surface quality of the Pt electrodes. The 10PCO target for pulsed laser deposition (PLD) was prepared using the following procedure: the 10PCO powder was synthesized by a combined EDTA/citric acid chemical solution process. The powder was uniaxially pressed at 62 MPa and subsequently at 300 MPa for 20 minutes in a cold isostatic press, then sintered at 1400 °C for 10 h in stagnant air. Dense columnar film of 10PCO were grown on Pt electrode at the front side of $GaPO_4$ crystal by PLD using a Neocera PLD system equipped with a 248 nm KrF excimer laser. The laser energy was set at 300 mJ/pulse and the deposition frequency at 10 Hz under 10 mTorr of O_2 at the substrate temperature of 700 °C. The deposition was carried out by performing 20 sets of 25000 laser shots on the target, with 30 minutes breaks between each set. It resulted 6.2 μm thick film as shown in Figure 4.1(b). The cross-sectional image and surface morphology of the 10PCO film obtained by scanning electron microscopy (Hitachi S4800-II cFEG Scanning Electron Microscope) and atomic force microscopy (Bruker Dimension FastScan Atomic Force Microscope, Billerica, MA, USA). Crystal structure of the film was confirmed by X-ray diffraction (Rigaku Ultima IV, CuKa, Tokyo, Japan). The overall configuration of the sample is depicted in Figure 1(a). Zirconia-based oxygen sensor (MicroPoas®, Setnag) integrated with S-type thermocouple was positioned beneath the crystal for the real-time measurement. The resonance frequency of the crystal was measured at a rate of 10 Hz by piezocrystal monitor (STM-2, Inficon).

The mass relaxation measurements under small redox driving force (i.e. sufficiently small change in pO_2, $|\Delta\log(pO_2 / \text{atm})| < 0.3$) for extracting k_{Chem} were carried out at 700 °C in a range of $\sim 10^{-4} \leq pO_2 / \text{atm} \leq \sim 10^{-2}$.

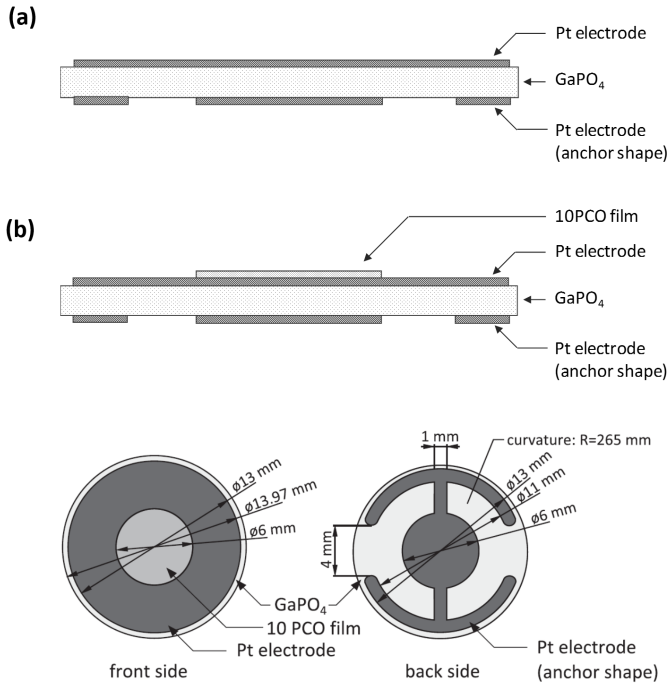

Figure 4.1: The $GaPO_4$ piezocrystal mass sensor: (A) Schematic cross-section without 10PCO thin film, and (B) with 10PCO thin film, showing from top to bottom 10PCO thin film, front/top side Pt electrode (almost fully covering the crystal), $GaPO_4$ crystal, and back/bottom side Pt electrode (double-anchor shape), and plan view technical drawings specifying front- and back-side Pt electrode dimensions as given by the manufacturer.[112]

4.4 Results and Discussion

The $GaPO_4$ crystal with Pt electrodes prior to deposit 10PCO film on the Pt electrode was annealed at 800 °C for 24 hours with tracking the resonant frequency, and then the temperature decreased to 700 °C with tracking the frequency as well. In Figure 4.2, the resonant frequency continuously decreased along time, but after the exposure at 800 °C for 24 hours, the frequency was quite stable at 700 °C, which is the temperature for the actual mass relaxation test for 10PCO film. This seems to be due to the morphology change of Pt electrodes such at 800 °C, and actually the SEM images of the surface of the Pt electrode (Figure 4.3) show that the surface quality was improved after this heat-treatment.

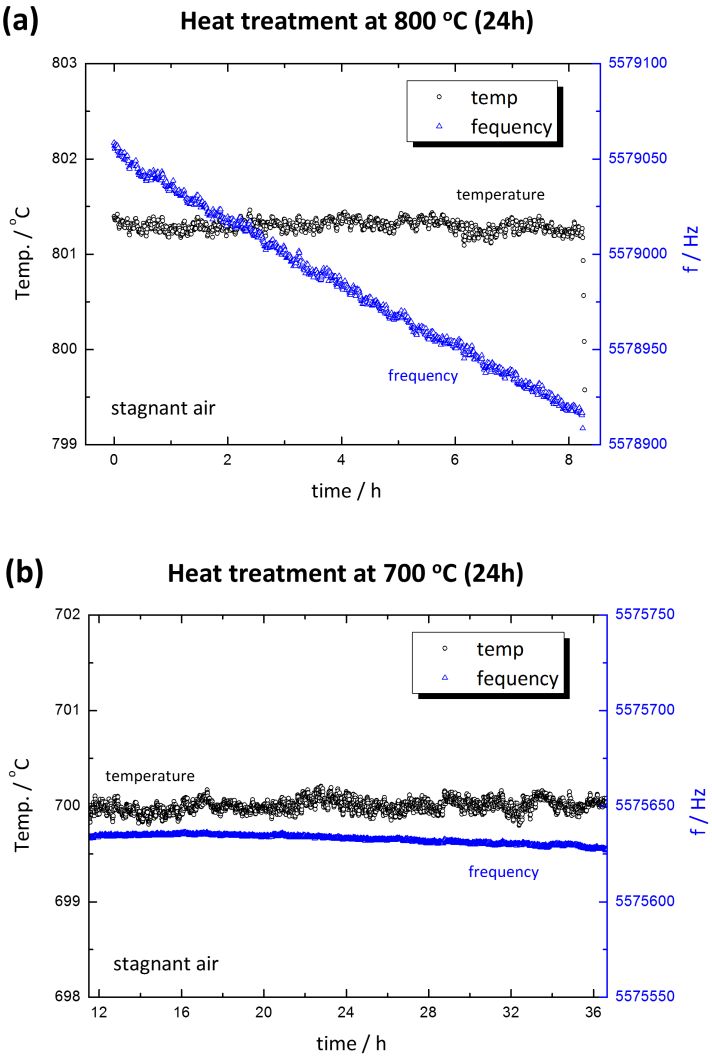

Figure 4.2: Resonant frequency drift of $GaPO_4$ crystal with Pt electrodes without 10PCO film against time at (a) 800 °C and (b) 700 °C.

A set of reference data were collected at a set temperature of 700°C using a bare gallium phosphate crystal onto which thick Pt electrodes had been applied to evaluate the system characteristics. The temperature, oxygen partial pressure, steam partial pressure, and resonant frequency were recorded over a period of 40 min, Figure 4.4. The temperature fluctuations were found to be ± 0.2 °C; no fluctuations in resonance frequency accompanied these minor temperature fluctuations.

Step changes in pO_2 between 10^{-2} and $10^{-3.5}$ atm were achieved within about 1 seconds. A slightly longer time scale for changing steam partial pressure is associated with the downstream location of the humidity sensor. Significantly, there is no de-

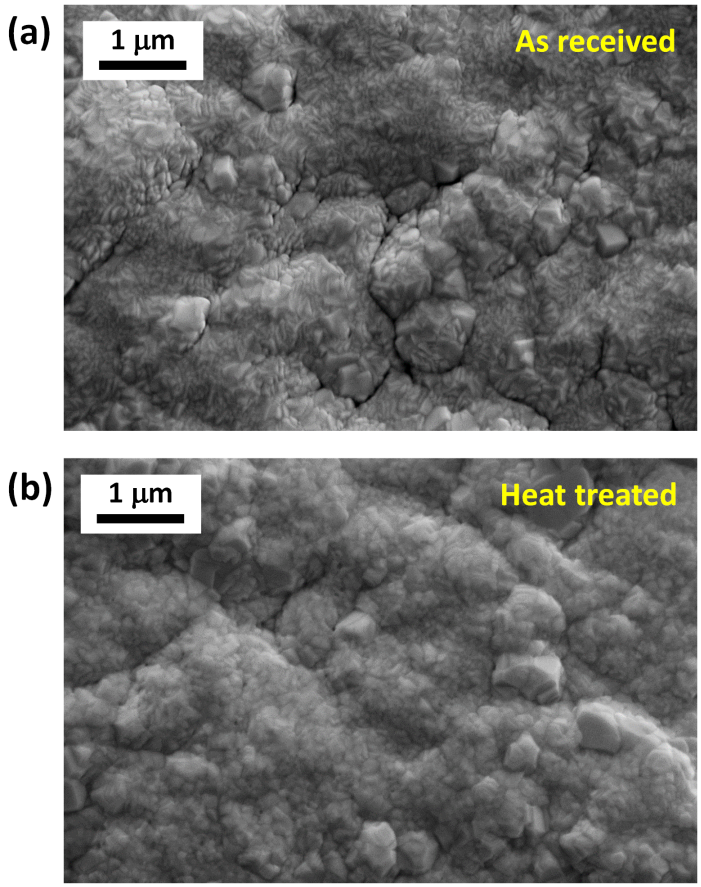

Figure 4.3: SEM images of Pt electrode surface (a) before and (b) after heat treatment at 800 °C for 24h followed by 700 °C for 24h.

tectable influence of oxygen partial pressure on the measured resonance frequency. This pO_2-independent frequency response is critical for successful implementation of gallium phosphate for mass relaxation studies where the change in mass is due to changes in pO_2. While steam partial pressure seemed to influence f_R, pH_2O was not varied in the experimental measurement of film properties and hence is not important here.

Cross-sectional and surface images of the 10PCO film obtained by scanning electron microscopy and atomic force microscopy are shown in Figure 4.5 and 4.6, respectively.

The SEM images reveal that the film is dense and of relatively uniform thickness, despite the somewhat undulating topology of the underlying $GaPO_4$ crystal. The

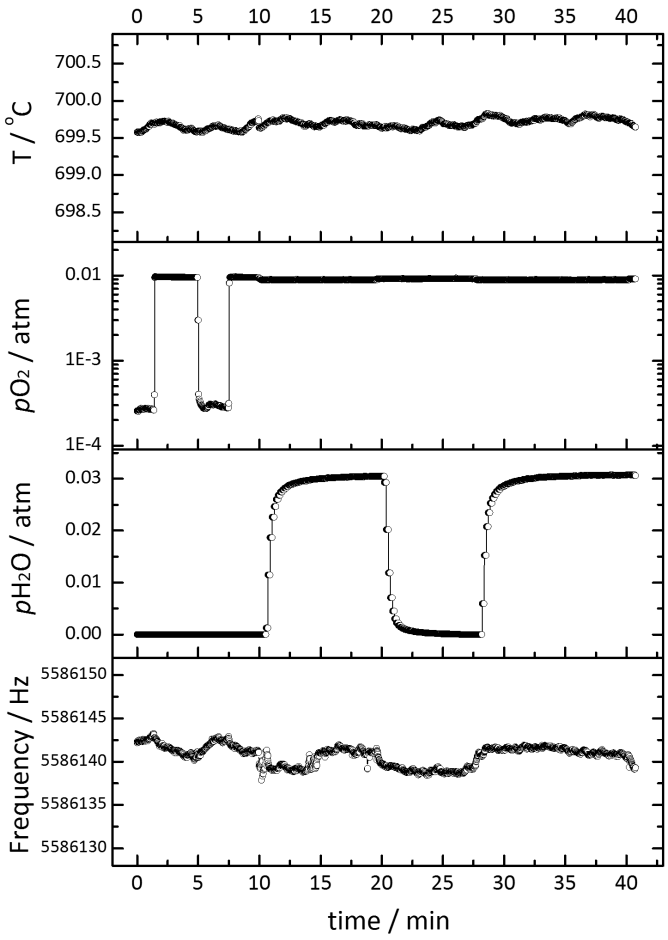

Figure 4.4: Characteristics of the high-temperature microbalance system measured at a set temperature of 700 °C and a total gas flow rate of 200 sccm: (A) temperature profile, (B) oxygen partial pressure profile, (C) steam partial pressure profile, and (D) resonant frequency profile. Independent step changes in pO_2 and pH_2O were applied as reflected in (B) and (C).

columnar morphology is typical of PLD growth in the absence of a lattice-matched substrate.[113] Analysis of phase contrast AFM images indicated grain sizes of and 62 ± 9 nm for the film deposited on the Pt. Growth of single-phase fluorite was confirmed by X-ray diffraction, which also revealed to be entirely randomly oriented as shown in Figure 4.7.

Peak broadening is furthermore evident in the diffraction patterns, generally consistent with the small crystallite sizes detected by AFM image analysis. From the cross-sectional SEM image, the thickness of the 10PCO film on a crystal with Pt electrode is measured to be 6.2 μm. The rms surface roughness value, as estimated

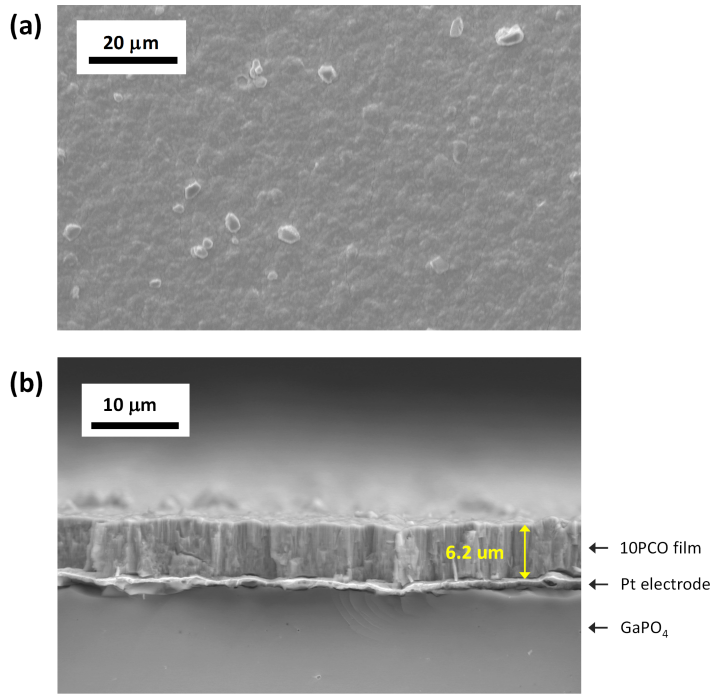

Figure 4.5: SEM micrographs of (a) the surface and (b) cross-section of the PCO film deposited on the $GaPO_4$ microbalance crystal with pure Pt electrode via PLD.

from the topographical analysis of the AFM image is 260 nm. Accordingly, the actual exposed 10PCO surface area is somewhat greater than the projected area; the difference between actual and projected area is 10.5%. As these surface area enhancement factors are relatively small in comparison to the typical range of k_{Chem} values encountered in the literature for any given material [114], no correction is made to account for this characteristic.

Relaxation studies were carried out at a temperature of 700 °C and selected oxygen partial pressures between 10^{-2} and and 10^{-4} atm (Figure 4.8).

The step change in oxygen partial pressure, $|\Delta \log(p\mathrm{O}_2 / \mathrm{atm})|$, was limited to values of 0.3 or less (or equivalently, a factor of 2 on the linear $p\mathrm{O}_2$ scale) to justify the assumption of a linear response and a fixed k_{Chem} over the relaxation conditions. At each oxygen partial pressure, 4 or 5 relaxation profiles were recorded. Both forward and reverse steps were evaluated at each pair of $p\mathrm{O}_2$ levels. The gas flow rate for all experiments was set to 200 sccm (standard cubic centimeter per minute), implying a gas-phase velocity of 0.02 m/s at the film. The supplied flow rates furthermore amount to gravimetric flow rates, normalized per unit mass of reactive

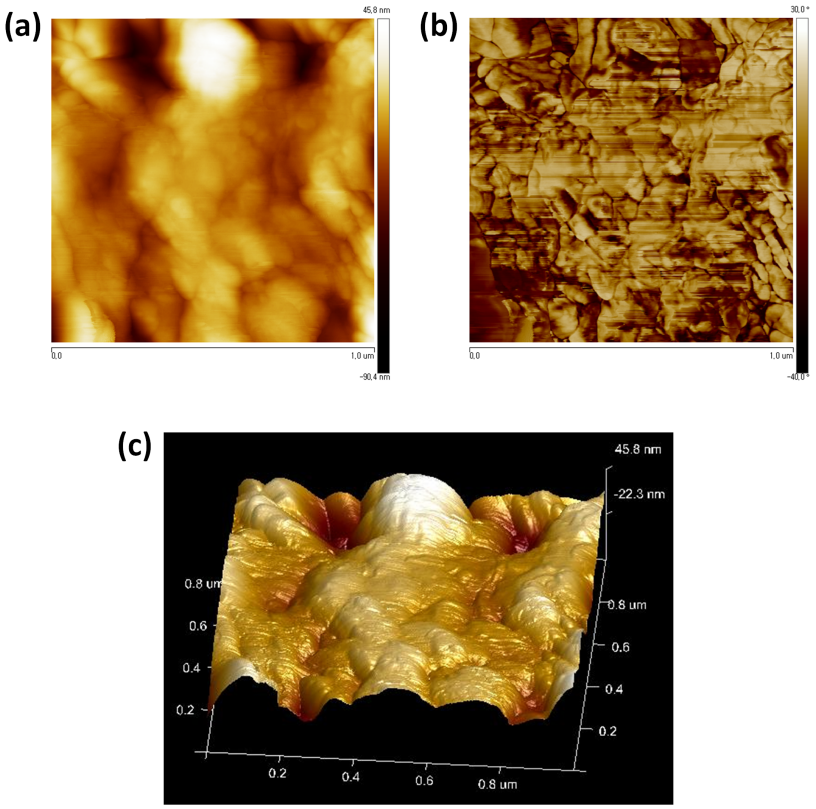

Figure 4.6: AFM topography of 10PCO film in (A) height-imaging mode, (b) phase-imaging mode, and (c) three-dimensional topography. Scanning area (*i.e.*, projected surface area): 400 μm2. Actual surface area: 442 μm2. RMS surface roughness: 260 nm

oxide, of 1.58×10^5 sccm/g. This flow rate is large enough to ensure that oxygen depletion/accumulation in the gas phase due to the change in film oxidation state does not impact the relaxation rate, as already discussed in chapter 3. Specifically, we estimate, based on the surface reaction constants reported below, that a gas flow rate of ~3 sccm would be sufficient to operate in the regime in which the gas-phase oxygen content is immune to oxygen release/uptake by the film, and hence the measurement accesses the surface reaction constant.

The overall both the frequency and oxygen profiles are presented in Figure 4.8. Figure 4.9 shows a typical set of raw relaxation profiles for four relaxation responses, *i.e.*, two reductions and two oxidations.

Several features are noteworthy. Overall, the behavior is highly reproducible. Second, the time scale for changing oxygen partial pressure within the reactor (~2

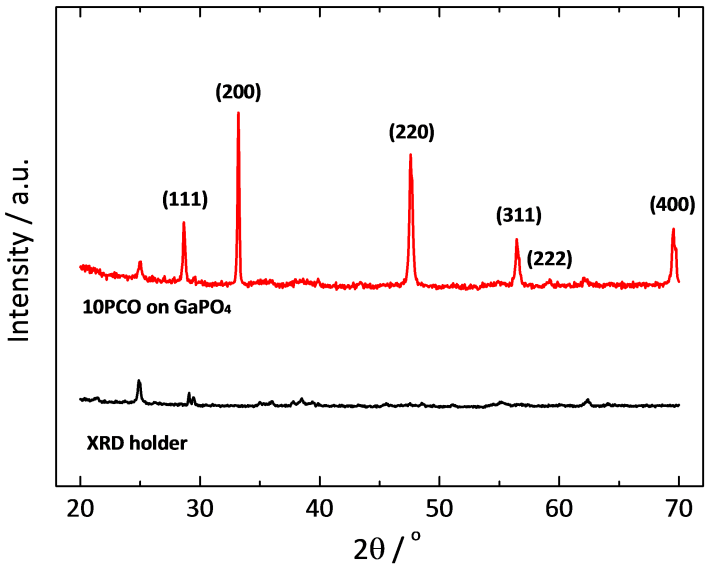

Figure 4.7: XRD patterns of 10PCO films with Pt electrodes after mass relaxation characterization. The XRD pattern of the XRD holder is displayed as a black line for reference.

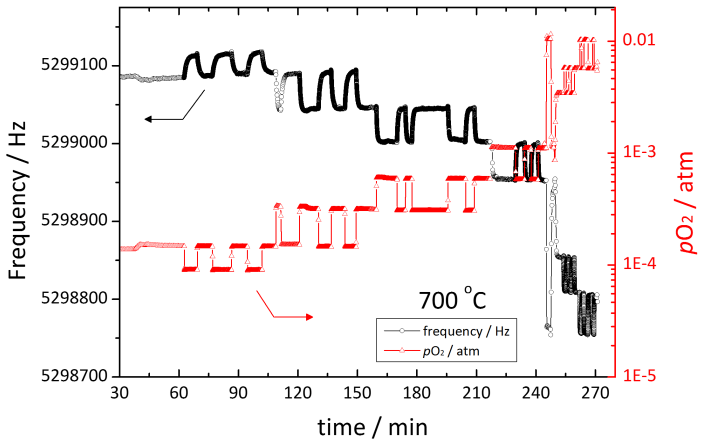

Figure 4.8: Long term frequency profile of the piezocrystal with 10PCO film (black) as well as the oxygen partial pressure (red) as a function of time, throughout the entire measurement campaign.

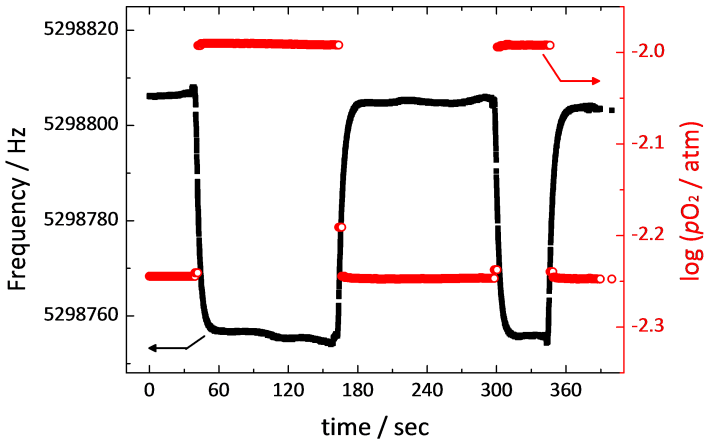

Figure 4.9: Crystal resonance frequency in Hz (left y-axis, black) and logarithmic pO_2 in atm (right y-axis, red) as a function of time throughout four relaxation studies, *i.e.*, two cycles of oxidation and subsequent reduction between oxygen partial pressures of 0.0102 and 0.0057 atm. Temperature: T = 700°C

seconds) is substantially shorter than the time scale of the material response (~20 seconds), indicating that the reactor characteristics are sufficient for measuring the material behavior. [78] Third, the frequency response shows no baseline drift. The normalized frequency relaxation profiles are well described by the exponential form given in Equation (4.2). The quality of the fit is evident in Figure 4.10, a representative case for the first oxidation change in Figure 4.9.

As reported in the inset table to Figure 4.10, the two k_{Chem} values for oxidation differ by less than 1%, and the k_{Chem} values for reduction differ by less than 3%. The R^2 values of all exponential fits (all the entire set of measurements) were larger than 0.998, implying the data are well described by the surface-limited solution to Fick's second law. The film is therefore thin enough that bulk diffusion contributions to the mass relaxation behavior are negligible. A slight but statistically significant asymmetry between the oxidation and reduction values of k_{Chem} is evident, with $k_{Chem}^{ox} > k_{Chem}^{red}$. Such asymmetry has received scattered attention in the literature. [80, 82] Understanding the precise origin of the phenomenon in the case of 10PCO awaits a future study, but it is likely related to the oxygen partial pressure dependence of k_{Chem} described below. Of relevance here is that the asymmetry is small enough that analysis of the relaxation behavior within the context of the linear approximation remains valid (as indicated by the large R^2 values).

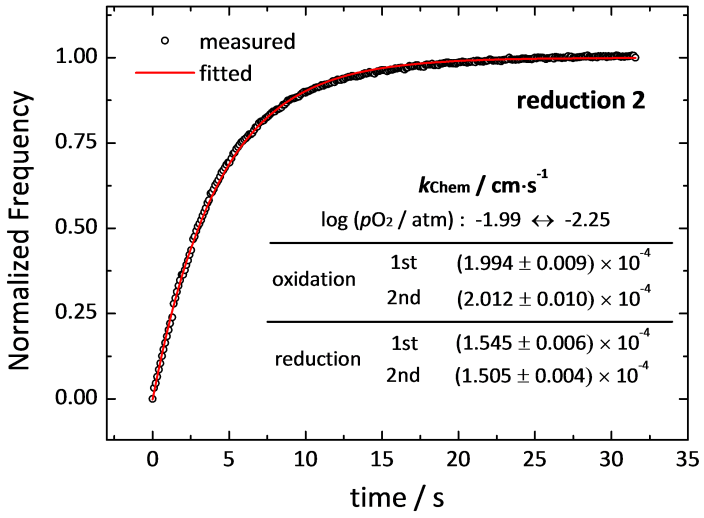

Figure 4.10: Normalized resonance frequency as a function of time, as well as fitted relaxation profile in the surface reaction limited case. Extracted value averaged over two reductions and oxidations, respectively: $k_{\mathrm{Chem}} = 1.76 \times 10^{-4}$ cm/s. Lower $p\mathrm{O}_2$ = 0.0057 atm; Higher $p\mathrm{O}_2$ = 0.0102 atm; Temperature: T = 700 °C. The inset table shows all extracted values of k_{Chem} for a swing between the indicated values of $p\mathrm{O}_2$. All R^2 values are > 0.998 for the respective fits

The complete set of surface reaction constants determined in this work is presented in Figure 4.11. The error bars shown in $p\mathrm{O}_2$ values reflect the span in oxygen partial pressure values between oxidizing and reducing conditions (with the average reported as the measurement pressure). The error bars in k_{Chem} values similarly reflect the span in surface reaction constant extracted from the oxidation and reduction perturbations. The measured k_{Chem} values obey a clear power law dependence on oxygen partial pressure, as evident from the linearity in the double-logarithmic plot. The power law exponents (m in $k_{\mathrm{Chem}} \propto (p\mathrm{O}_2)^{\mathrm{m}}$) are 0.69 ± 0.02. Moreover, the power law behavior holds over an oxygen partial pressure regime in which, as reported by Bishop *et al.*, [93] the concentration of the predominant negatively charged species, $[\mathrm{Pr'_{Ce}}]$, transitions at $p\mathrm{O}_2 \sim 10^{-3}$ atm from a fixed value, with $[\mathrm{Pr'_{Ce}}] = 2\left[V_{\mathrm{O}}^{\bullet\bullet}\right] \approx$ constant (below the transition $p\mathrm{O}_2$), to one that varies with oxygen partial pressure, with $[\mathrm{Pr'_{Ce}}] = 2\left[V_{\mathrm{O}}^{\bullet\bullet}\right] \propto p\mathrm{O}_2^{-1/6}$ (beyond the transition $p\mathrm{O}_2$). On increasing $p\mathrm{O}_2$ through this transition, the predominant positively charged defect species changes from oxygen vacancies to holes in the Pr impurity band. The surface reaction constant, as measured here, is apparently immune to these changes in defect chemistry.

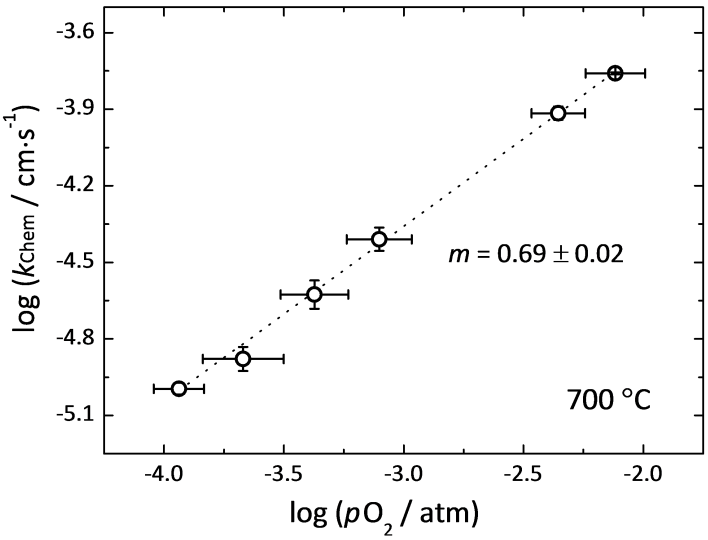

Figure 4.11: Surface reaction constants measured as a function of pO_2 (T = 700 °C). Straight line is a linear fit in the double-logarithmic scale (*i.e.*, power law fit) and number assigned with m is the power law slope.

The literature on the surface properties of PCO has been limited to date to electrochemical impedance measurements. Because this method yields a surface reaction constant which cannot be directly compared to the k_{Chem} obtained from a relaxation experiment, the present results cannot be readily validated against those from earlier studies. At a minimum, one must know the thermodynamic factor of oxygen, w_{O} ($\frac{d \ln a_{\mathrm{O}}}{d \ln c_{\mathrm{O}}}$, where a_{O} is activity and c_{O} is concentration of oxygen) in order to convert from surface reaction rate constant from impedance to k_{Chem}(relaxation). [19] In light of the complex defect chemistry of PCO [93] and the limited data collected in this work, such an analysis is not attempted here. Nevertheless, it is noteworthy that Chen *et al.* [111] have reported that k(impedance) in 10PCO increases with increasing partial pressure, in broad agreement with the present results. However, the behavior could not be described by a single power law exponent over the measured pO_2 range. The exponent was reported to change at 670 °C from 1.00 ± 0.04 to 0.33 ± 0.01 at an oxygen partial pressure of 10^{-3} atm, coinciding with the oxygen partial pressure at which the defect chemistry transitions. In addition to a likely influence of the thermodynamic factor in creating this difference between the behaviors of k(impedance) and k_{Chem}(relaxation), differences may also arise because those authors employed highly oriented and possibly epitaxial thin films grown on single-crystal yttria-stabilized zirconia (YSZ), whereas the present studies were performed using fine-grained polycrystalline PCO. A number of studies have revealed in recent

years that grain boundaries can play a decisive role in gas-solid reactions. [68–70] Furthermore, the surfaces in the two types of experiments (impedance spectroscopy and mass relaxation) may be very different as a consequence of application of a metal paste electrode in the former, whereas a bare surface is studied in the latter. [19] Differences in apparent rate constants can also result because surface defect concentrations, required in the conversion from interfacial conductance provided by impedance measurements to rate constant directly obtained from relaxation methods, [111] are uncertain.

While the results obtained here cannot be directly compared to previous studies of PCO, they can be viewed in the context of commonly studied p-type mixed ionic and electronic conductors of the perovskite structure, such as (La,Sr)CoO_3, [80] considered for cathode applications in solid oxide fuel cells. The k_{Chem} measured here for PCO falls within the general range of values observed for these materials. Moreover, a positive value of the power law exponent, m, is typical in these oxides, and values ranging from 0.14 to 0.82 have been reported under temperatures and oxygen partial pressure ranges similar to those of this work. [83] In undoped ceria, a rare example of an *n*-type conductor for which the surface reaction constant has been determined through a relaxation experiment, a value of 0.84 ± 0.02 has been measured at 1400 °C in chapter 3. Fleig *et al.* have presented a comprehensive analysis for connecting macroscopic measurements of the power law exponent to microscopic pathway.[86] Although the analysis was developed in the context of the more commonly studied *p*-type materials, it applies, in principle, also to oxides in which the electron carrier concentration exceeds the hole concentration (as in 10PCO). These authors have suggested that, when the hole concentration depends on oxygen partial pressure according to a 1/4 power law exponent, as is the case here, and the adsorbate coverage is low, as is typical of the high temperatures of the present experiments, a value of $m \cong 3/4$ results when reduction in diatomic oxygen from the superoxo ($O^{-}_{2,\mathrm{ad}}$) to the peroxo ($O^{2-}_{2,\mathrm{ad}}$) species is the rate-limiting step in oxygen incorporation from the gas into the solid phase. While it is premature to conclude that such a pathway definitively occurs in 10PCO, particularly in light of the potential role of surface-terminating grain boundaries, the experimental methodology outlined here enables further studies to fully elucidate the reaction mechanism.

4.5 Conclusions

In summary, we show that thin-film *mass* relaxation studies by detection of frequency response of gallium phosphate piezocrystals are feasible up to temperatures of 700 °C. The greatest challenge at this temperature is not the stability of the piezocrystal, but rather the stability of the metal electrodes, particularly under oxidizing (pO_2 > 10^{-4} atm) conditions. Measurements by this method up to the phase transition temperature of $GaPO_4$, 970 °C, are in principle possible. A key advantage of this mass relaxation system is not only its applicability towards the measurement of materials that change mass without changing other easily detected properties, such as conductivity, but also that the high sensitivity of the microbalance implies that only small samples are required. Consequently, the measurement chamber can also be made extremely small, ensuring rapid gas exchange and thus access to very rapid material processes. A potential disadvantage is that because materials to be studied must be deposited as films on metal electrodes that are, in turn, deposited on the gallium phosphate crystal, the oxide will in most cases be obtained in polycrystalline form, likely with small grain size. While a high grain boundary density in many cases enhances surface reaction rates, the inherent properties of boundary-free surfaces become difficult to characterize. The behavior of 10PCO revealed here by mass relaxation measurements is intriguing in that the rate constant appears insensitive to qualitative changes in the defect chemistry. The measured k_{Chem} varies between $\sim 1\times10^{-5}$ and $\sim 1.8\times10^{-4}$ cm/s at 700°C over the pO_2 range from 10^{-4} to 10^{-2} atm, with a law exponent of 0.69 ± 0.02. Some of this surprising behavior may be due to the nanocrystalline nature of the films, with grain size on the order of 60 nm. The methodology developed here lays the groundwork for future comprehensive studies of this and other materials. Moreover, the sensitivity of the gallium phosphate microbalance system has the potential to enable absolute measurements of oxygen nonstoichiometry in films of known thickness. The scatter in frequency response of 0.1 Hz corresponds to a scatter in mass of only 0.4 ng, suggesting accuracy in oxygen nonstoichiometry at the level of 10^{-5} for sufficiently thick (several μm) films.

Chapter 5

THE EFFECT OF MAGNITUDE OF DRIVING FORCE ON REDOX KINETICS

5.1 Introduction

The kinetic and mechanistic understandings of oxidation/reduction reactions in non-stoichiometric oxides are significantly helpful to design the reactive components for electrochemical and thermochemical energy related systems. In particular, for the thermochemical fuel production system, the reactive medium (usually ceria / doped ceria) experiences large oxygen nonstoichiometry changes along both reduction and oxidation. In chapter 4, we have showed the validity of the mass relaxation technique using piezocrystal microbalance. Unlike the conductivity/conductance relaxation method (chapter 2 and 3), the mass relaxation has the benefit in analysis of redox kinetics without the assumption of proximity to the equilibrium. Thus, we investigate the redox kinetics, especially the oxidation reaction of 10% Pr doped ceria via mass relaxation technique with respect to the magnitude of driving force, i.e. the size of ΔpO_2. To understand that kinetic behavior, firstly we have investigated the possible reaction mechanisms as well as rate determining steps, secondly the general reaction rate expressions have been derived, and lastly the most probable rate determining step has been suggested.

5.2 Experimentals

The all detail of the experimental system and the mass relaxation measurements under small driving force (*i.e.* sufficiently small change in pO_2, $|\Delta\log(pO_2 / \text{atm})| < 0.3$) for extracting k_{Chem} were described in chapter 4. Here, the relaxations towards oxidation under relatively large driving force, *i.e.* higher $|\Delta pO_2|$, were systematically measured with three different magnitudes in ΔpO_2 (small, medium, and large sizes) and different initial and final pO_2 values. More specifically, the initial and final values of pO_2 were controlled as i) different initial pO_2s to identical final pO_2, having small, moderate, and large magnitudes of ΔpO_2 and ii) identical initial pO_2

to different final $p\mathrm{O_2}$s, having also three magnitudes. The desired $p\mathrm{O_2}$ was obtained by employing gas mixture of $\mathrm{Ar/O_2}$ at the total flow rate of 200 sccm.

5.3 Results and Discussion

5.3.1 Redox kinetics with respect to the magnitude of driving force

The surface reaction rate constant (k_{Chem}) has been extensively investigated via relaxation methods. The relaxation of oxygen concentration in the oxide driven by a small oxygen partial pressure change of surrounding is tracked by measuring the mass of the oxide or by measuring the total electrical conductivity, as discussed in previous chapters. Here, we consider a case at which the surface reaction at the gas/oxide interface governs equilibration kinetics toward new equilibrium, more clearly, at which diffusion length of the oxide (thickness of the oxide film in this study) $\ll$ characteristic length ($D_{\mathrm{Chem}}/k_{\mathrm{Chem}}$). The very important experimental condition here is a sufficiently small perturbation in gas phase oxygen chemical potential (oxygen partial pressure), *i.e.* a sufficiently small driving force for redox reactions. It makes the following approximations valid: the surface reaction rate constant (k_{Chem}) is constant, and the oxygen flux across the surface of the oxide is in the linearity regime with respect to the oxygen concentration, thereby the first order correlation as below.

$$J_{\mathrm{O}} \approx k_{\mathrm{Chem}} \left(c_{\mathrm{O,eq}} - c_{\mathrm{O,S}} \right) \tag{5.1}$$

where $c_{\mathrm{O,eq}}$ is the oxygen concentration of the oxide at equilibrium with the gas phase, and $c_{\mathrm{O,S}}$ is the oxygen concentration just within the oxide surface(s). By combining with continuity relation, the oxygen concentration obeys the ordinary differential equation expressed in Eq. (5.2) with an already known initial condition, and its solution is expressed as an exponential decay function (Eq. (5.3)). The derivation is for the 1D case in which the thickness of sample is a and only one surface is exposed to the atmosphere, for example, the thin oxide film on substrate.

$$\frac{dc_{\mathrm{O}}(t)}{dt} = \frac{k_{\mathrm{Chem}}}{a} \left[c_{\mathrm{O}}(\infty) - c_{\mathrm{O}}(t) \right]; \quad c_{\mathrm{O}}(t)|_{t=0} = c_{\mathrm{O}}(0) \tag{5.2}$$

$$\frac{c_{\mathrm{O}}(t) - c_{\mathrm{O}}(0)}{c_{\mathrm{O}}(\infty) - c_{\mathrm{O}}(0)} = \frac{m(t) - m(0)}{m(\infty) - m(0)} \approx \frac{\sigma(t) - \sigma(0)}{\sigma(\infty) - \sigma(0)} = 1 - \exp\left(-\frac{k_{\mathrm{Chem}}}{a} t \right) \tag{5.3}$$

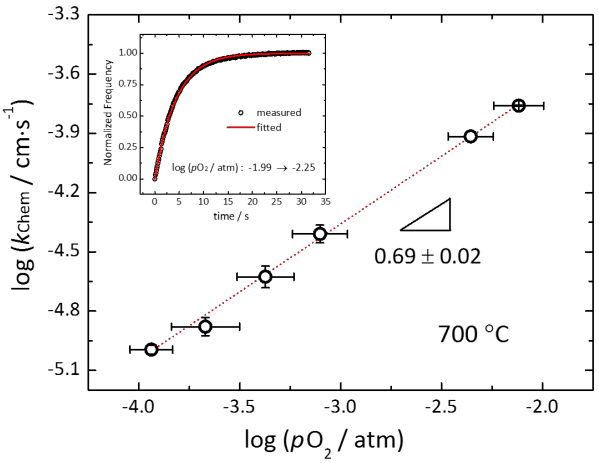

Figure 5.1: Surface reaction constants measured as a function of pO_2 (T = 700 °C). Straight line is a linear fit in the double-logarithmic scale (*i.e.*, power law fit) and number assigned with m is the power law slope.

As shown in Figure 5.1 (from chapter 4), k_{Chem} of 10PCO film at 700 °C has successfully extracted from the mass relaxation profiles which follow Eq. (5.3).

With increasing the magnitude of driving force of redox reaction, *i.e.* ΔpO_2 in this case, the linear correlation of oxygen flux with the oxygen concentration change (Eq. (5.1)) breaks down, therefore, the relaxation profile driven by this large ΔpO_2 cannot be explained by simple exponential decay function if the rate limiting step does not obey the first order reaction (Eq. (5.1)). This has been already pointed out by many researchers, [18, 52, 82] and Jacobson group actually showed the deviated kinetic behavior experimentally by conductivity relaxation methods. [56, 80] However, the experimental results according to the step size of pO_2 assessed by conductivity relaxation methods need to be carefully reconsidered. If the experimental result under large driving force is obtained by total electrical conductivity relaxation method for mixed ionic-electronic conducting (MIEC) oxides, *i.e.* if the total conductivity is a sum of both non-negligible ionic and electronic partial conductivities, or if the oxide contains transition metal and its effective charge affects the overall charge neutrality in the bulk of oxide, the assumption that the normalized conductivity is approximated to the normalized oxygen concentration as expressed in Eq. (5.3) is not valid. Therefore, it does not necessarily mean that Eq. (5.1) is not valid even though the linearity condition breaks down under large driving force, because it could be possible that the rate limiting step obeys the first order reaction.

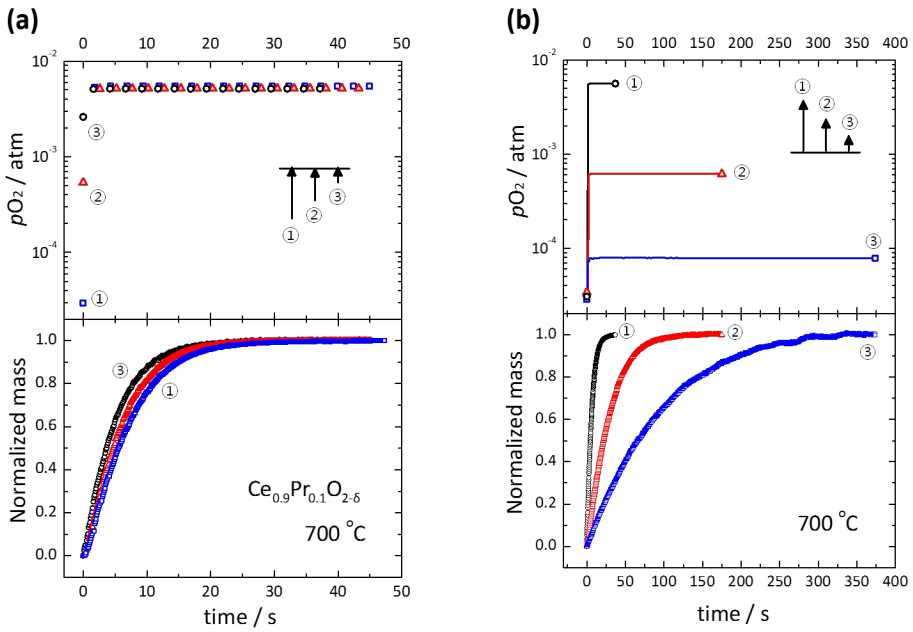

Figure 5.2: Mass relaxation profiles: (a) from different to the identical pO_2 and (b) from identical to the different pO_2.

In this study, we first exclude the effect of complicated correlation between normalized conductivity and oxygen concentration by directly observing the mass change which solely comes from the oxygen concentration change in the oxide. Then, we examine the relaxation results to confirm whether it obeys the first order reaction of the flux with the oxygen concentration.

As shown in Figure 5.2, the mass change under different ΔpO_2 conditions were measured via piezocrystal mass balance. The first set of measurements was from the different initial to the identical final pO_2 values (Figure 5.2(a)), and the second set was from the identical initial to the different final pO_2 values (Figure 5.2(b)). In the assumption that the rate determining step (RDS) obeys the first order reaction (Eq. (5.1)), two probable cases can be considered as shown in Figure 5.3(b): (i) k_{Chem} in Eq. (5.2) is determined by final pO_2 as a constant value which can be calculated from the correlation between k_{Chem} and pO_2 in Figure 5.1 or (ii) k_{Chem} is determined by the internal oxygen concentration at a time of t, $c_{\mathrm{O}}(t)$, which can be calculated from the mass of 10PCO. Even if the exact oxygen concentration of 10PCO film is not known, the oxygen concentration at a certain time of t can be calculated from the equilibrium oxygen concentration in bulk 10PCO reported by Bishop *et al.* [93] Based on the initial and final equilibrium oxygen concentration corresponding to

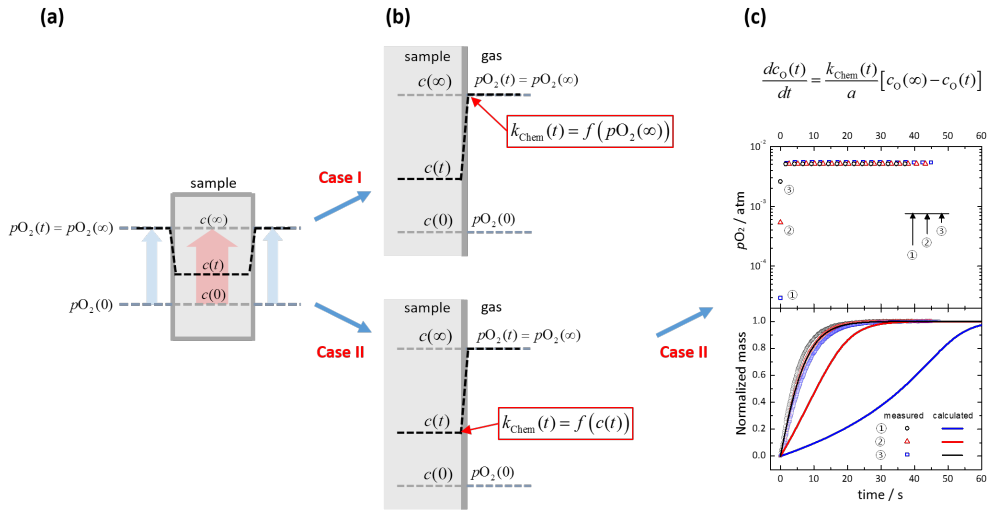

Figure 5.3: Schematic of oxygen concentration in bulk and pO_2 during redox reaction: (a) pO_2 and change and the oxygen concentration change at time of t. $c(0)$ and $c(\infty)$ are the values equilibrated at $pO_2(0)$ and $pO_2(\infty)$, respectively; (b) two plausible cases of how k_{Chem} is defined; and (c) mass relaxation profiles from experiments (symbols) and simulation (lines) in case II in (b).

the initial and final pO_2, respectively, the normalized mass profile can be directly converted to the absolute oxygen concentration profile. For the first case, the Eq. (5.2) can be solved to the Eq. (5.3) in the same manner with the case under small driving force, because k_{Chem} is fixed as the value at the final pO_2. Accordingly the normalized relaxation profiles should be the same if the final pO_2 is the same regardless of the initial pO_2. However, the experimental results in Figure 5.2(a) measured from different initials to the same final pO_2, show deviated relaxation profiles as the magnitude of ΔpO_2 changes, and thus the first case is not true. For the second case, we calculated the expected relaxation profiles by solving Eq. (5.2) (or the equation in Figure 5.2(c)) numerically. Here, we already know the initial value of c_O, and also know the k_{Chem} with respect to c_O from the correlations between the equilibrium c_O vs. pO_2 [93, 115] and between k_{Chem} vs. pO_2 (chapter 4); thus the full relaxation profiles of c_O are calculated by solving the ordinary differential equation (Eq. (5.2)) via 4^{th} order Runge-Kutta method (see Appendix). The calculated results in Figure 5.3(c) show large deviation from the experimental results, and the discrepancy gets bigger as ΔpO_2 change gets larger. Therefore, the RDS does not obey the first order reaction. Actually, the relaxation profile driven by large ΔpO_2 change was not well fitted to the simple exponential decay function, whereas the profile under small large ΔpO_2 change perfectly was (Fig. 5.4). It implies that the first order approximation

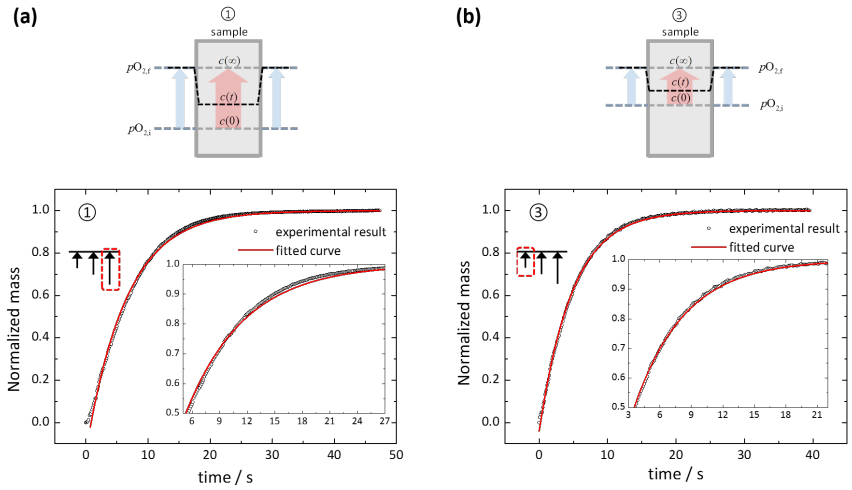

Figure 5.4: Normalized mass relaxation profiles and the fitted results to Eq. (5.3) under (a) large ΔpO_2 and (b) small ΔpO_2 conditions.

breaks down when ΔpO_2 change is large in this study.

There is one important report by Merkle and Maier which treated the relaxation profiles under large driving force by optical spectroscopy. [82] They assumed that one reaction step in the overall redox reaction is rate determining and the pre/post steps are in quasi-equilibrium state, and then derived the reaction rate of the probable rate determining step(s) from the simple chemical reaction expression. The detail of this approach was well explained in Maier's paper. [18] They aimed to understand the mechanism of redox kinetic process by using the method of initial rate, and hence used very initial part of relaxation profiles under large driving force. Despite they did not try to analyze the kinetics over the whole time, their approach which uses reaction rate expression for discrete reaction steps is a reasonable approach to adjust in our study.

5.3.2 Probable intermediates and mechanisms

The overall oxygen incorporation reaction is expressed as

$$O_2 + 2V_O^{\bullet\bullet} + 4e' = 2O_O^{\times} \tag{5.4}$$

It can be separated to the sequential discrete reaction steps accompanying the relevant intermediate species: adsorption of oxygen molecule on the oxide surface, charge

transfer of electronic species to the adsorbed, dissociation of oxygen molecule to the (charged) single oxygen, and incorporation with oxygen vacancy in the oxide. At oxide surfaces, O_2^- superoxide, [116, 117] O_2^{2-} peroxide, [118, 119] and O^- radicals [120–123] are the most frequently detected intermediates. However, their stability is expected to depend on the interaction with surface characteristics of the oxide, and the report for 10PCO system is quite sparse. Thus, we consider all possible cases for those three intermediates, respectively, and condense them into the five probable sequential mechanisms (Table 5.1). Regarding the first steps in each mechanism, it is not clear whether the oxygen adsorption sites at the surface should be addressed to be same with the oxygen vacancy of bulk ($V_O^{\bullet\bullet}$) by assuming the topmost surface as the extended of bulk, or should be accounted for just favorable sites due to the different bonding nature from the termination at the surface. Furthermore, the oxide is polycrystalline in this study, which implies that it consists of several different termination planes wherein the oxygen vacancy exists in different concentration. [124, 125] Therefore, we consider the two different cases: the oxygen vacancy is considered as i) one of point defects or ii) just the favorable adsorbed site, not as the point defect.

In Table 5.1, the reaction rates are expressed, where k_f and k_b are forward and backward reaction constants, respectively. Under the assumption that preceding and succeeding steps of single RDS are in quasi-equilibrium states, the concentration of the intermediate is converted to the combination of the concentrations of relatively well-defined species. In careful consideration of those reaction rate expressions, it is found that the reaction rate expression of RDS can be categorized into 9 cases according to what the preceding steps are as well as which point defect species (electron, oxygen vacancy) is incorporated in RDS. The case #3 corresponding to (IV-1), for example, indicates that the RDS is the incorporation of electron with adsorbed O_2, and the case #4 corresponding to (IV-2) and (IV-3) means that the RDS is whether i) the incorporation of electron with O_2^- followed by incorporation of electron with O_2 or ii) the dissociation of O_2^{2-} to two O^- species. Accordingly, instead of considering the specific reaction mechanisms described in Table 5.1 (in reference [126], they even introduced 22 possible reaction mechanisms composed of 66 discrete reaction steps), we will consider the generalized 9 reaction rate expressions in Table 5.2, which covers all possible scenario for an efficient study.

5.3.3 Reaction rate expression

The rate expression can be generalized as

$$R_{\mathrm{O}}(t) = \frac{dc_{\mathrm{O}}(t)}{dt} = A \cdot {pO_2}^{\omega}[V_{\mathrm{O}}^{\bullet\bullet}]^{\alpha} n^{\beta} - B \cdot [V_{\mathrm{O}}^{\bullet\bullet}]^{\alpha'} n^{\beta'} [\mathrm{O}_{\mathrm{O}}^{\times}]^{\gamma} \tag{5.5}$$

where ω, α, α', β, β', γ are the exponents of pO_2 and defect concentrations (listed in Table 5.2), and A and B are pre-factors for the forward and backward reactions. If all parameters in Eq. (5.5) are known, one can anticipate the oxygen concentration profiles over time. Thus, we consider how to determine pO_2, each defect concentration over time, and A, B constants.

First, the method of initial rate is applied to determine pO_2 and its exponent. As shown in Fig. 5.2, pO_2 is changed to the final pO_2 extremely fast, accordingly we assume that the pO_2 is constant as the final pO_2. The oxygen concentration is correlated with the mass of the oxide as below:

$$\begin{aligned} R_{\mathrm{O}}(t) &= \frac{dc_{\mathrm{O}}(t)}{dt} \\ &= (c_{\mathrm{O}}(0) - c_{\mathrm{O}}(\infty)) \cdot \frac{d\left(\frac{c_{\mathrm{O}}(t)-c_{\mathrm{O}}(\infty)}{c_{\mathrm{O}}(0)-c_{\mathrm{O}}(\infty)}\right)}{dt} \\ &\propto (m(0) - m(\infty)) \cdot \frac{d\,(\mathrm{normalizedmass})}{dt} \end{aligned} \tag{5.6}$$

For the oxidation reaction from the identical to the different final pO_2 values at the very initial of relaxations (near t $\approx$ 0), only forward reaction dominates the overall reaction, so that the reaction rate is expressed as

$$\begin{aligned} \log\left(R_{\mathrm{O}}|_{t\approx 0}\right) &= \log\left((m(0) - m(\infty)) \cdot \left.\frac{d\,(\mathrm{normalizedmass})}{dt}\right|_{t\approx 0}\right) + \mathrm{const.} \\ &\approx \log\left(A \cdot {pO_{2,f}}^{\omega}[V_{\mathrm{O}}^{\bullet\bullet}]_i^{\alpha} n_i^{\beta}\right) \\ &= \log\left(A \cdot [V_{\mathrm{O}}^{\bullet\bullet}]_i^{\alpha} n_i^{\beta}\right) + \omega \log pO_{2,f} \end{aligned} \tag{5.7}$$

where subscripts i and f indicate initial and final states. The $m(0)$ and $m(\infty)$ are obtained at the initial and final equilibrated states, and $\log\left(A \cdot [V_{\mathrm{O}}^{\bullet\bullet}]_i^{\alpha} n_i^{\beta}\right)$ is a constant because the oxygen vacancy and electron concentrations are fixed as the

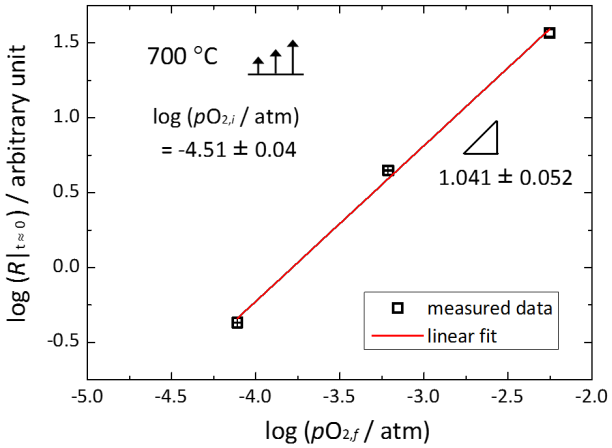

Figure 5.5: The correlation between reaction rate at the very initial and $pO_{2,f}$ from Eq. (5.8)

initial values due to their much slower change than pO_2. From the $pO_{2,f}$ dependence of reaction rate, the exponent of pO_2, ω, can be determined.

$$\frac{d\log\left(R_O|_{t\approx 0}\right)}{d\log pO_{2,f}} = \frac{d\log\left((m(0)-m(\infty))\cdot\left.\frac{d(\text{normalizedmass})}{dt}\right|_{t\approx 0}\right)}{d\log pO_{2,f}} = \omega \qquad (5.8)$$

Fig. 5.5 shows that the slope (ω) in (reaction rate at t $\approx$ 0) vs. ($pO_{2,f}$) is 1, and it means that the case #1-8 described in Table 5.2 are satisfactory to be RDS whereas #9 is not.

For the second parameter in Eq. (5.5), the defect concentrations, one needs to know the concentrations of oxygen vacancy, neutral oxygen, and electron as a function of pO_2 at 700 °C. Bishop *et al.* reported the equilibrium constants in 10PCO system at 700 °C, [93] thus by combining with i) charge neutrality condition and ii) mass/site conservation conditions, the concentrations can be calculated as shown in Fig. 5.6. The calculated results show good agreement with the experimentally obtained oxygen vacancy concentrations for bulk 10PCO by Bishop [93] and Davenport [115]. However, the defect concentrations at the surface layer are actually related to the surface reaction kinetics, and those are expected to differ from those in bulk. Furthermore, they are not easy to identify. At the surface or interface (*e.g.*, grain boundary), the difference in the free energies of formation of cation and anion vacancies lead to the formation of a surface electrical potential, associated with

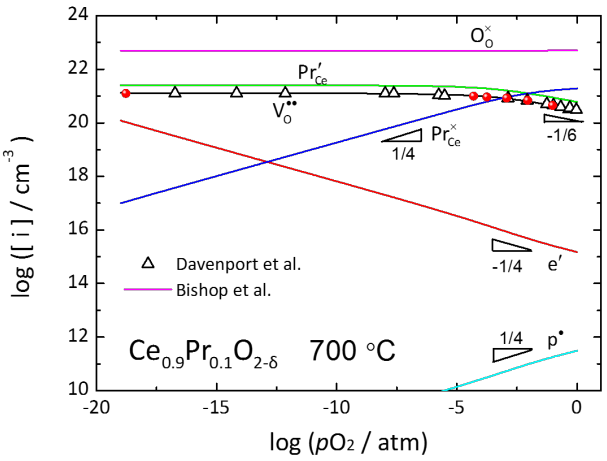

Figure 5.6: Defect concentrations in 10PCO as a function of $p\mathrm{O}_2$ at 700 °C

an excess of surface ionic charge. This space charge potential cuases the defect concentrations to deviate from those in the bulk. [127] For doped ceria system, it has been reported that the Mott-Schottky model where the dopant concentration does not vary along the position, *i.e.* the dopant concentration at surface is identical with that in bulk, was valid to explain the results of electrochemical study. [128–130] Thus, if we assume that our system obeys the Mott-Schottky model, the defect concentrations are expressed as [52]

$$
\begin{aligned}
&[\mathrm{Pr}_{\mathrm{Pr}}^{\times}]_s = [\mathrm{Pr}_{\mathrm{Pr}}^{\times}]_\infty \\
&quad \\
&\quad [\mathrm{Pr}'_{\mathrm{Pr}}]_s = [\mathrm{Pr}'_{\mathrm{Pr}}]_\infty \\
&[V_{\mathrm{O}}^{\bullet\bullet}]_s = [V_{\mathrm{O}}^{\bullet\bullet}]_\infty \cdot \exp\left(-\frac{2e\Delta\phi_s}{k_{\mathrm{B}}T}\right) \\
&[\mathrm{O}_{\mathrm{O}}^{\times}]_s = \left(2 - [V_{\mathrm{O}}^{\bullet\bullet}]_s\right) = \left(2 - [V_{\mathrm{O}}^{\bullet\bullet}]_\infty \cdot \exp\left(-\frac{2e\Delta\phi_s}{k_{\mathrm{B}}T}\right)\right) \approx [\mathrm{O}_{\mathrm{O}}^{\times}]_\infty \\
&n_s = n_\infty \cdot \exp\left(\frac{e\Delta\phi_s}{k_{\mathrm{B}}T}\right)
\end{aligned}
\tag{5.9}
$$

where subscripts s and ∞ indicate surface and bulk, respectively, and $\Delta\phi_s$ is the space charge potential at the surface relative to the bulk. If the space charge potential is independent of $p\mathrm{O}_2$, the reaction rate expression can be rewritten as below:

$$
\begin{aligned}
R_{\mathrm{O}}(t) &= A \cdot {p\mathrm{O}_2}^{\omega} [V_{\mathrm{O}}^{\bullet\bullet}]_s^{\alpha} n_s^{\beta} - B \cdot [V_{\mathrm{O}}^{\bullet\bullet}]_s^{\alpha'} n_s^{\beta'} [\mathrm{O}_{\mathrm{O}}^{\times}]_s^{\gamma} \\
&= A' \cdot {p\mathrm{O}_2}^{\omega} [V_{\mathrm{O}}^{\bullet\bullet}]_\infty^{\alpha} n_\infty^{\beta} - B' \cdot [V_{\mathrm{O}}^{\bullet\bullet}]_\infty^{\alpha'} n_\infty^{\beta'} [\mathrm{O}_{\mathrm{O}}^{\times}]_\infty^{\gamma}
\end{aligned}
\tag{5.10}
$$

where A' and B' are the pre-factors composed of equilibrium constants of preceding or succeeding steps and space charge potential related term. Since the terms relevant to the space charge potential are included in the pre-factors as a constant, the defect concentrations in bulk can be used.

Lastly, the remaining parameter, A' and B' pre-factors, will be calculated from the result of the equilibrium surface reaction rate constant (k_{Chem} following the correlation of $\log [k_{\mathrm{Chem}} / \mathrm{cm{\cdot}s^{-1}}] = 0.69 \times \log [p\mathrm{O_2} / \mathrm{atm}] - 2.30$). For conciseness, we first show how the reaction rate of model reaction A + B $\rightleftharpoons$ C + D can be simplified near the equilibrium condition. First, the reaction rate can be expressed as a function of the driving force (Λ).

$$\begin{aligned} R &= k_f[A][B] - k_b[C][D] \\ &= k \cdot e^{-\Delta G_f^{\mathrm{o}}/RT}[A][B] - k \cdot e^{-\Delta G_b^{\mathrm{o}}/RT}[C][D] \\ &= k \cdot e^{-\Delta G_f^{\mathrm{o}}/RT}[A][B]\left(1 - e^{(\Delta G_f^{\mathrm{o}} - \Delta G_b^{\mathrm{o}})/RT}\frac{[C][D]}{[A][B]}\right) \\ &= k \cdot e^{-\Delta G_f^{\mathrm{o}}/RT}[A][B]\left(1 - e^{\Delta G_{\mathrm{rxn}}^{\mathrm{o}}/RT}\frac{[C][D]}{[A][B]}\right) \\ &= k \cdot e^{-\Delta G_f^{\mathrm{o}}/RT}[A][B]\left(1 - e^{-\Lambda/RT}\right) \end{aligned} \tag{5.11}$$

where k is pre-exponential factor, ΔG_f^{o} and ΔG_b^{o} are the difference between Gibbs free energy of the reactant/product and the transition state along forward/backward directions, respectively, and $\Delta G_{rxn}^{\mathrm{o}}$ is ΔG_f^{o} - ΔG_b^{o}. It has been shown that 15-20% Sm, Gd, and Y doped ceria obey the ideal solution behavior. [131–133] Similarly if 10PCO system shows the ideal solution behavior, the driving force (Λ) is expressed as $-\Lambda = \Delta G_{\mathrm{rxn}}^{\mathrm{o}} + RT \ln \frac{[C][D]}{[A][A]}$, and thus the reaction rate is finally expressed as below:

$$R = k \cdot e^{-\Delta G_f^{\mathrm{o}}/RT}[A][B]\left(1 - e^{-\Lambda/RT}\right) \tag{5.12}$$

At equilibrium, the reaction rate as well as the driving force are zero, and thus

$$k_f[\widehat{A}][\widehat{B}] = k_b[\widehat{C}][\widehat{D}] = \sqrt{k_f k_b[\widehat{A}][\widehat{B}][\widehat{C}][\widehat{D}]} \tag{5.13}$$

$$\Lambda = 0 = \Delta G_{\mathrm{rxn,eq}}^{0} + RT \ln \frac{[\widehat{C}][\widehat{D}]}{[\widehat{A}][\widehat{B}]} \tag{5.14}$$

where the arc on the concentration terms indicates the equilibrium quantity. Thus, at near equilibrium, the driving force is

$$
\begin{aligned}
-\Lambda &= (\Delta G^0_{\text{rxn}} - \Delta G^0_{\text{rxn,eq}}) + RT \ln \frac{[C][D]/[\widehat{C}][\widehat{D}]}{[A][B]/[\widehat{A}][\widehat{B}]} \\
&\approx RT \ln \frac{[C][D]/[\widehat{C}][\widehat{D}]}{[A][B]/[\widehat{A}][\widehat{B}]}
\end{aligned}
\tag{5.15}
$$

and the reaction rate is

$$
R \approx R^0 \left(1 - \frac{[C][D]/[\widehat{C}][\widehat{D}]}{[A][B]/[\widehat{A}][\widehat{B}]}\right) \tag{5.16}
$$

where $R^0 = \sqrt{k_f k_b [\widehat{A}][\widehat{B}][\widehat{C}][\widehat{D}]}$.

Based on the derivation above, let us consider the case #2 in Table 5.2 as an example under small driving force.

$$
\begin{aligned}
R_{\text{O}} &= \frac{dc_{\text{O}}(t)}{dt} \\
&= A \cdot p\text{O}_2 [V_{\text{O}}^{\bullet\bullet}]^2 - B \cdot \frac{[\text{O}_{\text{O}}^{\times}]^2}{n^4} \\
&\approx \sqrt{AB} \frac{\sqrt{p\text{O}_{2,f}}[\widehat{V}_{\text{O}}^{\bullet\bullet}][\widehat{\text{O}}_{\text{O}}^{\times}]}{\widehat{n}^2} \cdot \left[1 - \frac{[\text{O}_{\text{O}}^{\times}]^2}{[\widehat{\text{O}}_{\text{O}}^{\times}]^2} \frac{[\widehat{V}_{\text{O}}^{\bullet\bullet}]^2}{[V_{\text{O}}^{\bullet\bullet}]^2} \frac{\widehat{n}^4}{n^4}\right]
\end{aligned}
\tag{5.17}
$$

For simplification, all defect concentrations are converted to the oxygen nonstoichiometry (δ) based on the following equations:

$$
\begin{aligned}
&\frac{[\text{V}_{\text{O}}^{\bullet\bullet}]}{[\widehat{\text{V}}_{\text{O}}^{\bullet\bullet}]} = \frac{\delta}{\delta_\infty}; \quad \frac{[\text{O}_{\text{O}}^{\times}]}{[\widehat{\text{O}}_{\text{O}}^{\times}]} = \frac{2-\delta}{2-\delta_\infty} \\
&\frac{n}{\widehat{n}} \approx \left(\frac{2\delta}{(0.1-2\delta)\,\text{K}_{\text{Pr}}}\right) \Big/ \left(\frac{2\delta_\infty}{(0.1-2\delta_\infty)\,\text{K}_{\text{Pr}}}\right) = \frac{\delta\,(0.1-2\delta_\infty)}{\delta_\infty\,(0.1-2\delta)}
\end{aligned}
\tag{5.18}
$$

from the defect equilibrium condition $\left(\frac{[\text{Pr}'_{\text{Ce}}]}{[\text{Pr}_{\text{Ce}}^{\times}]\text{n}} = \text{K}_{\text{Pr}}\right)$, the charge neutrality condition in the thermodynamic condition $\left([\text{Pr}'_{\text{Ce}}] \cong 2[\text{V}_{\text{O}}^{\bullet\bullet}]\right)$, and the mass balance condition $\left([\text{Pr}'_{\text{Ce}}] + [\,\text{Pr}_{\text{Ce}}^{\times}] = 0.1\right)$. Finally, the reaction rate is

$$
R_{\text{O}} \approx \sqrt{AB} \frac{\sqrt{p\text{O}_{2,f}}[\widehat{V}_{\text{O}}^{\bullet\bullet}][\widehat{\text{O}}_{\text{O}}^{\times}]}{\widehat{n}^2} \cdot \left[1 - \frac{{\delta_\infty}^6 (2-\delta)^2 (0.1-2\delta)^4}{\delta^6 (2-\delta_\infty)^2 (0.1-2\delta_\infty)^4}\right] \tag{5.19}
$$

In surface reaction limited regime, the k_{Chem} and reaction rate are correlated as Eq. (5.20) at specific oxygen nonstoichiometry (δ_∞) or specific $p\mathrm{O}_2$:

$$\frac{k_{\mathrm{Chem}}}{a} = \lim_{\delta \to \delta_\infty} \frac{R_{\mathrm{O}}}{\delta - \delta_\infty} \tag{5.20}$$

where a is a diffusion length, *i.e.* thickness of 10PCO in this study. Since the equilibrium defect concentrations (with arc) are already known at the specific $p\mathrm{O}_2$ where the δ is δ_∞, those values are constants.

$$k_{\mathrm{Chem}} = a\sqrt{AB}\frac{\sqrt{p\mathrm{O}_{2,f}}[\widehat{V}_{\mathrm{O}}^{\bullet\bullet}][\widehat{\mathrm{O}}_{\mathrm{O}}^{\times}]}{\widehat{n}^2} \cdot \lim_{\delta \to \delta_\infty}\left[1 - \frac{{\delta_\infty}^6(2-\delta)^2(0.1-2\delta)^4}{\delta^6(2-\delta_\infty)^2(0.1-2\delta_\infty)^4}\right] \tag{5.21}$$

In Eq. (5.21), all the concentrations are already known (Fig. 5.6), and the term in the limit function can be numerically calculated at the given δ_∞, which is determined by $p\mathrm{O}_{2,\mathrm{f}}$, and thus the value of $A{\times}B$ is obtained as a function of $p\mathrm{O}_2$. Furthermore, since the reaction rate is equal to zero at equilibrium state, A/B value is obtained as below:

$$R_{\mathrm{O}} = 0 = A \cdot p\mathrm{O}_{2,f}[\widehat{V}_{\mathrm{O}}^{\bullet\bullet}]^2 - B \cdot \frac{[\widehat{\mathrm{O}}_{\mathrm{O}}^{\times}]^2}{\widehat{n}^4} \tag{5.22}$$

$$\frac{A}{B} = \frac{[\widehat{\mathrm{O}}_{\mathrm{O}}^{\times}]^2}{p\mathrm{O}_{2,f}[\widehat{V}_{\mathrm{O}}^{\bullet\bullet}]^2\widehat{n}^4} \tag{5.23}$$

By solving the simultaneous equations relevant to $A{\times}B$ and A/B, the values of A and B are obtained, respectively.

5.3.4 Numerical simulation

The oxidation profiles for case #1-8 in Table 5.2 under small, medium, and large $p\mathrm{O}_2$ changes were computed solving the reaction rate equations numerically. The in-house Mathematica code was used to solve those ordinary differential equations (Table 5.2) in a stepwise manner via Runge-Kutta 4$^{\mathrm{th}}$ order method (see Appendix). Since this method is to find the numerical approximations to the solutions by calculating the slope, $\mathrm{d}c_{\mathrm{O}}/\mathrm{d}t$, the smaller step-size of t is preferable to find the true

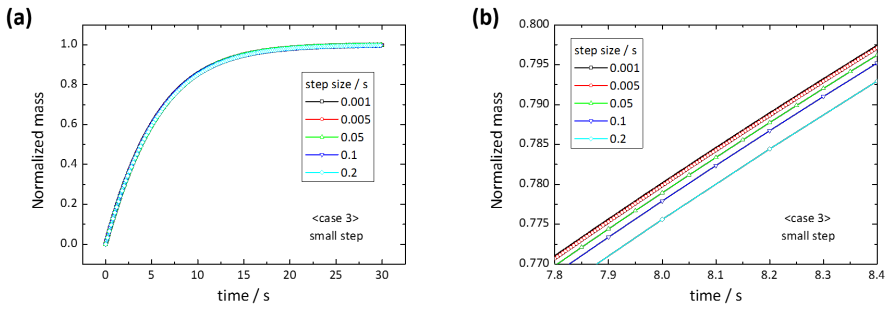

Figure 5.7: Mass relaxation profile from numerical calculation with respect to step size of time for case #3 under small pO_2 change.

solution. Therefore, the convergence with respect to the step-size was always checked for all cases. As an example, for case #3 under small pO_2 change, the numerical solution was converged to where the step size was less than 0.005 sec (Fig. 5.7). Fig. 5.8 shows the deviation between the computed and the experimental profiles as a function of time. In consideration of all results with respect to the experimental conditions in ΔpO_2, the reaction step of case #3 corresponding to the reduction of diatomic oxygen from neutral oxygen molecule to superoxide is expected to the most probable RDS. The relaxation profiles of case #3 (Fig. 5.9) from calculation and experiments show good agreement (for the other cases, please see the supplementary information). This result implies that if one knows RDS step, correlation between equilibrium k_{Chem} and pO_2, and defect concentrations, then the redox kinetic behavior can be anticipated.

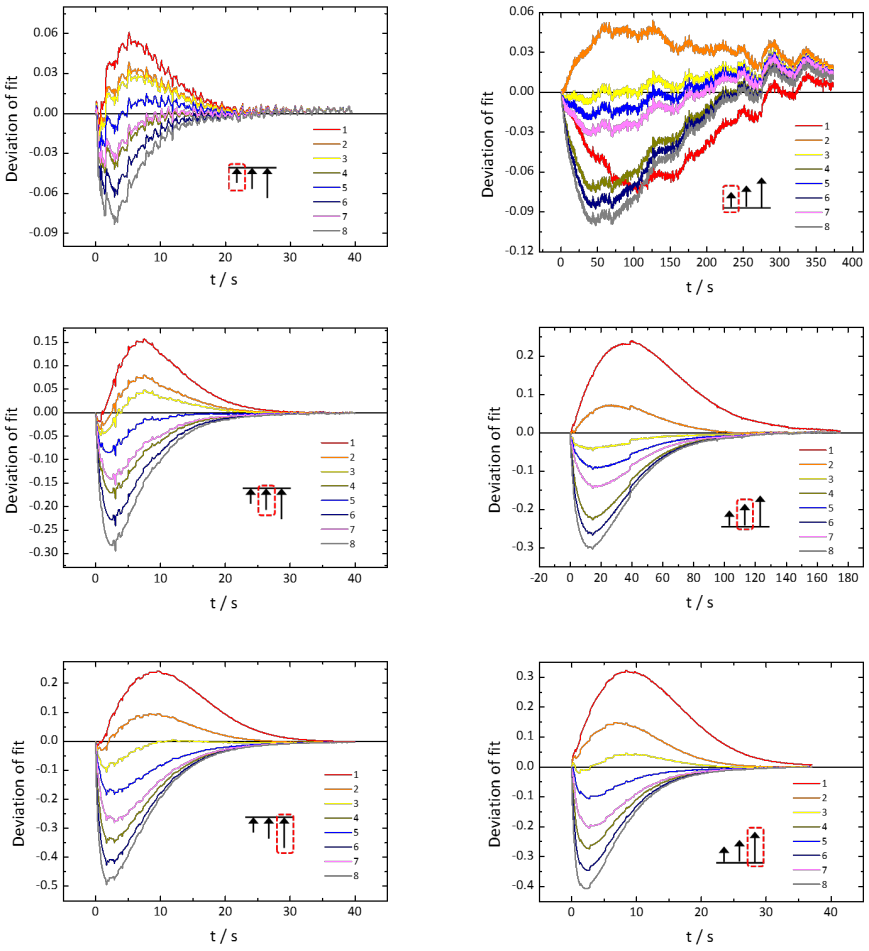

Figure 5.8: Derivation of the computed result from the experimental result as a function of time for all cases. The experimental condition is described in the plot (the marked arrow).

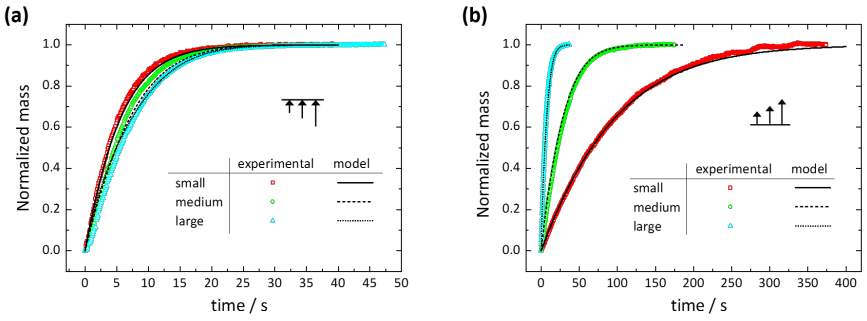

Figure 5.9: Comparison of computed result based on model case #3 with the experimental results: the pO_2 conditions are (a) from different to the same condition and (b) from same to the different conditions.

5.4 Conclusions

Relaxation behavior of oxygen concentration within oxides under large driving force (large ΔpO_2) in material-kinetic limit, especially in surface reaction limit, is a result of convolution of surface reaction rate constants and rate determining step (RDS) of oxidation reaction. From the comparison between relaxation profiles from experiments and from calculation based on the reaction rate expression, the most probable RDS can be determined. In this study for 10% Pr doped ceria at 700 °C, the reduction of diatomic oxygen from neutral oxygen molecule to superoxide is the probable RDS in oxidation reaction, and from this finding, we have successfully explained the oxidation kinetics under large driving force.

Table 5.1: Possible reaction mechanisms

Case I.

$O_2 + V_O^{\bullet\bullet} \leftrightarrow (O_2 \cdots V_O^{\bullet\bullet})$	
$R_O = 2R_{O_2} = 2k_f \cdot pO_2[V_O^{\bullet\bullet}] - 2k_b \cdot [(O_2 \cdots V_O^{\bullet\bullet})]$ $= 2k_f \cdot pO_2[V_O^{\bullet\bullet}] - 2\frac{k_b}{K_2 {K_3}^2} \cdot \frac{[O_O^\times]^2}{[V_O^{\bullet\bullet}]n^4}$	$K_1 = \frac{[(O_2 \cdots V_O^{\bullet\bullet})]}{pO_2[V_O^{\bullet\bullet}]}$
$(O_2 \cdots V_O^{\bullet\bullet}) + V_O^{\bullet\bullet} \leftrightarrow 2(O \cdots V_O^{\bullet\bullet})$	
$R_O = 2R_{O_2} = 2k_f \cdot [(O_2 \cdots V_O^{\bullet\bullet})][V_O^{\bullet\bullet}] - 2k_b \cdot [(O \cdots V_O^{\bullet\bullet})]^2$ $= 2k_f K_1 \cdot pO_2[V_O^{\bullet\bullet}]^2 - 2\frac{k_b}{{K_3}^2} \cdot \frac{[O_O^\times]^2}{n^4}$	$K_2 = \frac{[(O \cdots V_O^{\bullet\bullet})]^2}{[(O_2 \cdots V_O^{\bullet\bullet})][V_O^{\bullet\bullet}]}$
$(O \cdots V_O^{\bullet\bullet}) + 2e' \leftrightarrow O_O^\times$	
$R_O = k_f \cdot [(O \cdots V_O^{\bullet\bullet})]n^2 - k_b \cdot [O_O^\times]$ $= k_f \sqrt{K_1 K_2} \cdot n^2 [V_O^{\bullet\bullet}] \sqrt{pO_2} - k_b \cdot [O_O^\times]$	$K_3 = \frac{[O_O^\times]}{[(O \cdots V_O^{\bullet\bullet})]n^2}$

Case II.

$O_2 + V_O^{\bullet\bullet} \leftrightarrow (O_2 \cdots V_O^{\bullet\bullet})$	
$R_O = 2R_{O_2} = 2k_f \cdot pO_2[V_O^{\bullet\bullet}] - 2k_b \cdot [(O_2 \cdots V_O^{\bullet\bullet})]$ $= 2k_f \cdot pO_2[V_O^{\bullet\bullet}] - 2\frac{k_b}{K_2 {K_3}^2} \cdot \frac{[O_O^\times]^2}{[V_O^{\bullet\bullet}]n^4}$	$K_1 = \frac{[(O_2 \cdots V_O^{\bullet\bullet})]}{pO_2[V_O^{\bullet\bullet}]}$
$(O_2 \cdots V_O^{\bullet\bullet}) + V_O^{\bullet\bullet} + 2e' \leftrightarrow 2(O^- \cdots V_O^{\bullet\bullet})$	
$R_O = 2R_{O_2} = 2k_f \cdot [(O_2 \cdots V_O^{\bullet\bullet})][V_O^{\bullet\bullet}]n^2 - 2k_b \cdot [(O^- \cdots V_O^{\bullet\bullet})]^2$ $= 2k_f K_1 \cdot pO_2[V_O^{\bullet\bullet}]^2 n^2 - 2\frac{k_b}{{K_3}^2} \cdot \frac{[O_O^\times]^2}{n^2}$	$K_2 = \frac{[(O^- \cdots V_O^{\bullet\bullet})]^2}{[(O_2 \cdots V_O^{\bullet\bullet})][V_O^{\bullet\bullet}]n^2}$
$(O^- \cdots V_O^{\bullet\bullet}) + e' \leftrightarrow O_O^\times$	
$R_O = k_f \cdot [(O^- \cdots V_O^{\bullet\bullet})]n - k_b \cdot [O_O^\times]$ $= k_f \sqrt{K_1 K_2} \cdot n^2 [V_O^{\bullet\bullet}] \sqrt{pO_2} - k_b \cdot [O_O^\times]$	$K_3 = \frac{[O_O^\times]}{[(O^- \cdots V_O^{\bullet\bullet})]n}$

Case III.

$O_2 + V_O^{\bullet\bullet} + e' \leftrightarrow (O_2^- \cdots V_O^{\bullet\bullet})$	
$R_O = 2R_{O_2} = 2k_f \cdot pO_2[V_O^{\bullet\bullet}]n - 2k_b \cdot [(O_2^- \cdots V_O^{\bullet\bullet})]$ $= 2k_f \cdot pO_2[V_O^{\bullet\bullet}]n - 2\frac{k_b}{{K_2K_3}^2} \cdot \frac{[O_O^\times]^2}{[V_O^{\bullet\bullet}]n^3}$	$K_1 = \frac{[(O_2^- \cdots V_O^{\bullet\bullet})]}{pO_2[V_O^{\bullet\bullet}]n}$
$(O_2^- \cdots V_O^{\bullet\bullet}) + V_O^{\bullet\bullet} + e' \leftrightarrow 2(O^- \cdots V_O^{\bullet\bullet})$	
$R_O = 2R_{O_2} = 2k_f \cdot [(O_2^- \cdots V_O^{\bullet\bullet})][V_O^{\bullet\bullet}]n - 2k_b \cdot [(O^- \cdots V_O^{\bullet\bullet})]^2$ $= 2k_fK_1 \cdot pO_2[V_O^{\bullet\bullet}]^2n^2 - 2\frac{k_b}{{K_3}^2} \cdot \frac{[O_O^\times]^2}{n^2}$	$K_2 = \frac{[(O^- \cdots V_O^{\bullet\bullet})]^2}{[(O_2^- \cdots V_O^{\bullet\bullet})][V_O^{\bullet\bullet}]n}$
$(O^- \cdots V_O^{\bullet\bullet}) + e' \leftrightarrow O_O^\times$	
$R_O = k_f \cdot [(O^- \cdots V_O^{\bullet\bullet})]n - k_b \cdot [O_O^\times]$ $= k_f\sqrt{K_1K_2} \cdot n^2[V_O^{\bullet\bullet}]\sqrt{pO_2} - k_b \cdot [O_O^\times]$	$K_3 = \frac{[O_O^\times]}{[(O^- \cdots V_O^{\bullet\bullet})]n}$

Case IV.

$O_2 + e' \leftrightarrow O_2^-$	
$R_O = 2R_{O_2} = 2k_f \cdot pO_2n - 2k_b \cdot [O_2^-]$ $= 2k_f \cdot pO_2n - 2\frac{k_b}{K_2K_3{K_4}^2} \cdot \frac{[O_O^\times]^2}{[V_O^{\bullet\bullet}]^2n^3}$	$K_1 = \frac{[O_2^-]}{pO_2n}$
$O_2^- + e' \leftrightarrow O_2^{2-}$	
$R_O = 2R_{O_2} = 2k_f \cdot [O_2^-]n - 2k_b \cdot [O_2^{2-}]$ $= 2k_fK_1 \cdot pO_2n^2 - 2\frac{k_b}{K_3{K_4}^2} \cdot \frac{[O_O^\times]^2}{[V_O^{\bullet\bullet}]^2n^2}$	$K_2 = \frac{[O_2^{2-}]}{[O_2^-]n}$
$O_2^{2-} \leftrightarrow 2O^-$	
$R_O = 2R_{O_2} = 2k_f \cdot [O_2^{2-}] - 2k_b \cdot [O^-]^2$ $= 2k_fK_1K_2 \cdot pO_2n^2 - 2\frac{k_b}{{K_4}^2} \cdot \frac{[O_O^\times]^2}{[V_O^{\bullet\bullet}]^2n^2}$	$K_3 = \frac{[O^-]^2}{[O_2^{2-}]}$
$O^- + V_O^{\bullet\bullet} + e' \leftrightarrow O_O^\times$	
$R_O = k_f \cdot [O^-][V_O^{\bullet\bullet}]n - k_b \cdot [O_O^\times]$ $= k_f\sqrt{K_1K_2K_3} \cdot n^2[V_O^{\bullet\bullet}]\sqrt{pO_2} - k_b \cdot [O_O^\times]$	$K_4 = \frac{[O_O^\times]}{[O^-][V_O^{\bullet\bullet}]n}$

Case V.

$\mathrm{O_2} + V_{\mathrm{O}}^{\bullet\bullet} \leftrightarrow (\mathrm{O_2}\cdots V_{\mathrm{O}}^{\bullet\bullet})$	
$R_{\mathrm{O}} = 2R_{\mathrm{O_2}} = 2k_f \cdot p\mathrm{O_2}[V_{\mathrm{O}}^{\bullet\bullet}] - 2k_b \cdot [(\mathrm{O_2}\cdots V_{\mathrm{O}}^{\bullet\bullet})]$ $= 2k_f \cdot p\mathrm{O_2}[V_{\mathrm{O}}^{\bullet\bullet}] - 2\frac{k_b}{{K_2K_3K_4K_5}^2}\frac{[\mathrm{O_O^\times}]^2}{[V_{\mathrm{O}}^{\bullet\bullet}]n^4}$	$\mathrm{K_1} = \frac{[(\mathrm{O_2}\cdots V_{\mathrm{O}}^{\bullet\bullet})]}{p\mathrm{O_2}[V_{\mathrm{O}}^{\bullet\bullet}]}$
$(\mathrm{O_2}\cdots V_{\mathrm{O}}^{\bullet\bullet}) + e' \leftrightarrow (\mathrm{O_2}\cdots V_{\mathrm{O}}^{\bullet\bullet})^-$	
$R_{\mathrm{O}} = 2R_{\mathrm{O_2}} = 2k_f \cdot [(\mathrm{O_2}\cdots V_{\mathrm{O}}^{\bullet\bullet})]n - 2k_b \cdot [(\mathrm{O_2}\cdots V_{\mathrm{O}}^{\bullet\bullet})^-]$ $= 2k_fK_1 \cdot p\mathrm{O_2}[V_{\mathrm{O}}^{\bullet\bullet}]n - 2\frac{k_b}{{K_3K_4K_5}^2}\cdot\frac{[\mathrm{O_O^\times}]^2}{[V_{\mathrm{O}}^{\bullet\bullet}]n^3}$	$\mathrm{K_2} = \frac{[(\mathrm{O_2}\cdots V_{\mathrm{O}}^{\bullet\bullet})^-]}{[(\mathrm{O_2}\cdots V_{\mathrm{O}}^{\bullet\bullet})]n}$
$(\mathrm{O_2}\cdots V_{\mathrm{O}}^{\bullet\bullet})^- + e' \leftrightarrow (\mathrm{O_2}\cdots V_{\mathrm{O}}^{\bullet\bullet})^{2-}$	
$R_{\mathrm{O}} = 2R_{\mathrm{O_2}} = 2k_f \cdot [(\mathrm{O_2}\cdots V_{\mathrm{O}}^{\bullet\bullet})^-]n - 2k_b \cdot [(\mathrm{O_2}\cdots V_{\mathrm{O}}^{\bullet\bullet})^{2-}]$ $= 2k_fK_1K_2p\mathrm{O_2}[V_{\mathrm{O}}^{\bullet\bullet}]n^2 - 2\frac{k_b}{K_4{K_5}^2}\frac{[\mathrm{O_O^\times}]^2}{[V_{\mathrm{O}}^{\bullet\bullet}]n^2}$	$\mathrm{K_3} = \frac{[(\mathrm{O_2}\cdots V_{\mathrm{O}}^{\bullet\bullet})^{2-}]}{[(\mathrm{O_2}\cdots V_{\mathrm{O}}^{\bullet\bullet})^-]n}$
$(\mathrm{O_2}\cdots V_{\mathrm{O}}^{\bullet\bullet})^{2-} + V_{\mathrm{O}}^{\bullet\bullet} \leftrightarrow 2(\mathrm{O}^-\cdots V_{\mathrm{O}}^{\bullet\bullet})$	
$R_{\mathrm{O}} = 2R_{\mathrm{O_2}} = 2k_f \cdot [(\mathrm{O_2}\cdots V_{\mathrm{O}}^{\bullet\bullet})^{2-}][V_{\mathrm{O}}^{\bullet\bullet}] - 2k_b \cdot [(\mathrm{O}^-\cdots V_{\mathrm{O}}^{\bullet\bullet})]^2$ $= 2k_fK_1K_2K_3p\mathrm{O_2}[V_{\mathrm{O}}^{\bullet\bullet}]^2n^2 - 2\frac{k_b}{{K_5}^2}\cdot\frac{[\mathrm{O_O^\times}]^2}{n^2}$	$\mathrm{K_4} = \frac{[(\mathrm{O}^-\cdots V_{\mathrm{O}}^{\bullet\bullet})]^2}{[(\mathrm{O_2}\cdots V_{\mathrm{O}}^{\bullet\bullet})^{2-}][V_{\mathrm{O}}^{\bullet\bullet}]}$
$(\mathrm{O}^-\cdots V_{\mathrm{O}}^{\bullet\bullet}) + e' \leftrightarrow \mathrm{O_O^\times}$	
$R_{\mathrm{O}} = k_f \cdot [(\mathrm{O}^-\cdots V_{\mathrm{O}}^{\bullet\bullet})]n - k_b \cdot [\mathrm{O_O^\times}]$ $= k_f\sqrt{K_1K_2K_3K_4}\cdot n^2[V_{\mathrm{O}}^{\bullet\bullet}]\sqrt{p\mathrm{O_2}} - k_b \cdot [\mathrm{O_O^\times}]$	$\mathrm{K_5} = \frac{[\mathrm{O_O^\times}]}{[(\mathrm{O}^-\cdots V_{\mathrm{O}}^{\bullet\bullet})]n}$

Table 5.2: Generalized expression of reaction rates and its relevant rate determining step(s).

#	Reaction rate	Relevant RDS
1	$R_O = A \cdot pO_2[V_O^{\bullet\bullet}] - B\frac{[O_O^\times]^2}{[V_O^{\bullet\bullet}]n^4}$	(I-1, II-1, V-1)
2	$R_O = A \cdot pO_2[V_O^{\bullet\bullet}]^2 - B \cdot \frac{[O_O^\times]^2}{n^4}$	(I-2)
3	$R_O = A \cdot pO_2 n - B \cdot \frac{[O_O^\times]^2}{[V_O^{\bullet\bullet}]^2 n^3}$	(IV-1)
4	$R_O = A \cdot pO_2 n^2 - B \cdot \frac{[O_O^\times]^2}{[V_O^{\bullet\bullet}]^2 n^2}$	(IV-2, IV-3)
5	$R_O = A \cdot pO_2[V_O^{\bullet\bullet}]n - B \cdot \frac{[O_O^\times]^2}{[V_O^{\bullet\bullet}]n^3}$	(III-1, V-2)
6	$R_O = A \cdot pO_2[V_O^{\bullet\bullet}]n^2 - B \cdot \frac{[O_O^\times]^2}{[V_O^{\bullet\bullet}]n^2}$	(V-3)
7	$R_O = A \cdot pO_2[V_O^{\bullet\bullet}]^2 n - B \cdot \frac{[O_O^\times]^2}{n^3}$	(none)
8	$R_O = A \cdot pO_2[V_O^{\bullet\bullet}]^2 n^2 - B \cdot \frac{[O_O^\times]^2}{n^2}$	(II-2, III-2, V-4)
9	$R_O = A \cdot n^2[V_O^{\bullet\bullet}]\sqrt{pO_2} - B \cdot [O_O^\times]$	(All the final steps, I-3, II-3, III-3, IV-4, V-5)

Supplemental Information of Ch.5

Bulk defect chemistry of $Pr_{0.1}Ce_{0.9}O_{2-\delta}$

Defect chemistry of bulk 10PCO is well established by Bishop *et al.* [93] In the high pO_2 range ($pO_2 > 10^{-5}$ atm) treated in this study, the following defect reactions with equilibrium constants, charge neutrality, mass and site conservation conditions are valid.

$$Pr_{Ce}^{\times} + e' \leftrightarrow Pr'_{Ce} : \quad \frac{[Pr'_{Ce}]}{[Pr_{Ce}^{\times}]n} = K_{Pr}$$

$$nil \leftrightarrow e' + p^{\bullet} : \quad np = K_e$$

$$O_O^{\times} \leftrightarrow V_O^{\bullet\bullet} + 2e' + \tfrac{1}{2}O_2 : \quad \frac{[V_O^{\bullet\bullet}]n^2 pO_2{}^{1/2}}{[O_O^{\times}]} = K_{red}$$

$$[Pr'_{Ce}] + [Pr_{Ce}^{\times}] = 0.1[Ce_{0.9}Pr_{0.1}O_{2-\delta}]$$

$$[V_O^{\bullet\bullet}] + [O_O^{\times}] = 2[Ce_{0.9}Pr_{0.1}O_{2-\delta}]$$

$$[Pr'_{Ce}] \cong 2[V_O^{\bullet\bullet}]$$

From all the parameters of defect equilibria at 700 °C reported in ref. [93], defect concentrations are calculated as a function of pO_2.

Computed relaxation profiles

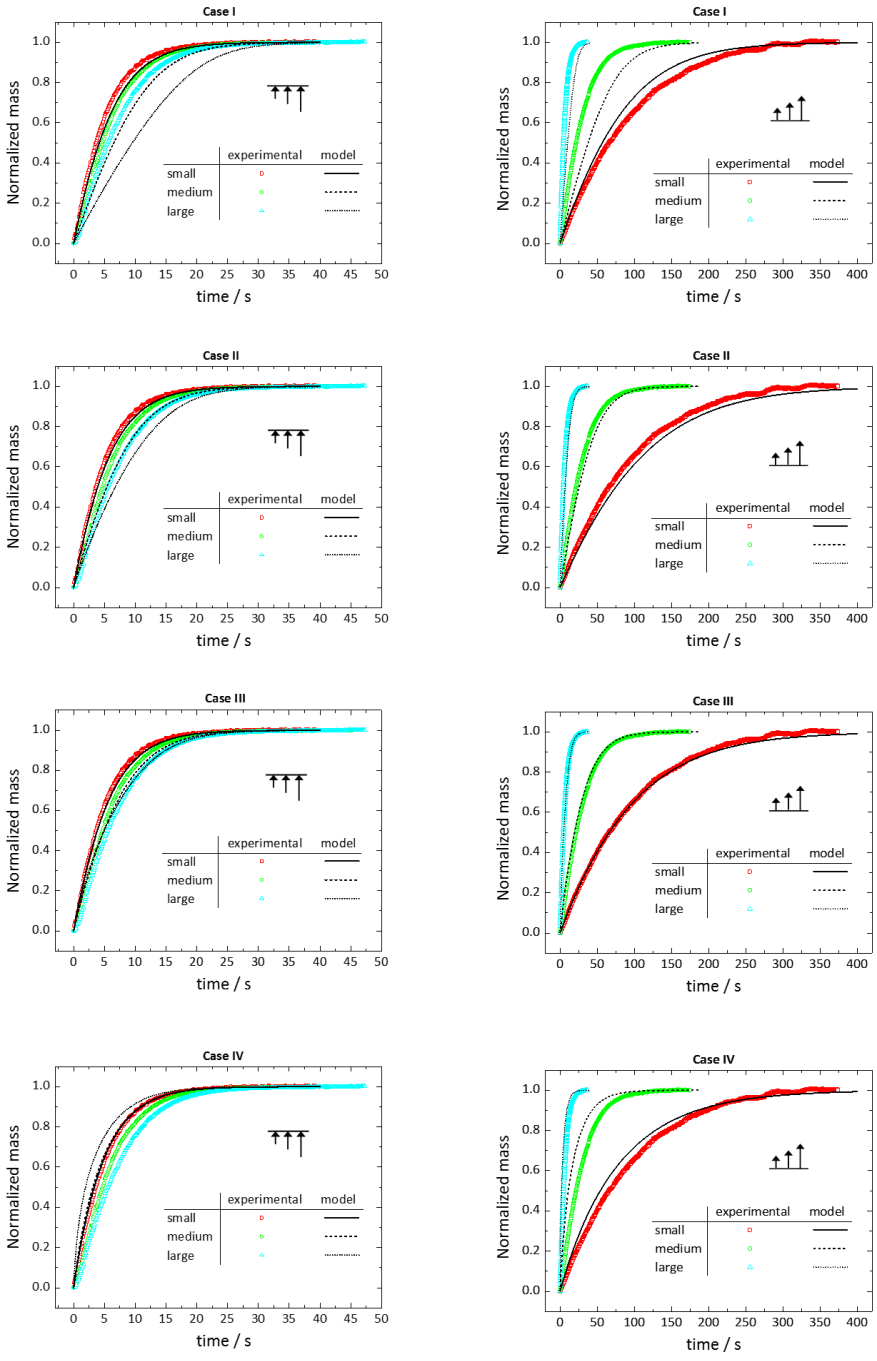

Figure 5.10: Computed and experimental mass relaxation profiles for case #1-8.

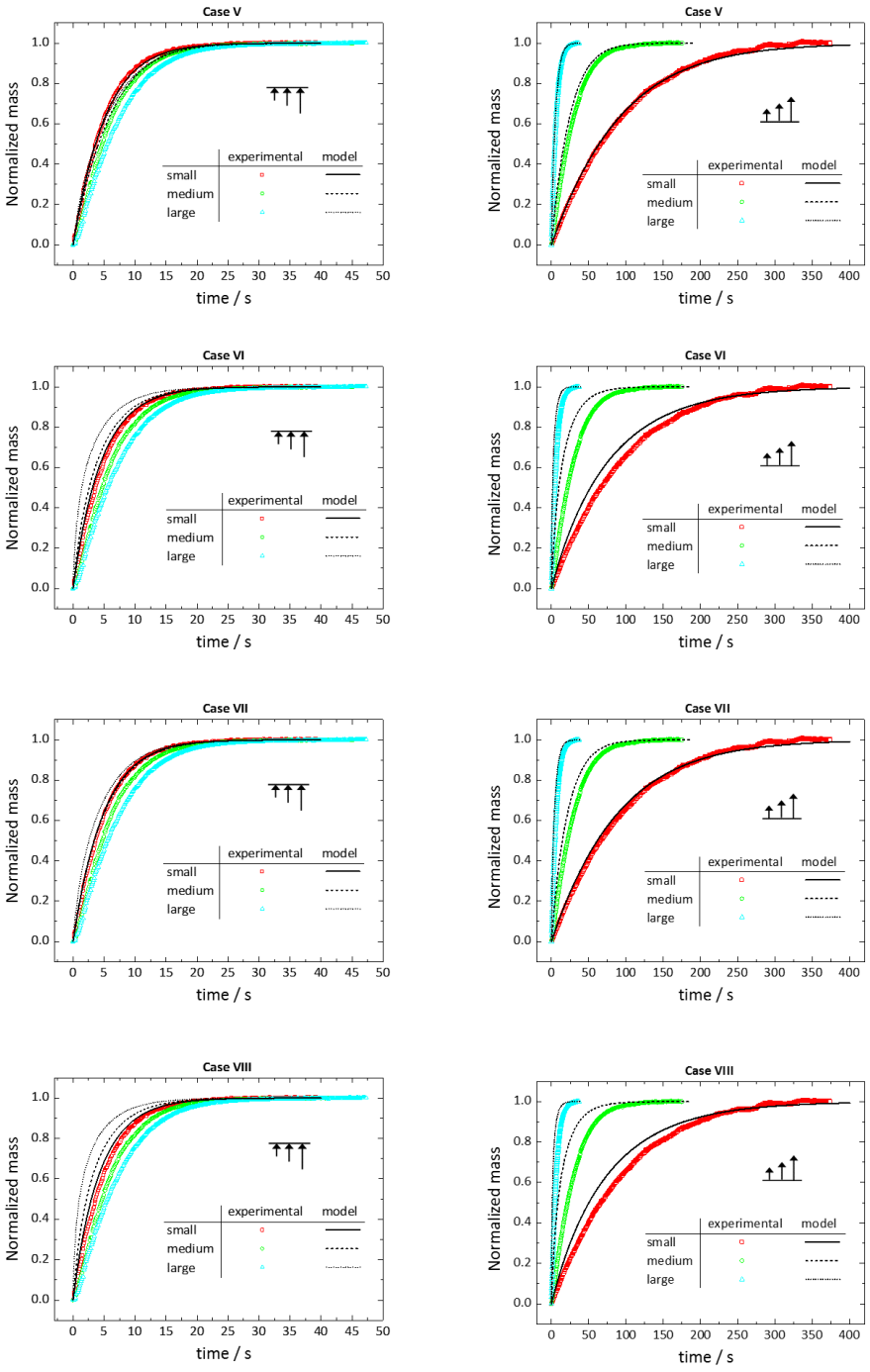

Figure 5.10: continued.

The issue with final pO_2 in experiments under small driving force

As introduced in the main part, Wang et al.[80] investigated the effect of the magnitude of pO_2 change on the relaxation behavior, and pointed out that the surface reaction rate constants are deviated in which ΔpO_2 is larger than the certain size. However, solid understanding on the maximum magnitude of ΔpO_2 to obtain true material-kinetic parameters, especially the surface reaction rate constants. In this chapter, we have derived a reaction rate equation which consists of the final ΔpO_2 and defect concentrations:

$$R_O(t) = \frac{dc_O(t)}{dt} = A \cdot pO_{2,f}{}^{\omega}[V_O^{\bullet\bullet}]^{\alpha} n^{\beta} - B \cdot [V_O^{\bullet\bullet}]^{\alpha'} n^{\beta'} [O_O^{\times}]^{\gamma} \tag{5.24}$$

Here, it is clear that the reaction rate is dependent on the RDS and the pO_2 dependencies of point defects. Let us consider the situation that in certain thermodynamic condition the change of pO_2 is much larger than the absolute change of defect concentrations, in other words, the term related with defect concentrations has the weak pO_2 dependence. Then, the overall reaction rate will be dominated by ΔpO_2, and accordingly the relaxation profile would not be strongly dependent on the magnitude of ΔpO_2. However, it apparently means that in the opposite case the smallest ΔpO_2 should be applied to obtain the true surface reaction rate constants.

The pO_2 dependencies of defects are changed in many cases as temperature and pO_2 change. Furthermore, RDS is not readily unveiled. Thus, as discussed in chapter 3, the smallest driving force is always strongly recommended. If the total conductivity or mass are not changed significantly against pO_2, thus one should apply relatively large ΔpO_2, it should be shown that the relaxation profiles under different initial and identical final pO_2 are exactly identical.

Chapter 6

CONCLUSION AND FUTURE OUTLOOK

6.1 Summary

Chemical redox kinetics of nonstoichiometric oxides, especially ceria system, was investigated with respect to thermodynamic (temperature, oxygen partial pressure, water vapor partial pressure) and non-thermodynamic (gas flow rate, morphology of material) parameters via relaxation methods in electrical conductance and mass. We found the following:

1. In thermodynamic conditions where the oxides have relatively large changes with respect to pO_2, generally in high temperature and/or low pO_2 regime, the redox kinetics driven by atmospheric pO_2 change is limited by capacity of sweep-gas to supply/remove oxygen to/from the oxides.

    a) The relaxation profiles of oxygen concentration within oxides driven by sufficiently small ΔpO_2 under both of gas-phase and surface-reaction limits follow identical functional form, a simple exponential decay function.

    b) In gas-phase limit, the relaxation time is dependent only on the material thermodynamic properties and the normalized gas flow rate, without the influence of pore architecture and material kinetic properties. In the material-kinetic (specifically surface-reaction) limit, it is exactly opposite.

    c) The transition between material-kinetic and gas-phase limits is shifted to higher temperatures as specific surface area is decreased or normalized gas flow rate is increased.

2. In humidifed atmosphere, total oxygen flux at the interface of gas/solid is a simple sum of each flux sourced from O_2 and H_2O, where the material can thermodynamically dissociate H_2O, and thus surface reaction rate constant (k_{Chem}) in the humidified conditions consists of a sum of $k_{\mathrm{Chem,O_2}}$ and $k_{\mathrm{Chem,H_2O}}$.

3. Relaxation behavior of oxygen concentration within oxides under large driving force (large ΔpO_2) in material-kinetic limit is a result of convolution of surface reaction rate constants and rate determining step (RDS) of oxidation reaction.

    a) From the comparison between relaxation profile and reaction rate expression based on non-equilibrium thermodynamics and transition state theory for possible RDSs, the most probable RDS can be known.

    b) For 10% Pr doped ceria at 700 °C, reduction of diatomic oxygen from neutral oxygen molecule to superoxo is the probable RDS in oxidation reaction.

6.2 Recommendation for Future investigations

1. **Oxidation kinetics in thermochemical two-temperature cycle**

    In actual two-temperature thermochemical cycle, kinetics during oxidation which is an incorporation of H_2O/CO_2 into the reduced oxide at around 800 °C is still not well understood due to its complexity: (i) oxygen for the oxidatin of the oxide is sourced only from H_2O/CO_2, therefore the surface reaction rate as a function of pO_2 as well as pH_2O should be known in that thermodynamic regime, (ii) the effective pO_2 is changed from very low ($\sim 10^{-25}$) to high ($\sim 10^{-8}$) values, *i.e.* very large ΔpO_2 is applied on the oxide, and (iii) the thermodynamic power for dissociating H_2O/CO_2 is decreased as the oxidation proceeds, in other words, the actual utilization amount of H_2O/CO_2 per total amount of supplied H_2O/CO_2 is continuously decreased as the oxygen nonstoichiometry of the oxide is decreased along the oxidation, and therefore, there may be a transition from material-kinetic to gas-phase limits after a certain time period.

    k_{Chem} study as a function of pO_2 and pH_2O in reduced atmosphere might be worth to try. Furthermore, the effect of large ΔpO_2 in this regime needs to be studied. From these studies if i) one figures out probable RDS and ii) can perfectly anticipate the reaction rate under surface reaction limit for given pO_2 change condition, theoretical calculation relevant to the transition from material-kinetic to gas-phase limits can be done based on the thermodynamic information of equilibrium δ vs. pO_2 and based on the reaction extent of H_2O dissociation as a function of pO_2. This calculation will show whether the transition exists or not.

2. **Impedance relaxation technique**

   Electrical conductance relaxation method enables one to measure each or both the chemical diffusion coefficient and surface reaction rate constant for oxide materials showing a measurable change in conductance against pO_2. Mass relaxation method has wider applicability even for such oxides showing pO_2 independent conductance behavior. Another powerful tool is elecrochemical impedance spectroscopy. Its merits include being able to separate several resistance components such as bulk, grain boundary, and electrode resistances, which means that the redox kinetics (or hydration/dehydration kinetics in certain case) for bulk and grain boundary can be separated by tracking the impedance change driven by ΔpO_2 (or ΔpH_2O) along time. To my best knowledge, no one has reported an comparison between the redox kinetics of bulk and that of grain boundary.

Appendix A

RUNGE-KUTTA METHOD FOR SOLVING ORDINARY DIFFERENTIAL EQUATION

Let's consider the numerical methods for ordinary differential equations (ODEs). It is used to find numerical approximations to the solutions of ODEs by evaluating the function f at points between x_i and x_{i+1}.
Let an initial value problem be specified as follows:

$$\frac{dy}{dt} = f(x, y); \qquad y(x_0) = y_0 \tag{A.1}$$

where y is an unknown function of time t, which we would like to approximate. The $\frac{dy}{dt}$, which is the rate at which y changes, is a function of t and of y itself.

The formula for the Euler method is [134]

$$y_{n+1} = y_{n+1} + h \cdot f\,(x_n, y_n) \tag{A.2}$$

which advances a solution from x_n to $x_{n+1} \equiv x_n + h$. It advances the solution through an interval h, but uses derivative information only at the beginning of that interval. That means that the step's error is only one power of h smaller than the correction, *i.e.* $O(h^2)$ added to Equation (A.2). Euler's method is not commonly recommended for practical use because the method is not very accurate compared to other methods run at the equivalent stepsize, and neither is it very stable. Instead, we can consider the use of a step like Equation (A.2) to take a "trial" step to the midpoint of the interval. And then use the value of both x and y at that midpoint to compute the "real" step across the whole interval. In the equations,

$$\begin{aligned} lk_1 &= h \cdot f\,(x_n, y_n) \\ k_2 &= h \cdot f\left(x_n + \frac{1}{2}h, y_n + \frac{1}{2}k_1\right) \\ y_{n+1} &= y_n + k_2 + O(h^3) \end{aligned} \tag{A.3}$$

As indicated in the error term, this symmetrization cancels out the first-order error term, making the method *second order*. In fact, (A.3) is called the *second-order Runge-Kutta* method.

By adding up the right combination along this approach, we can eliminate the error terms order by order. This is the basic idea of the Runge-Kutta method. By far the most often used is the classical *fouth-order Runge-Kutta formula*, as follows:

$$
\begin{aligned}
k_1 &= h \cdot f\left(x_n, y_n\right) \\
k_2 &= h \cdot f\left(x_n + \frac{1}{2}h, y_n + \frac{1}{2}k_1\right) \\
k_3 &= h \cdot f\left(x_n + \frac{1}{2}h, y_n + \frac{1}{2}k_2\right) \\
k_4 &= h \cdot f\left(x_n + h, y_n + k_3\right) \\
y_{n+1} &= y_n + \frac{1}{6}\left(k_1 + 2k_2 + 2k_3 + k_4\right) + O(h^5)
\end{aligned}
$$

The fourth-order Runge-Kutta method is often, perhaps even usually, superior to the lower order method such as Euler method; however, the *high order* does not always mean *high accuracy*. It therefore means that the convergence should always be checked for different stepsize, h.

BIBLIOGRAPHY

1. Sieminski, A. International energy outlook. *Energy Information Administration (EIA)* (2014).
2. Stocker, T. *Climate change 2013: the physical science basis: Working Group I contribution to the Fifth assessment report of the Intergovernmental Panel on Climate Change* (Cambridge University Press, 2014).
3. Kudo, A. & Miseki, Y. Heterogeneous photocatalyst materials for water splitting. *Chemical Society Reviews* **38,** 253–278 (2009).
4. Maeda, K. Photocatalytic water splitting using semiconductor particles: history and recent developments. *Journal of Photochemistry and Photobiology C: Photochemistry Reviews* **12,** 237–268 (2011).
5. Steinfeld, A. Solar hydrogen production via a two-step water-splitting thermochemical cycle based on Zn/ZnO redox reactions. *International Journal of Hydrogen Energy* **27,** 611–619 (2002).
6. Chueh, W. C. *et al.* High-Flux Solar-Driven Thermochemical Dissociation of CO_2 and H_2O Using Nonstoichiometric Ceria. *Science* **330.** 698OS Times Cited:324 Cited References Count:27, 1797–1801. ISSN: 0036-8075 (2010).
7. Yang, C.-K. *An Exploration of Perovskite Materials for Thermochemical Water Splitting* PhD thesis (California Institute of Technology, 2015).
8. Chueh, W. C. & Haile, S. M. A thermochemical study of ceria: exploiting an old material for new modes of energy conversion and CO_2 mitigation. *Philosophical Transactions of the Royal Society a-Mathematical Physical and Engineering Sciences* **368,** 3269–3294. ISSN: 1364-503X (2010).
9. Wang, L., Merkle, R. & Maier, J. Surface Kinetics and Mechanism of Oxygen Incorporation Into $Ba_{1-x}Sr_xCo_yFe_{1-y}O_{3-\delta}$ SOFC Microelectrodes. *Journal of The Electrochemical Society* **157,** B1802–B1808 (2010).
10. Jung, W. & Tuller, H. L. A New Model Describing Solid Oxide Fuel Cell Cathode Kinetics: Model Thin Film $SrTi_{1-x}Fe_xO_{3-\delta}$ Mixed Conducting Oxides–a Case Study. *Advanced Energy Materials* **1,** 1184–1191 (2011).
11. Fleig, J., Kim, H.-R., Jamnik, J & Maier, J. Oxygen Reduction Kinetics of Lanthanum Manganite (LSM) Model Cathodes: Partial Pressure Dependence and Rate-Limiting Steps. *Fuel Cells* **8,** 330–337 (2008).
12. Lane, J. & Kilner, J. Oxygen surface exchange on gadolinia doped ceria. *Solid State Ionics* **136,** 927–932 (2000).
13. Ishihara, T. *et al.* Oxygen surface exchange and diffusion in $LaGaO_3$ based perovskite type oxides. *Solid State Ionics* **113,** 593–600 (1998).

14. Scheffe, J. R., Weibel, D. & Steinfeld, A. Lanthanum–strontium–manganese perovskites as redox materials for solar thermochemical splitting of H_2O and CO_2. *Energy & Fuels* **27,** 4250–4257. ISSN: 0887-0624 (2013).

15. Cooper, T. *et al.* Lanthanum Manganite Perovskites with Ca/Sr A-site and Al B-site Doping as Effective Oxygen Exchange Materials for Solar Thermochemical Fuel Production. *Energy Technology* **3,** 1130–1142 (2015).

16. Scheffe, J. R. & Steinfeld, A. Thermodynamic analysis of cerium-based oxides for solar thermochemical fuel production. *Energy & Fuels* **26,** 1928–1936 (2012).

17. Hao, Y., Yang, C. K. & Haile, S. M. Ceria-Zirconia Solid Solutions ($Ce_{1-x}Zr_xO_{2-delta}$, $x \leqq 0.2$) for Solar Thermochemical Water Splitting: A Thermodynamic Study. *Chemistry of Materials* **26,** 6073–6082. ISSN: 0897-4756 (2014).

18. Maier, J. On the correlation of macroscopic and microscopic rate constants in solid state chemistry. *Solid State Ionics* **112,** 197–228. ISSN: 0167-2738 (1998).

19. Maier, J. Interaction of oxygen with oxides:: How to interpret measured effective rate constants? *Solid State Ionics* **135,** 575–588 (2000).

20. Kim, J. J., Bishop, S. R., Thompson, N. J., Chen, D. & Tuller, H. L. Investigation of nonstoichiometry in oxide thin films by simultaneous in situ optical absorption and chemical capacitance measurements: Pr-doped ceria, a case study. *Chemistry of Materials* **26,** 1374–1379 (2014).

21. Gopal, C. B. & Haile, S. M. An electrical conductivity relaxation study of oxygen transport in samarium doped ceria. *Journal of Materials Chemistry A* **2,** 2405–2417. ISSN: 2050-7488 (2014).

22. Song, C. R. & Yoo, H. I. Chemical diffusivity of $BaTiO_{3-delta}$ I. Experimental determination. *Solid State Ionics* **120,** 141–153. ISSN: 0167-2738 (1999).

23. Yasuda, I. & Hikita, T. Precise Determination of the Chemical Diffusion Coefficient of Calcium-Doped Lanthanum Chromites by Means of Electrical Conductivity Relaxation. *Journal of The Electrochemical Society* **141,** 1268–1273. ISSN: 0013-4651 (1994).

24. Katsuki, M., Wang, S., Yasumoto, K. & Dokiya, M. The oxygen transport in Gd-doped ceria. *Solid State Ionics* **154,** 589–595 (2002).

25. Yashiro, K *et al.* Mass transport properties of $Ce_{0.9}Gd_{0.1}O_{2-\delta}$ at the surface and in the bulk. *Solid State Ionics* **152,** 469–476 (2002).

26. Ackermann, S., Scheffe, J. R. & Steinfeldt, A. Diffusion of Oxygen in Ceria at Elevated Temperatures and Its Application to H_2O/CO_2 Splitting Thermochemical Redox Cycles. *Journal of Physical Chemistry C* **118,** 5216–5225. ISSN: 1932-7447 (2014).

27. Bouwmeester, H., Den Otter, M. & Boukamp, B. Oxygen transport in $La_{0.65}Sr_{0.4}Co_{1-y}Fe_yO_{3-\delta}$. *Journal of Solid State Electrochemistry* **8,** 599–605. ISSN: 1432-8488 (2004).

28. Yang, C. K., Yamazaki, Y., Aydin, A. & Haile, S. M. Thermodynamic and kinetic assessments of strontium-doped lanthanum manganite perovskites for two-step thermochemical water splitting. *Journal of Materials Chemistry A* **2,** 13612–13623. ISSN: 2050-7488 (2014).

29. Hao, Y., Yang, C. K. & Haile, S. M. High-temperature isothermal chemical cycling for solar-driven fuel production. *Physical Chemistry Chemical Physics* **15,** 17084–17092. ISSN: 1463-9076 (2013).

30. Davenport, T. C., Yang, C.-K., Kucharczyk, C. J., Ignatowich, M. J. & Haile, S. M. Implications of Exceptional Material Kinetics on Thermochemical Fuel Production Rates. *Energy Technology,* n/a–n/a. ISSN: 2194-4296 (2016).

31. Roine, A. HSC Chemistry 5.11. *Outokumpu Research Oy, Pori, Finland* **76** (2002).

32. Panlener, R., Blumenthal, R. & Garnier, J. A thermodynamic study of non-stoichiometric cerium dioxide. *Journal of Physics and Chemistry of Solids* **36,** 1213–1222. ISSN: 0022-3697 (1975).

33. Haile, S. M. Fuel cell materials and components. *Acta Materialia* **51,** 5981–6000 (2003).

34. Bonanos, N, Knight, K. & Ellis, B. Perovskite solid electrolytes: structure, transport properties and fuel cell applications. *Solid State Ionics* **79,** 161–170 (1995).

35. Shao, Z. & Haile, S. M. A high-performance cathode for the next generation of solid-oxide fuel cells. *Nature* **431,** 170–173 (2004).

36. Tao, S. & Irvine, J. T. A redox-stable efficient anode for solid-oxide fuel cells. *Nature materials* **2,** 320–323 (2003).

37. Shao, Z. *et al.* Investigation of the permeation behavior and stability of a $Ba_{0.5}Sr_{0.5}Co_{0.8}Fe_{0.2}O_{3-\delta}$ oxygen membrane. *Journal of Membrane Science* **172,** 177–188 (2000).

38. Mastrikov, Y. A., Kuklja, M. M., Kotomin, E. A. & Maier, J. First-principles modelling of complex perovskite $(Ba_{1-x}Sr_x)(Co_{1-y}Fe_y)O_{3-\delta}$ for solid oxide fuel cell and gas separation membrane applications. *Energy & Environmental Science* **3,** 1544–1550 (2010).

39. Suntivich, J. *et al.* Design principles for oxygen-reduction activity on perovskite oxide catalysts for fuel cells and metal–air batteries. *Nature Chemistry* **3,** 546–550 (2011).

40. Suntivich, J., May, K. J., Gasteiger, H. A., Goodenough, J. B. & Shao-Horn, Y. A perovskite oxide optimized for oxygen evolution catalysis from molecular orbital principles. *Science* **334,** 1383–1385 (2011).

41. Pena, M. & Fierro, J. Chemical structures and performance of perovskite oxides. *Chemical reviews* **101,** 1981–2018 (2001).

42. Kašpar, J, Fornasiero, P & Graziani, M. Use of CeO_2-based oxides in the three-way catalysis. *Catalysis Today* **50,** 285–298 (1999).

43. McDaniel, A. H. *et al.* Sr-and Mn-doped $LaAlO_{3-\delta}$ for solar thermochemical H_2 and CO production. *Energy & Environmental Science* **6,** 2424–2428 (2013).

44. Rudisill, S. G. *et al.* Enhanced oxidation kinetics in thermochemical cycling of CeO_2 through templated porosity. *The Journal of Physical Chemistry C* **117,** 1692–1700. ISSN: 1932-7447 (2013).

45. Sholklapper, T. Z., Kurokawa, H., Jacobson, C. P., Visco, S. J. & De Jonghe, L. C. Nanostructured Solid Oxide Fuel Cell Electrodes. *Nano Letters* **7,** 2136–2141. ISSN: 1530-6984 (2007).

46. Jung, W., O. Dereux, J., C. Chueh, W., Hao, Y. & M. Haile, S. High electrode activity of nanostructured, columnar ceria films for solid oxide fuel cells. *Energy & Environmental Science* **5,** 8682–8689 (2012).

47. Furler, P. *et al.* Solar thermochemical CO_2 splitting utilizing a reticulated porous ceria redox system. *Energy & Fuels* **26,** 7051–7059. ISSN: 0887-0624 (2012).

48. Furler, P. *et al.* Thermochemical CO_2 splitting via redox cycling of ceria reticulated foam structures with dual-scale porosities. *Physical Chemistry Chemical Physics* **16,** 10503–10511 (2014).

49. Keene, D. J., Lipiński, W. & Davidson, J. H. The effects of morphology on the thermal reduction of nonstoichiometric ceria. *Chemical Engineering Science* **111,** 231–243. ISSN: 0009-2509 (2014).

50. Ackermann, S., Takacs, M., Scheffe, J. & Steinfeld, A. Reticulated porous ceria undergoing thermochemical reduction with high-flux irradiation. *International Journal of Heat and Mass Transfer* **107,** 439–449. ISSN: 0017-9310 (2017).

51. Gellings, P. J. & Bouwmeester, H. J. *Handbook of Solid State Electrochemistry* Google-Books-ID: SI070Alf90oC. 646 pp. (CRC Press, 1997).

52. Maier, J. *Physical chemistry of ionic materials: ions and electrons in solids* ISBN: 0470020210 (John Wiley & Sons, 2004).

53. Ji, H.-I., C. Davenport, T., Balaji Gopal, C. & M. Haile, S. Extreme high temperature redox kinetics in ceria: exploration of the transition from gas-phase to material-kinetic limitations. *Physical Chemistry Chemical Physics* **18,** 21554–21561 (2016).

54. Marxer, D. *et al.* Demonstration of the Entire Production Chain to Renewable Kerosene via Solar Thermochemical Splitting of H_2O and CO_2. *Energy & Fuels* **29,** 3241–3250 (2015).

55. Davenport, T. C., Yang, C.-K., Kucharczyk, C. J., Ignatowich, M. J. & Haile, S. M. Maximizing fuel production rates in isothermal solar thermochemical fuel production. *Applied Energy* **183,** 1098–1111 (2016).

56. Kim, S *et al.* Oxygen Surface Exchange in Mixed Ionic Electronic Conductors: Application to $La_{0.5}Sr_{0.5}Fe_{0.8}Ga_{0.2}O_{3-\delta}$. *Journal of the Electrochemical Society* **147,** 2398–2406 (2000).

57. Crank, J. *The mathematics of diffusion* ISBN: 0198534116 (Oxford university press, 1979).

58. Tuller, H. & Nowick, A. Defect structure and electrical properties of non-stoichiometric CeO_2 single crystals. *Journal of The Electrochemical Society* **126,** 209–217. ISSN: 0013-4651 (1979).

59. Elshof, J. E. t., Lankhorst, M. H. R. & Bouwmeester, H. J. M. Oxygen Exchange and Diffusion Coefficients of Strontium-Doped Lanthanum Ferrites by Electrical Conductivity Relaxation. *Journal of The Electrochemical Society* **144,** 1060–1067. ISSN: 0013-4651, 1945-7111 (1997).

60. Preis, W., Bucher, E. & Sitte, W. Oxygen exchange kinetics of $La_{0.4}Sr_{0.6}FeO_{3-\delta}$ by simultaneous application of conductivity relaxation and carrier gas coulometry. *Solid State Ionics* **175,** 393–397. ISSN: 0167-2738 (2004).

61. Studart, A. R., Gonzenbach, U. T., Tervoort, E. & Gauckler, L. J. Processing Routes to Macroporous Ceramics: A Review. *Journal of the American Ceramic Society* **89,** 1771–1789. ISSN: 1551-2916 (2006).

62. Colombo, P. Conventional and novel processing methods for cellular ceramics. *Philosophical Transactions of the Royal Society a-Mathematical Physical and Engineering Sciences* **364,** 109–124 (2006).

63. Ackermann, S., Scheffe, J. R., Duss, J. & Steinfeld, A. Morphological Characterization and Effective Thermal Conductivity of Dual-Scale Reticulated Porous Structures. *Materials* **7,** 7173–7195 (2014).

64. Kamiya, M., Shimada, E., Ikuma, Y., Komatsu, M. & Haneda, H. Intrinsic and extrinsic oxygen diffusion and surface exchange reaction in cerium oxide. *Journal of the Electrochemical Society* **147,** 1222–1227. ISSN: 0013-4651 (2000).

65. Gerhardt, R. & Nowick, A. S. Grain-Boundary Effect in Ceria Doped with Trivalent Cations: I, Electrical Measurements. *Journal of the American Ceramic Society* **69,** 641–646. ISSN: 1551-2916 (1986).

66. Gerhardt, R., Nowick, A. S., Mochel, M. E. & Dumler, I. Grain-Boundary Effect in Ceria Doped with Trivalent Cations: II, Microstructure and Microanalysis. *Journal of the American Ceramic Society* **69,** 647–651. ISSN: 1551-2916 (1986).

67. Tanaka, J., Baumard, J.-F. & Abelard, P. Nonlinear Electrical Properties of Grain Boundaries in an Oxygen-Ion Conductor ($CeO_2{\cdot}Y_2O_3$). *Journal of the American Ceramic Society* **70,** 637–643. ISSN: 1551-2916 (1987).

68. E. Usiskin, R., Maruyama, S., J. Kucharczyk, C., Takeuchi, I. & M. Haile, S. Probing the reaction pathway in $(La_{0.8}Sr_{0.2})_{0.95}MnO_{3+\delta}$ using libraries of thin film microelectrodes. *Journal of Materials Chemistry A* **3,** 19330–19345 (2015).

69. Lee, W. *et al.* Oxygen Surface Exchange at Grain Boundaries of Oxide Ion Conductors. *Advanced Functional Materials* **22,** 965–971 (2012).

70. Navickas, E. *et al.* Fast oxygen exchange and diffusion kinetics of grain boundaries in Sr-doped $LaMnO_3$ thin films. *Physical Chemistry Chemical Physics* **17,** 7659–7669 (2015).

71. Knoblauch, N., Dörrer, L., Fielitz, P., Schmücker, M. & Borchardt, G. Surface controlled reduction kinetics of nominally undoped polycrystalline CeO_2. *Physical Chemistry Chemical Physics* **17,** 5849–5860 (2015).

72. Welty, J. R., Wicks, C. E., Rorrer, G. & Wilson, R. E. *Fundamentals of momentum, heat, and mass transfer* ISBN: 8126515260 (John Wiley & Sons, 2009).

73. Gopal, C. B. & van de Walle, A. Ab initio thermodynamics of intrinsic oxygen vacancies in ceria. *Physical Review B* **86,** 134117 (2012).

74. Zinkevich, M., Djurovic, D. & Aldinger, F. Thermodynamic modelling of the cerium–oxygen system. *Solid State Ionics* **177,** 989–1001. ISSN: 0167-2738 (2006).

75. Falkenstein, A., Mueller, D. N., De Souza, R. A. & Martin, M. Chemical relaxation experiments on mixed conducting oxides with large stoichiometry deviations. *Solid State Ionics* **280,** 66–73. ISSN: 0167-2738 (2015).

76. Lohne, F., Søgaard, M. & Wiik, K. The Significance of Gas-Phase Mass Transport in Assessment of $_{k\mathrm{Chem}}$ and D_{Chem}. *Journal of The Electrochemical Society* **160,** F1282–F1292. ISSN: 0013-4651 (2013).

77. Den Otter, M., Van der Haar, L. & Bouwmeester, H. Numerical evaluation of eigenvalues of the sheet diffusion problem in the surface/diffusion mixed regime. *Solid State Ionics* **134,** 259–264. ISSN: 0167-2738 (2000).

78. Den Otter, M., Bouwmeester, H., Boukamp, B. & Verweij, H. Reactor flush time correction in relaxation experiments. *Journal of the Electrochemical Society* **148,** J1–J6. ISSN: 0013-4651 (2001).

79. Boukamp, B. A., den Otter, M. W. & Bouwmeester, H. J. Transport processes in mixed conducting oxides: combining time domain experiments and frequency domain analysis. *Journal of Solid State Electrochemistry* **8,** 592–598. ISSN: 1432-8488 (2004).

80. Wang, S, Verma, A, Yang, Y., Jacobson, A. & Abeles, B. The effect of the magnitude of the oxygen partial pressure change in electrical conductivity relaxation measurements: oxygen transport kinetics in $La_{0.5}Sr_{0.5}CoO_{3-\delta}$. *Solid State Ionics* **140,** 125–133. ISSN: 0167-2738 (2001).

81. Blumenthal, R., Lee, P. & Panlener, R. Studies of the defect structure of nonstoichiometric cerium dioxide. *Journal of The Electrochemical Society* **118,** 123–129. ISSN: 0013-4651 (1971).

82. Merkle, R. & Maier, J. Oxygen incorporation into Fe-doped $SrTiO_3$: Mechanistic interpretation of the surface reaction. *Physical Chemistry Chemical Physics* **4,** 4140–4148 (2002).

83. Chueh, W. C. & Haile, S. M. Electrochemistry of mixed oxygen ion and electron conducting electrodes in solid electrolyte cells. *Annual review of chemical and biomolecular engineering* **3,** 313–341. ISSN: 1947-5438 (2012).

84. Kröger, F., Vink, H., Seitz, F. & Turnbull, D. Solid state physics. *Academic, New York,* 307–435 (1956).

85. Adler, S. B., Chen, X. Y. & Wilson, J. R. Mechanisms and rate laws for oxygen exchange on mixed-conducting oxide surfaces. *Journal of Catalysis* **245,** 91–109. ISSN: 0021-9517 (2007).

86. Fleig, J., Merkle, R. & Maier, J. The $p(O_2)$ dependence of oxygen surface coverage and exchange current density of mixed conducting oxide electrodes: model considerations. *Physical Chemistry Chemical Physics* **9,** 2713–2723 (2007).

87. Wang, S, van der Heide, P., Chavez, C, Jacobson, A. & Adler, S. An electrical conductivity relaxation study of $La_{0.6}Sr_{0.4}Fe_{0.8}Co_{0.2}O_{3-\delta}$. *Solid State Ionics* **156,** 201–208. ISSN: 0167-2738 (2003).

88. Stan, M, Zhu, Y., Jiang, H & Butt, D. Kinetics of oxygen removal from ceria. *Journal of applied physics* **95,** 3358–3361 (2004).

89. Cerda, R. M. *Understanding quartz crystals and oscillators* (Artech House, 2014).

90. Elam, J. & Pellin, M. GaPO4 sensors for gravimetric monitoring during atomic layer deposition at high temperatures. *Analytical chemistry* **77,** 3531–3535 (2005).

91. Krispel, F *et al. Properties and applications of singly rotated GaPO/sub 4/resonators* in *Frequency Control Symposium and PDA Exhibition Jointly with the 17th European Frequency and Time Forum, 2003. Proceedings of the 2003 IEEE International* (2003), 668–673.

92. Fritze, H. High-temperature bulk acoustic wave sensors. *Measurement Science and Technology* **22,** 012002 (2010).

93. Bishop, S. R., Stefanik, T. S. & Tuller, H. L. Electrical conductivity and defect equilibria of $Pr_{0.1}Ce_{0.9}O_{2-\delta}$. *Physical Chemistry Chemical Physics* **13,** 10165–10173 (2011).

94. Benes, E, Schmid, M & Thorn, G. Progress in monitoring thin film thickness by use of quartz crystals. *Thin Solid Films* **174,** 307–314 (1989).

95. Lu, C.-S. & Lewis, O. Investigation of film-thickness determination by oscillating quartz resonators with large mass load. *Journal of Applied Physics* **43,** 4385–4390 (1972).

96. Wimmer, L, Hertl, S, Hemetsberger, J & Benes, E. New method of measuring vibration amplitudes of quartz crystals. *Review of scientific instruments* **55,** 605–609 (1984).

97. Miller, J. & Bolef, D. Acoustic Wave Analysis of the Operation of Quartz-Crystal Film-Thickness Monitors. *Journal of Applied Physics* **39,** 5815–5816 (1968).

98. Benes, E. Improved quartz crystal microbalance technique. *Journal of Applied Physics* **56,** 608–626 (1984).

99. Buzea, C. & Robbie, K. State of the art in thin film thickness and deposition rate monitoring sensors. *Reports on Progress in Physics* **68,** 385 (2005).

100. Lu, C.-s. Mass determination with piezoelectric quartz crystal resonators. *Journal of vacuum science and technology* **12,** 578–583 (1975).

101. *QCM100: Quartz Crystal Microbalance Theory and Calibration* tech. rep. (Sunnyvale, CA: Stanford Research Systems, Inc). `www.thinksrs.com/downloads/PDFs/ApplicationNotes/QCMTheoryapp.pdf`.

102. Sauerbrey, G. Verwendung von Schwingquarzen zur Wägung dünner Schichten und zur Mikrowägung. *Zeitschrift für physik* **155,** 206–222 (1959).

103. Reiter, C., Krempl, P. W., Thanner, H., Wallnöfer, W. & Worsch, P. M. *Material properties of $GaPO_4$ and their relevance for applications* in *Annales de chimie science des matériaux* **26** (2001), 91–94.

104. Nosek, J. & Pustka, M. *About the coupling factor of the gallium orthophosphate ($GaPO_4$) and its influence to the resonance-frequency temperature dependence* in *Frequency Control Symposium and PDA Exhibition Jointly with the 17th European Frequency and Time Forum, 2003. Proceedings of the 2003 IEEE International* (2003), 674–678.

105. Millichamp, J. *et al.* Application of a $GaPO_4$ crystal microbalance for the detection of coke formation in high-temperature reactors and solid oxide fuel cells. *Industrial & Engineering Chemistry Research* **50,** 8371–8375 (2011).

106. Millichamp, J. *et al.* A study of carbon deposition on solid oxide fuel cell anodes using electrochemical impedance spectroscopy in combination with a high temperature crystal microbalance. *Journal of Power Sources* **235,** 14–19 (2013).

107. Meng, Q.-L., Lee, C.-i., Kaneko, H. & Tamaura, Y. Solar thermochemical process for hydrogen production via two-step water splitting cycle based on $Ce_{1-x}Pr_xO_{2-\delta}$ redox reaction. *Thermochimica Acta* **532,** 134–138 (2012).

108. Stefanik, T. S. & Tuller, H. L. Praseodymium-cerium oxide as a surface-effect gas sensor. *Journal of electroceramics* **13,** 771–774 (2004).

109. Shuk, P & Greenblatt, M. Hydrothermal synthesis and properties of mixed conductors based on $Ce_{1-x}Pr_xO_{2-\delta}$ solid solutions. *Solid State Ionics* **116,** 217–223 (1999).

110. Takasu, Y, Sugino, T & Matsuda, Y. Electrical conductivity of praseodymia doped ceria. *Journal of applied electrochemistry* **14,** 79–81 (1984).

111. Chen, D., Bishop, S. R. & Tuller, H. L. Praseodymium-cerium oxide thin film cathodes: Study of oxygen reduction reaction kinetics. *Journal of electroceramics* **28,** 62–69. ISSN: 1385-3449 (2012).

112. *High Temperature Microbalance Sensor Crystals - Type R-30* tech. rep. (Graz, Austria: Piezocryst Advanced Sensorics GmbH, 2008). `http://www.piezocryst.com/fileadmin/user_upload/pdf/R-30_Datenblatt_Rev.01.pdf`.

113. Infortuna, A., Harvey, A. S. & Gauckler, L. J. Microstructures of CGO and YSZ thin films by pulsed laser deposition. *Advanced Functional Materials* **18,** 127–135 (2008).

114. Richter, J., Holtappels, P., Graule, T., Nakamura, T. & Gauckler, L. J. Materials design for perovskite SOFC cathodes. *Monatshefte für Chemie-Chemical Monthly* **140,** 985–999 (2009).

115. Davenport, T., Ignatowich, M., Wilke, S., Hao, Y & Haile, S. *Thermodynamics of $Ce_{0.9}Pr_{0.1}O_2$ for Thermochemical Water Splitting* In preparation.

116. Che, M & Tench, A. Characterization and reactivity of molecular oxygen species on oxide surfaces. *Advances in catalysis* **32,** 1–148 (1983).

117. Anpo, M. *et al.* Generation of superoxide ions at oxide surfaces. *Topics in catalysis* **8,** 189–198 (1999).

118. Kawabe, T., Tabata, K., Suzuki, E., Yamaguchi, Y. & Nagasawa, Y. Electronic states of chemisorbed oxygen species and their mutually related studies on SnO_2 thin film. *The Journal of Physical Chemistry B* **105,** 4239–4244 (2001).

119. Bermudez, V. M. & Ritz, V. H. Adsorption of O2 on the SrTiO3 (100)-(1× 1) surface. *Chemical Physics Letters* **73,** 160–166 (1980).

120. Che, M & Tench, A. Characterization and reactivity of mononuclear oxygen species on oxide surfaces. *Advances in catalysis* **31,** 77–133 (1982).

121. Nakano, Y., Watanabe, M. & Takahashi, T. Investigation of interface states in (Sr, Ca) TiO_{3-x}-based ceramics. *Journal of applied physics* **70,** 1539–1547 (1991).

122. Rantala, T. S., Lantto, V. & Rantala, T. T. Rate equation simulation of the height of Schottky barriers at the surface of oxidic semiconductors. *Sensors and Actuators B: Chemical* **13,** 234–237 (1993).

123. Morrison, S. R. Measurement of surface state energy levels of one-equivalent absorbates on ZnO. *Surface science* **27,** 586–604 (1971).

124. Ganduglia-Pirovano, M. V., Hofmann, A. & Sauer, J. Oxygen vacancies in transition metal and rare earth oxides: Current state of understanding and remaining challenges. *Surface Science Reports* **62,** 219–270. ISSN: 0167-5729 (2007).

125. Nolan, M., Fearon, J. E. & Watson, G. W. Oxygen vacancy formation and migration in ceria. *Solid State Ionics* **177,** 3069–3074 (2006).

126. Mosleh, M., Søgaard, M. & Hendriksen, P. V. Kinetics and mechanisms of oxygen surface exchange on $La_{0.6}Sr_{0.4}FeO_{3-\delta}$ thin films. *Journal of The Electrochemical Society* **156,** B441–B457 (2009).

127. Chiang, Y.-M., Birnie III, D & Kingery, W. D. *Physical Ceramic* (Wiley, New York, 1997).

128. Kim, S. & Maier, J. On the conductivity mechanism of nanocrystalline ceria. *Journal of the Electrochemical society* **149,** J73–J83 (2002).

129. Kim, S. & Maier, J. Partial electronic and ionic conduction in nanocrystalline ceria: role of space charge. *Journal of the European Ceramic Society* **24,** 1919–1923 (2004).

130. Avila-Paredes, H. J., Choi, K., Chen, C.-T. & Kim, S. Dopant-concentration dependence of grain-boundary conductivity in ceria: A space-charge analysis. *Journal of Materials Chemistry* **19,** 4837–4842 (2009).

131. Wang, S., Inaba, H., Tagawa, H. & Hashimoto, T. Nonstoichiometry of $Ce_{0.8}Gd_{0.2}O_{1.9-x}$. *Journal of the Electrochemical Society* **144,** 4076–4080 (1997).

132. Kobayashi, T., Wang, S., Dokiya, M., Tagawa, H. & Hashimoto, T. Oxygen nonstoichiometry of $Ce_{1-y}Sm_yO_{2-0.5y-x}$ (y= 0.1, 0.2). *Solid State Ionics* **126,** 349–357 (1999).

133. Otake, T *et al.* Nonstoichiometry of $Ce_{1-x}Y_xO_{2-0.5x-\delta}$ (x= 0.1, 0.2). *Solid State Ionics* **161,** 181–186 (2003).

134. Seiler, M. C. & Seiler, F. A. Numerical recipes in C: the art of scientific computing. *Risk Analysis* **9,** 415–416 (1989).